## Title

Beyond Moore neuromorphic chips: harnessing complexity in atomic switch networks for alternative computing



## Author

Scharnhorst, Kelsey

## Publication Date

2018

Peer reviewed|Thesis/dissertation

UNIVERSITY OF CALIFORNIA

Los Angeles

# Beyond Moore neuromorphic chips: harnessing complexity in atomic switch networks for alternative computing

A dissertation submitted in partial satisfaction of the requirements for the degree Doctor of Philosophy in Chemistry

by

Kelsey Sue Scharnhorst

2018

ABSTRACT OF THE DISSERTATION

Beyond Moore neuromorphic chips:
harnessing complexity in atomic switch
networks for alternative computing

by

Kelsey Sue Scharnhorst
Doctor of Philosophy in Chemistry
University of California, Los Angeles, 2018
Professor James K. Gimzewski, Chair

The invention of the internet began the age of information as well as exponentially increased the number of complex systems in our world. As the age of information comes to an end, so does the persevering trend known as Moore's Law. This means that the number of circuit elements on an integrated chip will no longer double every two years, nor will the processing speed of computers. Personal computers utilize the Von Neumann architecture which separates storage from processing. This separation causes information transfer lags as a computer processes information much faster than it can be fetched from information storage. Thus, to circumvent both the limitations on elemental packing, and areal density a movement into neuromorphic hardware has occurred. Neuromorphic chips seek to emulate brain-like processing of

information through low-power, highly parallel, densely interconnected, and closely packed individual elements which have a non-intuitive entangled relationship. This work explored the potential of atomic switch networks (ASNs) for reservoir, natural, and unconventional computing, provides evidence for ASNs as complex adaptive systems operating in and around the edge of chaos, presents a new material for use in ASNs, and evaluates spoken digit recognition using reservoir computing. A second project herein explores the maturation of human pluripotent stem cell-derived cardiomyocytes for use in studying heart disease, which is the leading cause of death in the world. Maturation of these cells is significant to the field. Via a chemically defined differentiation regimen with a monolayer cell culture technique on top of a multi-electrode array for real-time measurements of electrophysiological properties, in vivo development was reproduced. Both systems described above required data science analysis of time-series multi-electrode array information.

The dissertation of Kelsey Sue Scharnhorst is approved.

Peter M. Felker

Dolores Bozovic

James K. Gimzewski, Committee Chair

University of California, Los Angeles

2018

To all the brave souls pursuing a Ph.D.

# Contents

Abstract . . . . . ii

List of Figures . . . . . xvii

Acknowledgements . . . . . xviii

Vita . . . . . xxii

**1 Introduction** **1**

**2 Atomic Switch Networks for Alternative and Unconventional Types of Computing** **5**

2.0.1 Materials and methods . . . . . 6

2.0.2 Results and discussion . . . . . 9

2.0.3 Conclusion . . . . . 13

**3 Logic** **15**

3.1 Introduction . . . . . 16

3.2 Fabrication . . . . . 19

3.3 Methods . . . . . 23

3.4 Results and Discussion . . . . . 27

3.5 Conclusion . . . . . 29

**4 Complex Adaptive Systems** **33**

4.1 Introduction . . . 33

4.2 Experimental Methods . . . 35

4.2.1 Fabrication and Interfacing . . . 35

4.2.2 Non-linearity . . . 37

4.2.3 Current Control . . . 40

4.3 Results and Discussion . . . 41

4.3.1 Non-linearity . . . 41

4.3.2 Control Dynamics . . . 45

4.4 Conclusions . . . 47

**5 Spoken Digit Classification Using AgI Atomic Switch Networks** **48**

5.1 Introduction . . . 49

5.2 Methods . . . 51

5.2.1 Reservoir Computing . . . 54

5.3 Results and Discussion . . . 59

5.3.1 ASN Characterization . . . 59

5.3.2 Logic Operations, Non-Temporal . . . 59

5.3.3 Logic Operations, Temporal . . . 63

5.3.4 Spoken Digit Recognition . . . 65

5.4 Conclusion . . . 67

**6 Two dimensional electrophysiological characterization of human pluripotent stem cell-derived cardiomyocyte system** **69**

6.1 Introduction . . . 70

6.2 Results . . . 72

6.3 Discussion . . . . . 81
6.4 Methods . . . . . 84

**7 Conclusions** **87**

# List of Figures

1.1 The ASN went through different generations. Electrode numbers increased from two, four, sixteen up to 128. Work presented in this document began by optimizing the fabrication process for the 128 electrode devices. . . . . 3

2.1 Device holder. Above is a computer aided design schematic of the custom 3D printed sample holder to interface with the ASN device. The main components are (a) the device holder, (b) electrical interface with gold spring-loaded pins that make contact with the platinum electrode pads of the ASN when (c) the interlocking component is twisted into the posts of (a) the device holder. The gold pins in (b) are wired into measurement hardware. . . . . 8

2.2 Distributed switching activity. Each row (a)–(c) represents activity of a patterned seed network (2 mm by 2 mm) for 3 ms (0.5 ms frame rate) at each electrode with a 5 V DC bias input at the upper right corner and a ground at the lower left corner. (a) Localized switching activity (b) switching activity localized to upper left corner (c) distributed switching activity that affects the entire network. . . 11

3.1 Optical images of the wafer with Pt electrodes and SU-8 layers present (scale bars = 1.5 mm and 500 $\mu$m, respectively). Pt electrode pattern (top) is covered in SU-8 except at inner point contacts of the platinum (bottom). . . . . 20

3.2 SEM images of the ASN device (scale bars = 20$\mu$m, 4 $\mu$m and 4 $\mu$m, respectively). Seed sites can be seen in (a), zooming in illustrates silver nanowires cladded in $Ag_2S$ crossing in the lower left of (b) and a dendritic structure originating towards the top right of (c). . . . . 22

3.3 Voltage readings from $\pm 1$ V input electrodes (top) and output electrodes (bottom). Data were sampled at 50 kHz with input bit frequencies of 5 kHz. An ideal network would have a large range of values in the output electrodes. . . . . 24

3.4 Accuracy on all logic functions learned using 1000 training samples. fig. 3.4a and fig. 3.4b used 3 V inputs; fig. 3.4c, (continued on the following page) . . . . . 30

3.5 Accuracy of learning AND with 0.01 V inputs across different numbers of both training and testing samples. . . . . 31

3.6 Accuracy of learning AND with 3 V inputs across different numbers of both training and testing samples. . . . . 31

3.7 Accuracy of learning the non-temporal XOR function with 3 V inputs across different numbers of both training and testing samples. Beating the naive guess for XOR relied on non-temporal non-linearities in the ASN. Those non-linearities were stable, making regressed coefficients valid for a large number of testing samples. . . . . 32

4.1 An optical image of an $SiO_2$ coated wafer with 120 Pt electrodes (top left, scale bar = 1 mm), a zoom in via SEM after SU-8 deposition to provide point contact electrodes which are covered by 5x5 $\mu$m Cu posts (top right, scale bar = 300 $\mu$m). Finally, an SEM of a self-assembled $Ag^+$ network after submersion in $AgNO_3$ (bottom, scale bar = 10 $\mu$m). See [18], Fig. 1 for design schematics. . . . . 36

4.2 (Color online) CAD rendering of the 3D printed interface set up for the latest generation of ASN devices which include 120 electrodes with inner networks over four times as large as previous 16 electrode devices. 120 pins in the middle section make contact with outer device electrodes and connect to measurement I/O hardware when the upper portion is depressed and locked into place within the four posts. . . . . 38

4.3 Representative example of the current-controlled feedback loop operating in real-time through control of the applied bias voltage (top) with the resulting current trace (bottom). In this example, the current set point modulated between 100$\mu$A and 500$\mu$A at 30s intervals and was monitored at a sampling frequency of 10kHz. . . . . 40

4.4 (a-c) shows IV curves of the ASN network when stimulated with a triangle wave input bias of ± 2.0 V at 10 Hz, exhibiting soft switching in (a), persisting until a conduction transition begins in (b), leading to hard switching in (c). Specific classes of V in V out Lissajous curves are featured in panels (d-f), and were stimulated by a ± 1.0 V sinusoidal 11 Hz input signal. Amplitude of the output signal corresponds to the value in the bottom right corner. Observed activity includes (d) initial pseudo linearity (containing short periods of non-linear responses), (e) asymmetric switching activity, and (f) bipolar switching activity. Channels intermittently converge and proportionally follow the input signal, resulting in the embedded elliptical shapes seen in (e) and (f). . . . . 42

4.5 Each subplot is a Lissajous figure displaying one minute of the ASN's response to an 11 Hz, 1 V sine wave at 64 spatially distributed measurement points (Normalized output V vs. 1V input). The signal was input at the electrode marked with the red box, and the device was grounded at the electrode marked with the black box in the upper left of panel (a). Additional outlined subplots represent examples shown in Figs. 4(d-f). Color bar represents the amplitude of normalized output voltages through time. . . . . 44

4.6 Plots (a) and (b) above show dependence of power law scaling (PSD $\alpha$ value) from current set point data presented in Fig. 3. The PSD slope ($\alpha$) of the current output is shown in (a) at currents of 100 $\mu$A and 500 $\mu$A and simultaneously acquired voltage (b). In all cases 1/f $\alpha$ scaling is present. Repeated cycling of PID loop and current set point demonstrated an ability to tune the PSD slope ($\alpha$), and hence spatiotemporal dynamics of the current output (c) and local voltage throughout the ASN device (d). . . . . 46

5.1 SEM image of an AgI ASN (left), transparency was set to 70% and overlaid on an optical image of point contact Pt electrodes shown in blue (left). The overlay allows one to visualize the inner measurement contacts which are 50 $\mu$m in diameter in the context of the entire network (1 $mm^2$). On the right is a zoomed in SEM image of the same network to illustrate the variety of wire lengths and diameters present. Scale bars = 250 $\mu$m and 10 $\mu$m, respectively. . . . . 50

5.2 Layers of an atomic switch network (ASN) after top-down photolithographic fabrication methods are complete, prior to bottom-up assembly of a silver network. This schematic is not to scale, but can be used as a comprehensive guide to the components of the base multi-electrode array. The copper posts necessary to the network architecture, while the point contact platinum electrodes are imperative to the readouts of the network for later computation. . . 52

5.3 ASN input process used for spoken digits. Raw audio was broken into overlapping windows, each of which was converted to 13 MFCCs. These were arranged to minimize input thrashing for the ASN, and then passed as input to a single electrode. The final prediction was based on a linear combination of the remaining electrodes; see text for details. . . . . 58

5.4 UV-Vis of silver thin films before and after iodization using ambient and heated methods. . . . . 60

5.5 XPS spectra of silver-based devices exposed to (sample, red) or withheld from (control, black) iodization procedure. Characteristic peak for iodide 3d5/2 at a binding energy of 620 electron volts (eV) are absent in those devices withheld from iodization. In contrast, this peak is present in those devices exposed to iodization procedure and is consistent with previously reported spectra for metal iodides. 61

5.6 Mean ± standard deviation of accuracy for different input frequencies, input voltages, and regression modes, computed across different electrode combinations and the linear logic functions IN0, IN1, and AND. I - inputs only. N - read electrodes only. R - full reservoir readout. . . . . 61

5.7 Identical layout as fig. 5.6, but showing statistics only for XOR to demonstrate non-linear results. Statistics are therefore computed across electrode combos, demonstrating the variability of choosing different input electrodes. . . . . 62

5.8 Recall of the input from $\tau$ bits in the past. While 10 Hz only had enough data to test up to $\tau = 4$ prior bits, it demonstrated perfect recall. 5000 Hz on the other hand demonstrated linearly-decaying recall, consistent with capacitive or inductive effects. . . . . 63

5.9 XOR between the current input and the input $\tau$ bits in the past. Like fig. 5.8, 10 Hz demonstrated perfect accuracy. Unlike recall, this illustrates that the prior results were stored in a non-linear manner, allowing for richer computations. 5000 Hz did not outperform the naive baseline, indicating slower input was required. . . . . 64

5.10 Mean and standard deviation for tapping the temporal sequence of spoken digit MFCCs at $N$ different points, and regressing to identify the digit spoken. This plot shows that the "R" readout method avoided overfitting and provided some benefit over using the inputs directly ("I" mode). See section 5.3.4 for precise formulation of this plot. . . . . 66

6.1 (a) mRNA relative expression over the time course of hESC differentiation toward cardiac lineages. The value is standardized to the peak value of the time points for each gene. (b) Immunofluorescent staining for $\alpha$-actinin in red showing over 90% are positive for $\alpha$-actinin (scale bar = 100 um) (c) Morphological changes in hESC-CMs over the time course. Representative optical images of hESC-CMs on MEA on Day 20 and Day 35 (fluorescent staining: $\alpha$-Actinin in green, nucleus in blue, scale bar = 10 um). (d) mRNA relative expression by qPCR standardized to the expression of day0 over the time course of cardiac differentiation/maturation. . . . . 73

6.2 (a) Microelectrode arrays (MEA) with 120 integrated TiN electrodes (30 $\mu$m diameter, 200 $\mu$m interelectrode spacing) were used to culture the 2D hESC-CMs. (b) Representative optical image of hESC-CMs on top of MEA. (c) Field potential signals were detected in electrodes which are in touch with the hESC-CMs. . . . . 73

6.3 (a) Field potential features such as beat interval, field potential duration, amplitude, and local activation time (LAT) were extracted out of the signal sequences. On average, 100 out of 120 channels were selected to calculate the beat interval after the peak detection and experiments were performed in triplicate. (b) The beat interval was stable up to day 28–30 with a beat interval around 2 s. Starting from day 28, the beat interval of hESC-CMs became unstable and irregular. The standard deviation ($\delta$) of beat interval agreed with the beat interval trend. (c) The field potential duration (FPD) ranged from 0.2 s to 0.5 s and was relatively stable throughout the differentiation process. (d) The corrected FPD ( = FPD/[beat interval/1000] 1/3 ; Fridericia's formula) was also relatively stable ranging from 0.2 to 0.3. . . . . 75

6.4 Peak mean amplitude (a–c) and mean beat interval (d–f) of field potential of monolayer cardiomyocytes cultured in the presence of (a,d) E4031 ($K^+$ channel blocker), (b,e) TTX (tetrodotoxin, Na$\hat{+}$ channel blocker) and (c,f) Nifedipine (Ca$\hat{2}$+ channel blocker). p-values are calculated by one-way ANOVA. Data are representative of at least 2 biological replicates. . . . . 77

6.5 Field potential propagation, pacemaking and conduction velocity of the 2D hESC-CMs. (a–h) shows a representative activation map from day 19, 20, 21, 22, 25, 26, 28, 29, respectively. The activation map was consistent over the 20-minute recording window showing a stable pace making source, but the propagation map changed over days. (i) On day 23, a contour graph of the propagation wave was generated from the activation map. (j) The center of the propagation wavelet was identified by fitting the wavelet with a circle. The origin of the circle represented the location of the pacemaking cells. The pacemaking cells were located at the edge of the MEA. . . . . 79

6.6 (a) The field potential amplitude rapidly increased until day 23 and declined at day 27. The turning point agreed with that of the beat interval. (b) The field potential amplitude upstroke speed increased from 15.3 $\mu$V/ms at day 18 to 122.9 $\mu$V/ms at day 26 and declined at day 27. (c) Conduction velocity was calculated at each day. There was an increment of conduction velocity as the development of hESC-CMs. Results from two samples were consistent. 80

# Acknowledgements

This degree would not have been possible if not for the shoulders of giants to pave the way and give me something to stand on. Thus, in addition to my creative and complex advisor Jim Gimzewski whom I love and respect tremendously, I must strongly acknowledge those that stood before me and next to me during this degree. Particularly Adam Stieg, whose invaluable guidance has kept me in the program, Henry Sillin that trained me, Odo's crystal growth work, Christina's cleanroom fabrication techniques, Renato's simulations, and Ellie for recruiting me into the group in the first place. Additional collaborations with Juan Pablo-Carbajal formerly in the reservoir lab at Ghent University and Walt Woods from the Teuscher group have kept ideas and energy flowing. Local collaborations with Volker Strauss and Yolanda Lee have kept life at UCLA more interesting, and an undergrad named Michelle Phi has helped considerably in converting analysis codes into Python. NSF funding played a major role in my staying for the whole degree. Furthermore, a degree such as this would have never been possible without the support and love of friends and family. To all the friends I've made in the program I am eternally grateful for their effortless presence in their own skin, all extremely intelligent and as kind as anyone that has ever known what it feels like to be viewed as weird. I've never felt so at home with a group of people, nor do I ever expect to again. To my parents for loving me, my siblings for their love and encouragement, and of course Rachel for holding me up and leaning on me as two trees supporting one another for a thousand years.

**Chapter 2** is a highly condensed summary based on thesis author contributions of Demis, E., Aguilera, R., Sillin, H., Scharnhorst, K., Sandouk, E., Aono, M., Stieg, A., Gimzewski, J. "Atomic switch networks – Nanoarchitectonic design of a complex system for natural computing," Nanotechnology, Apr. 2015. and carries with it the following acknowledgements: The authors would like to thank Audrius Avizienis and Cristina Martin-Olmos for their past contributions to this work. This work was partially supported by the Ministry of Education, Culture, Sports, Science and Technology (MEXT) World Premier International (WPI) Research Center for Materials Nanoarchitectonics (MANA) and the Defense Advanced Research Projects Agency (DARPA)—Physical Intelligence Program (HR0011-10-1-0008P00005), US Department of Defense. The authors acknowledge use of the Nanoelectronics Research Facility (NRF), Molecular Instrumentation Center (MIC) and Nano and Pico Characterization Laboratory (NPC) at the University of California, Los Angeles. Authors would also like to acknowledge the Integrated Systems Nanofabrication Cleanroom (ISNC) for access to fabrication equipment and clean room facilities.

**Chapter 4** is a version of Scharnhorst, K., Carbajal, J., Aquilera, R., Sandouk, E., Aono, M., Stieg, A., Gimzewski, J. "Atomic switch networks as Complex Adaptive Systems" Japanese Journal of Applied Physics, Volume 57, Feb. 2018, and carries with it the following acknowledgements: Authors would like to acknowledge Henry Sillin for his software engineering work in LabView, especially the current-controlled feedback loop. Additionally we thank Christina Olmos for her foundation work in device fabrication protocols. Funding from NSF, SRC, HP and the International Center for Materials Nanoarchitechtonics (MANA) supported this work. We would also like to acknowledge the Integrated Systems Nanofabrica-

tion Cleanroom (ISNC) for access to fabrication equipment and clean room facilities.

**Chapter 3** is a version of Scharnhorst, K., Woods, W., Teuscher, C., Stieg, A., Gimzewski, J. "Non-temporal Logic Performance of an Atomic Switch Network," Proceedings of the 2017 IEEE/ACM International Symposium on Nanoscale Architectures (NANOARCH), Newport, RI, Oct. 2017, and carries with it the following acknowledgements: The authors gratefully acknowledge Sam Lilak for capturing SEM images of the device, and past group members: Christina Martin-Olmos, Henry Sillin and Audrius V. Avizienis for their foundation work in chip fabrication, LabView programming and crystal growth, respectively. Physical ASN chips were fabricated in the Integrated Systems Nanofabrication Cleanroom (ISNC) at the California Nanosystems Institute (CNSI). This work was partially supported by the Research Center for Materials Nanoarchitectonics (MANA), HP, and NSF. This work was also supported by DARPA under award # HR0011-13-2-0015. The views expressed are those of the author(s) and do not reflect the official policy or position of the Department of Defense or the U.S. Government. Approved for public release, distribution is unlimited.

**Chapter 5** is an unpublished manuscript and carries with it the following acknowledgements: The authors gratefully acknowledge past group members: Christina Martin-Olmos, Henry Sillin and Audrius V. Avizienis for their foundation work in chip fabrication, LabView programming and crystal growth, respectively. Physical ASN chips were fabricated in the Integrated Systems Nanofabrication Cleanroom (ISNC) at the California Nanosystems Institute (CNSI). This work was partially supported by the Research Center for Materials Nanoarchitectonics (MANA), HP,

and NSF. This work was also supported by DARPA under award # HR0011-13-2-0015. The views expressed are those of the author(s) and do not reflect the official policy or position of the Department of Defense or the U.S. Government. Approved for public release, distribution is unlimited.

**Chapter 6** is a version of Huanqi, Z., Scharnhorst, K., Stieg, A., Gimzewski, J., Minami, I., Nakatsuji, N., Nakano, H., Nakano, A. "Two dimensional electrophysiological characterization of human pluripotent stem cells derived cardiomyocyte system," Nature Scientific Reports, Mar. 2017, and carries with it the following acknowledgements: Authors thank Jinghua Tang in BSCRC stem cell core for the technical support. This work was supported by supports from NIH (R21HL124503), Oppenheimer Foundation and Center for Duchenne Muscular Dystrophy at UCLA. H.Z., K.S.S., H.N. and I.M. performed the experiments and analyzed the data. A.Z.S., J.K.G., N.N. and A.N. designed and supervised the project. H.Z., K.S., A.Z.S. and A.N. wrote the manuscript. 

# Vita

| | |
|---|---|
| 2013 | B.S. Chemistry |
| 2013 & 2018 | Eugene V. Cota-Robles Fellowship, UCLA |
| 2015 | M.S. Chemistry - Materials |
| 2015-2018 | National Science Foundation Graduate Research Fellowship Program (NSF GRFP) |

**Publications**


[1] Scharnhorst, K., Carbajal, J., Aquilera, R., Sandouk, E., Aono, M., Stieg, A., Gimzewski, J. "Atomic switch networks as Complex Adaptive Systems" Japanese Journal of Applied Physics, Volume 57, Feb. 2018.

[2] Scharnhorst, K., Woods, W., Teuscher, C., Stieg, A., Gimzewski, J. "Non-temporal Logic Performance of an Atomic Switch Network," Proceedings of the 2017 IEEE/ACM International Symposium on Nanoscale Architectures (NANOARCH), Newport, RI, Oct. 2017.

[3] Huanqi, Z., Scharnhorst, K., Stieg, A., Gimzewski, J., Minami, I., Nakatsuji, N., Nakano, H., Nakano, A. "Two dimensional electrophysiological characterization of human pluripotent stem cells derived cardiomyocyte system," Nature Scientific Reports, Mar. 2017.

[4] Demis, E., Aguilera, R., Scharnhorst, K., Aono, M., Stieg, A., Gimzewski, J. "Nanoarchitectonic atomic switch networks for unconventional computing," JJAP, Sept. 2016.

[5] Aguilera, R., Demis, E., Scharnhorst, K., Aono, M., Stieg, A., Gimzewski, J. "Morphic Atomic Switch Networks for Beyond-Moore Computing Architec-

tures," IITC/MAM 2015 IEEE International, Grenoble, pp. 165-168, May 2015.

[6] Demis, E., Aguilera, R., Sillin, H., Scharnhorst, K., Sandouk, E., Aono, M., Stieg, A., Gimzewski, J. "Atomic switch networks – Nanoarchitectonic design of a complex system for natural computing," Nanotechnology, Apr. 2015.

# Chapter 1

# Introduction

Natural systems abundant in emergent phenomenon exist all around us in the natural world and comprise of complex structures and behaviors. A flock of birds, a swarm of bees. A pile of sand. Anything involving heat transfer, or pressure gradients. Economies, ecosystems, stock markets, biological processes, the list goes on. Earth itself is an incredibly complex natural system consisting of innumerable fractals of systems branching upwards in complexity like the branches of a tree. When a system has a dynamic response to a feedback loop, it can continually adapt. Intelligence emerges via a fine set of fault-tolerant rules telling where a bird should fly in 3D space with respect to others in the flock and at what velocity. Swarm intelligence such as this is known as an emergent property. Consciousness can be seen as a spontaneous evolution from the complex entanglement of interacting synapses. Our brains consist of long and short range connections which are non-trivially weighted to one another, in that all weights are different through space and time. Although there is compartmentalization within the brain, information storage occurs on the same platform as processing and is incredibly interconnected. This

allows for mammals to process mutli-sensory information, fetch data from memory, and come to a conclusion almost instantly when it comes to object recognition, decision making, prediction, and time-dependent problems. On top of all this, the brain is extremely low power. The term computer came about in 1804 and was used to describe a human doing a calculation, it transformed with the invention of computers to describe a machine performing a calculation. So, although the english language has transformed the meaning of 'computer', biological synapses are some of the most complex computers known to man.

In order to solve and/or model more and more complex problem a revolutionized platform will be required. When an individual element of a system lacks a property the system as a whole exhibits, there exists emergent phenomenon. Emergence, simply put means that the whole is greater than the sum of it's parts. This thesis will primarily address the question of how to characterize and harness such a system in the form of a bio-inspired microchip with individual elements similar to those of a mammalian synapse. The inspiration for this work stems largely from an area called neuromorphic computing, presented in the 1960's by Carver Mead. His work focused on using analog hardware to emulate brain-like activity for problem solving. These early chips were based on analog metal oxide semiconductors (MOS), and after 35 years of research analog learning was shown via a single synapse transistor. However, explorations in digital computers exploded and led to the complementary metal oxide semiconductor (CMOS) integrated circuits used in digital computers today.

Computing today has two main limitations that the research presented here attempts to overcome. Both Moore's Law and the Von Neumann Bottleneck hinder the continued progress of integrated circuits (IC). While the first states

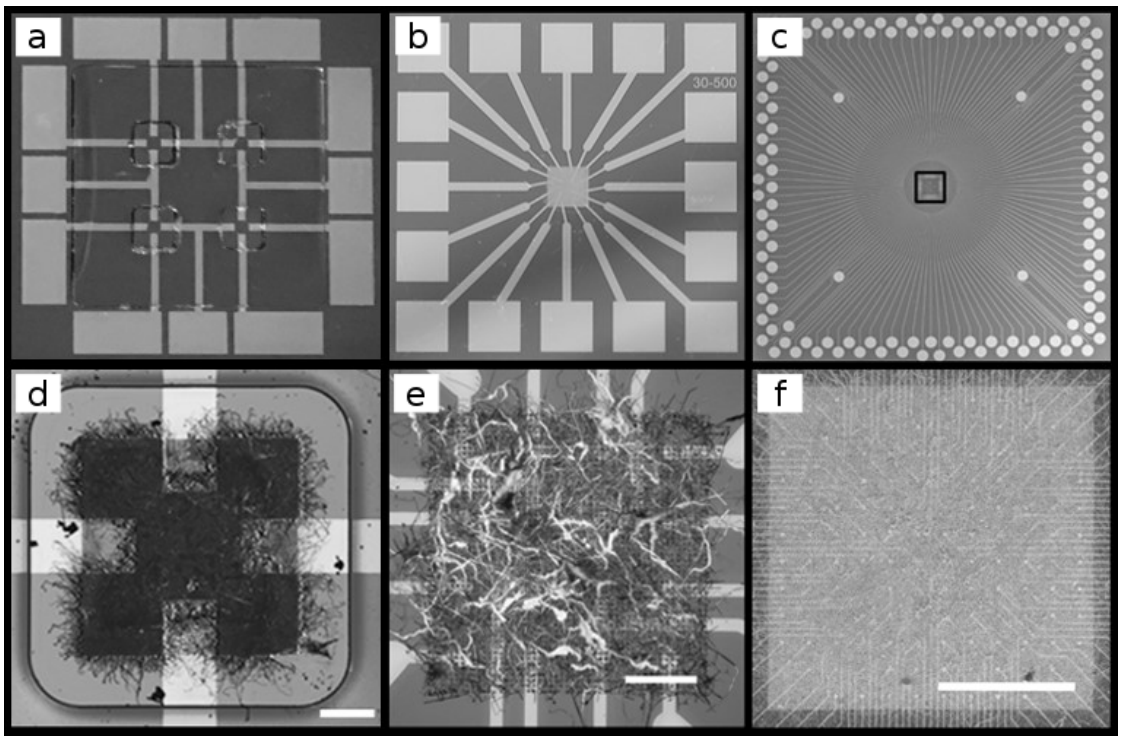


Figure 1.1: The ASN went through different generations. Electrode numbers increased from two, four, sixteen up to 128. Work presented in this document began by optimizing the fabrication process for the 128 electrode devices.

that the number of transistors per IC doubles every two years, this law is coming to its end upon reaching the theoretical and financial limits of individual circuit element packing. At a certain point the increased cost outweighs the advantages of increased processing power from the decreased size of transistors. The Von Neumann Bottleneck also acts as a hurdle for increasing the computational complexity a system is capable of. This bottleneck refers to the backup of information caused by the separation of the storage/memory and processing components of a personal computer (PC). Information transfer is the slowest portion of task performance. Thus, to circumnavigate both packing density and transfer limits would allow for faster computing using more individual circuit elements.

Fabrication begins in a clean room where standard lithographic techniques are used to pattern a grid of 5umx5um seed sites, 300 nm tall. Then, through the use of self-assembly densely packed interconnect junctions arise via an electrochemical reaction called electroless deposition, where as the name suggests a chemical reaction occurs without applied electricity. A seed atom that has a higher affinity towards a carrier ion which is bonded to our desired end material will swap positions. At the end of these metal atoms assembling through stochastic waves of brownian motion we are left with silver wires varying in thickness, length, and structure. There are two ways to grow branching structures caused by mullins-serka instabilities, (1) altering the concentration of the ions in the wavefront, or (2) varying the seed site size which changes the surface area exposed to ions. If all the molecules in contact with the seed site have switched positions and are now stable entities, then there is a depletion region causing an influx of ions from the sides leading to a branch being born. The entropy to grow out to the side rather than straight forward becomes energetically favored. Through the careful consideration of past grad students, it has been found that extremely branched elements exhibit less reliable behavior than wires. A such, the work herein contains microchips with densely packed nanowires that are functionalized by cladding the metal spaghetti with an insulator. Individual elements are thus metal-insulator-metal (MIM) junctions which have been shown to exhibit short-term and long-term memory based on input frequency, amplitude, and duration. Each neuromorphic chip produced during this work contains approximately 1E8 junctions/cm2 and have been shown to exhibit behavior similar to the human brain. A brief history of chips is shown in fig. 1.1.

# Chapter 2

# Atomic Switch Networks for Alternative and Unconventional Types of Computing

Naturally occurring complex systems based on self-organization are abundant in this world and can be used as inspiration to construct new types of operational nanotechnology using an abundance of interacting units in a network. Size and interconnect density scaling limits hinder the continuation of standard integrated circuit (IC) fabrication to handle higher complexity problems. This section focuses on fabrication methodology of a self-organized complex device and its potential for computing. Atomic switch networks (ASNs) were designed to combine highly patterned top-down techniques with a self-organized bottom-up assembly. Individual units have an inherent memory and an ability to transform information via nonlinear dynamics. The unique nonlinear and memory properties of the ASN support its potential use in natural computing, such as reservoir computing – an

area that looks at the computing ability of biologically-inspired complex systems.

### 2.0.1 Materials and methods

#### 2.0.1.1 MEA fabrication

Using a silicon wafer 500 $\mu$m thick and 100 $m$m in diameter, a 500 $n$m thermal oxide is deposited to act as the substrate for the MEA that connects to hardware and the user interface. Electrodes patterned in a 4x4 array connect to outer electrode pads that connect to hardware via gold spring loaded pins. The MEA consists of a 5 $n$m Cr wetting layer and a 150 $n$m platinum layer via exposure of a photoresist with UV rays and metal evaporation. Different electrode pad diameters were used: 20, 30, and 50 $\mu$m while changing the spacing of these pads from 200, 300, and 500 $\mu$m. Wafers are dehydration baked for 10 min at 150and cooled for two minutes. In addition, a 400 $n$m SU-8 layer is used as an insulating layer to allow point contacts. The SU-8 is spin coated and photolithographically patterned, post-exposure baked, developed, rinsed in IPA, baked, and diced.

#### 2.0.1.2 Network fabrication

Many network fabrication methods were explored using metallic nanostructures to form a functional complex system. These methods lead to three types of networks, those that are seed-free, random seed, or patterned seed networks. Seed-free networks result from pipetting 150 $m$L of monodisperse silver nanowires (120-150 $n$m x 20-50$\mu$m, Aldrich) in an isopropanol suspension (149.8 $m$g Ag/L). To fabricate a random seed network, 1 $m$L of copper microspheres (1-10$\mu$m, 99.995% purity Alfa-Aesar) is dropped onto the center of the MEA and allowed to air dry. Next a

20 $\mu$L of 50 $m$M silver nitrate ($AgNO_3$) is dropped in the center of the chip to allow for the electroless deposition of silver that leads to dendritic branching structures. To fabricate a highly patterned grid of copper seed sites, an oxidized silicon wafer is coated with 2 $\mu$m of AZ NLOF 2020 and soft baked. A grid is patterned via UV photolithography, post-exposure baked, developed in MF26A, and rinsed with isopropanol. Copper (300 $n$m thick) is deposited via metal evaporation, then soaked in acetone overnight for liftoff, and spin-rinse dried. Finally, the chip is placed in 5 mL of 50 mM $AgNO_3$ for 40 min and leads to dense and interconnected network of silver nanowires.

#### 2.0.1.3 Network functionalization

Silver nanowire networks have up to $10^8$ junctions where two structures cross and are functionalized into working MIM switches via sulfurization with $S_8$ gas at $10^{-1}$ Torr, and 130°C for 5 min to form atomic switches of Ag—$Ag_2S$—Ag. To form a fully coated $Ag_2S$ layer, the sulfurization process is repeated until at least 75% of electrode combinations have a resistance above 1 M$\Omega$.

#### 2.0.1.4 Network testing

The interface module, shown in figure fig. 2.1, for the ASN device was 3D printed (MakerBot Replicator 2.0). The device was placed in the base of the module, which attached to a locking head holding 16 spring-loaded pins used to contact each outer MEA electrodes for the interface of the device to measurement hardware. A source measure unit (National Instruments Model 4141) was used in combination with two data acquisition cards (National Instruments Model 6368) and a switching module (National Instruments Model 2532) to define the input/output (I/O) functionality of

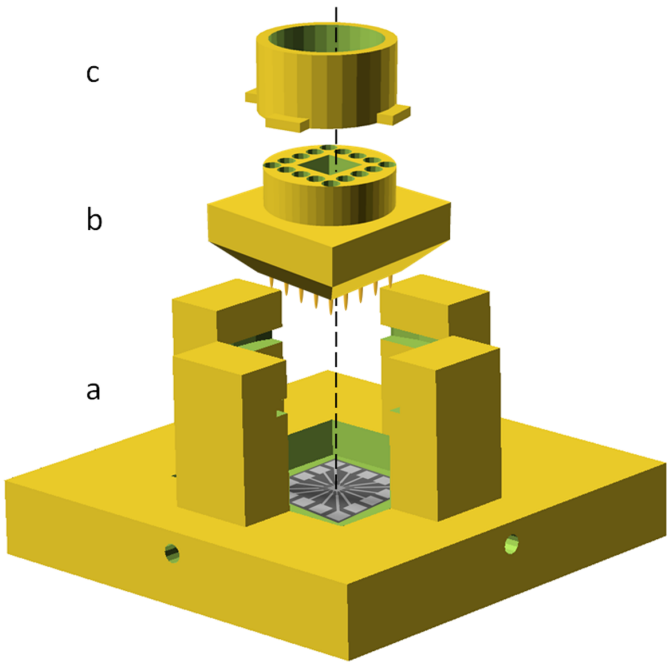


Figure 2.1: Device holder. Above is a computer aided design schematic of the custom 3D printed sample holder to interface with the ASN device. The main components are (a) the device holder, (b) electrical interface with gold spring-loaded pins that make contact with the platinum electrode pads of the ASN when (c) the interlocking component is twisted into the posts of (a) the device holder. The gold pins in (b) are wired into measurement hardware.

each MEA electrode, deliver/measure I/O signals and collect simultaneous, spatially-defined voltage traces. Control software for the ASN device was coded in LabView 2012 (National Instruments) to synchronize voltage and current acquisition, input arbitrary voltage signals, record any combination of electrodes, measure resistance between electrodes, input real-time signal feedback, and log data. Subsequent data analysis was conducted in Matlab 2010b (Mathworks).

### 2.0.2 Results and discussion

Networks of complex interconnected operational nanoarchitectures were purpose built via top-down meets bottom-up fabrication techniques. Functional networks consisted of drop cast monodisperse nanowires, or the ELD of metallic nanodendrites, or nanowires. Finding positives and negatives of each technique, the nanoarchitecture with patterned seeds led to the most reliable density. As such, the size of patterned seed site was varied to maintain density control and maximize the connectivity of individual atomic switches. Interacting switches produce a complex network capable of memory and information transformation. On top of this, emerging electrical activity from interacting elements span the entire network over time. Natural computing requires memory and nonlinear functionality.

#### 2.0.2.1 Structural and functional complexity of the network

Both structure and function of natural systems are closely intertwined. The complex structure of ASNs allows for emerging complex behavior of the network as a whole. Fabrication of these networks examined reproducible control over structure, density, functional diversity, and reliable operational control. ASNs have been fabricated via drop-casting of monodisperse nanowires, drop-casting random seed sites, and photolithographically patterning seed-sites. While all three have been shown to exhibit emergent behavior, memristive IV-curves, and power laws, the structural variances cause changes to the reliability of network function. Monodisperse wires held no control over the dispersion of the structure over the network and thus opened up potential for unused point contact electrodes, as well as exhibited a coffee ring effect. Additionally, the monodisperse nature of the nanowires did not lead to a large variation in functional parameters such as

the ON/OFF thresholds of atomic switches and thus limits the potential for non-linear transformations towards computing. Drop cast seed-sites allowed for much larger variation in ON/OFF thresholds; however, the density was uncontrolled and not always dispersed evenly across the MEA. Lastly, patterned seed-sites allowed for functional diversity, areal density, switch density, and operational control. Parameters for the highest level of unique dispersed elements included optimizing the concentration of the electroless deposition solution, and studying varying seed sizes [4, 73].

These patterned seed networks allow for complex functionality in the form of entangled interactions between individual atomic switches in the network. Electrical activity of ASNs is distributed through space and time and cannot be determined by a single switch, but only the network as a whole 2.2. Applied voltages at the input electrode move through the wires and non-trivially activate atomic switches which govern the flow of current. This distribution of electricity throughout the network is constantly reconfigured via the completion of a filament at one switch causing a local potential drop, or the breaking of another switch at a different location causing a local potential spike. In this way the network is inherently re-configurable and adapts. This forms the potential for learning in the field of natural computing, and more specifically artificial neural networks.

The resultant switching interactions lead to a constantly changing local and global potential map across the network, facilitated by the distribution of wire diameters and lengths. The diameters form different insulator widths, requiring different voltage levels to facilitate cation migration, and therefore different degrees of short and long-term memory [19]. The shorter wire lengths make nearest-neighbor con- nections and promote local interactions; longer wire lengths make long-range

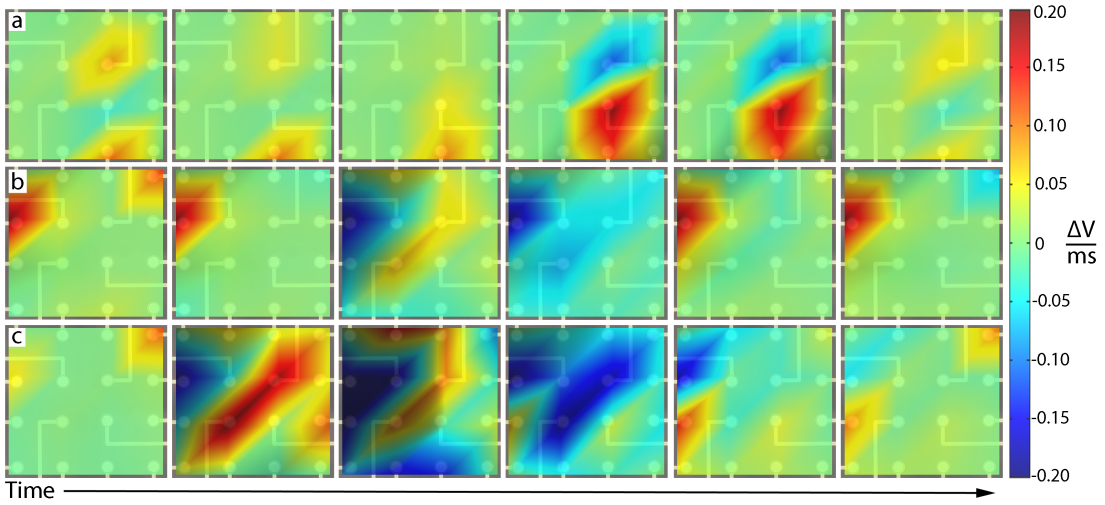


Figure 2.2: Distributed switching activity. Each row (a)–(c) represents activity of a patterned seed network (2 mm by 2 mm) for 3 ms (0.5 ms frame rate) at each electrode with a 5 V DC bias input at the upper right corner and a ground at the lower left corner. (a) Localized switching activity (b) switching activity localized to upper left corner (c) distributed switching activity that affects the entire network.

connections that promote global interactions [1, 21]. The degree of the switching event can therefore be categorized as local or global. These two types of switching are presented in figure 5. Various methods have demonstrated that the ASN does not adapt a static switch configuration [21, 23]. Application of a bias allows the network to adopt different resistance states by initiating switching events, which continually reconfigure the network in time. The different resistance states of the network are mea- sured by recording the electrical potential at different loca- tions using the MEA. While the networks are densely intricate, monitoring of bias over the network is only done at each electrode. This is an inherent disadvantage to under- standing intricate network dynamics as only the portions of the network that are in direct contact with the electrodes are monitored. To create a representative potential map of the network a smooth function is utilized to connect the biases of neighboring electrodes to create a more legible potential map. However, it is

important to note that discrepancies in the smoothed portion of the representation are undoubtedly pre- sent and discontinuities of bias are possible depending on the topology and behavior of the network that is not in direct contact with the electrodes.

These potential drops or spikes can be observed in a potential map of the network (2x2 mm) through time (0.5 ms windows over 3 ms in each row) in order to visually observe the magnitude of the perturbation as well as the fluctuations between high and low resistances. 2.2 presents a sequence of images representing the changes in electric potential at each measurement electrode in the ASN device. During periods of low switching activity, the network reaches a metastable state [10, 23], and the potential recorded by the electrodes remains nearly constant, as seen in the first three frames of figure 5(a). Localized switching is best represented in figures 5(a) and (b) by the changes in voltage observed at only one or two electrodes. Distributed switching activity in the ASN is represented in figure 5(c) to show global changes in potential due to an extensive switching event. The result is that activity in the ASN is comprised of metastable configurations punctuated with reconfigurations of varying degree [23]. This distribution of event sizes is reminiscent of patterns of activity in the brain that spatially distribute input signals, taking a one dimensional signal and mapping it into a higher dimension [2]. In natural computing, the spatial distribution of signals emulates the representation of information transfer in biological neural networks and produces the capability for solving complex problems [8].

### 2.0.3 Conclusion

To evaluate ASNs as a physical platform for complex natural systems, they have been fabricated with multiple processes with different structures. Monodisperse nanowires have dynamic activity, but are not density controlled and each element is like that of the rest. Nanoarchitectonics are proposed to combine a seed-directed DLA process with standard photolithography. Using nanoarchitectonic concepts we designed a network formed from silver nanostructures via DLA growth. The process itself was based on mathematical concepts and theoretical predictions and is thermodynamically driven, leading to a large number of varying atomic switches that produce robust behavior distributed in space and time. By using copper micropheres the structure of silver nanoarchitectures obtained were controllable, but their contacts and density were not. Patterned uniform grids of seeds via lithographic processes allowed for not only reproducible and controllable density, but also contact with the electrode pads, and a highly interconnected network.

ASN devices show switching activity distributed across the network in in the form of nonlinear transformations across time, this arises due to nanowires varying in size and insulator thickness. Individual MIM junctions have memristive properties in the form of a memory based on the frequency and amplitude of an applied bias. When these individual elements are connected within a complex network, behaviors more complex than that of an individual arise. The potential map of the ASN continually re-figures through the building and breaking of atomic filaments that reroute electricity in recurrent complex paths. Constant fluctuation of voltage throughout the network allows for the specific network state to map onto the output signals. Thus, another form of nonlinearity is present due to the vast number of atomic switching events.

Neural networks operate based on the strengthening and weakening interactions between individual neurons to solve problems and perform tasks. In the case of the ASN, the same principles are used to adapt to input stimuli and naturally compute. Through the use of a form of natural computing called reservoir computation, harnessing the unique properties of a complex dynamic system become possible. Reservoir computing needs multiple transformations of the input data to effectively problem solve. The ASN does just this via nonlinear transformations across the entire network, producing multiple dissimilar outputs. To surpass the limits of CMOS technology, complex dynamic systems limit power consumption while increasing information transfer. Through further fundamental studies, the ASN has potential as a state of the art hardware platform, that is CMOS compatible and capable of complex problem solving in the natural computing realm.

# Chapter 3

# Logic

Efforts to achieve a low-power, dynamically complex system become crucial as CMOS fabrication limits are realized. *Atomic Switch Networks* (ASNs) provide fabrication advantages over traditional CMOS through the combination of top-down and bottom-up techniques, leading to densely interconnected networks of atomic switches. ASNs show emergent behaviors through the interaction of individual non-linear elements. These properties make ASNs suitable for alternative computational paradigms, such as neuromorphic or reservoir computing. This work examined ASNs' ability to perform Boolean logic operations using non-temporal inputs based on randomized Boolean input streams. Zero and one bits were converted to negative and positive DC voltage pulses, respectfully. Next, a linear readout layer was applied to an array of voltage outputs from the device to reconstruct target output signals for the given task. ASNs produced nearly perfect results at low voltages for AND, OR, and NAND with more than 95% confidence. XOR, which requires non-linearity to solve, was able to be partially solved at high voltages with more than 95% confidence. As opposed to previous works which have investigated temporal

computation in ASNs, this work was the first to demonstrate semi-predictable, non-temporal, non-linear behavior within the device. Results demonstrated that the device connectivity is complete enough to perform complex computations.

## 3.1 Introduction

Alternative computing paradigms become paramount as interest in computation beyond CMOS grows, largely due to CMOS fabrication limits being quickly realized. In particular, bio-inspired computational paradigms have gained traction for their low power consumption and potential to solve complex distributed problems. Biological brains possess enormous computational efficiency, robust patterns of activity, fault tolerance and consume minimal power [8, 24]. Succinctly, these characteristics of the mammalian brain make it a model example of a complex cognitive platform [13].

We focused on neuromorphic systems and reservoir computing, both of which exist within the realm of bio-inspired computing. It is important to note that all bio-inspired computing falls under the larger realm of natural computing [16]. Contrary to the traditional Von Neumann architectures, bio-inspired computing seeks to combine data processing and storage on the same platform. Thus, these systems hold the potential to surpass the Von Neumann bottleneck, a time delay caused by the separation of data processing and storage.

Neuromorphic engineering, first proposed by Carver Mead in the 1980s, harnesses VLSI to mimic neuro-biological architectures [59]. Neuromorphic architectures focus on low power consumption, adaptability, and generating sparse outputs [91]. These systems provide a physical platform for alternative bio-inspired computing

algorithms. The most common of these is known as *Spike-Timing Dependent Plasticity* (STDP), but other high-performance spiking algorithms have been reported such as the *Simple Spiking Locally Competitive Algorithm* (SSLCA) [95]. Other recent relevant work in neuromorphic computing includes hybrid patterned crossbar networks of memristive synapses with complementary metal-oxide semiconductor neurons to implement synaptic functions such as STDP.

*Reservoir computing* (RC) is a system distinct from neuromorphic computing in that it requires no pre-training of the network and uses a dynamical system as a reservoir [25, 74]. RC is traditionally achieved by passing a time-varying input through a dynamic reservoir, harnessing a linear combination of the diverse output signals to reconstruct some target output. Physical platforms capable of RC have been limited to date, but have been increasing rapidly. Our work belongs loosely to this body of work, as the networks we will discuss demonstrate complex internal behaviors that, while untrained, can be harnessed for computation. Previous studies with *Atomic Switch Networks* (ASNs) have shown promise in reservoir computing through training output signals with a simple linear regression algorithm to meet various targeted waveform generations [17, 74].

These same ASNs have been shown to have an interconnect density of as many as $10^8$ switches/cm$^2$, achieved via a thermodynamically favourable self assembly reaction [77]. It's important to note fabrication costs for such a reaction are merely a fraction of standard lithographic techniques and are highly scalable. Individual atomic switches exhibit non-linear properties, and when part of a network interact in a dynamically complex way to produce emergent behaviors much more complex than those of single elements [17, 97]. These devices transform inputs into a higher dimensional space and thus provide a diverse class of output signals. In

addition, networks exhibit robust patterns of activity distributed in space and time and in turn are capable of fault-tolerance. This, combined with their inherent memory, recurrent structure, and non-linearity, provides a promising platform for computation [17].

Substituting self-organizing nanodevices for traditional computations has been proposed before. Tour  proposed building logic gates and performing other computations with a random, self-assembled nanocell accessed through I/O electrodes [88]. While this setup is excessive for logic functions, which are simple to implement in CMOS, the ability of a nanodevice to learn these functions indicates an ability to combine inputs in a variety of ways, leading to more complicated functions. Lawson proposed the idea of *Randomly Assembled Computers* (RACs) in 2006 [51]. In their work, random diode networks were constructed with a set of attached electrodes to access and control the random network. They also investigated random logic functions, as we did in this work. If the behavior of self-organizing nanodevices could be sufficiently defined, eventually these devices could be trained to be comparable to CMOS with the functions that they implement, while having the advantage that they could be re-trained.

In this study, ASNs were investigated as devices for non-temporal, or time-independent, logic computations. These combinatory non-temporal computations consist of simultaneously applying all input signals to the ASN, and reading the output values concurrently. However, unlike traditional combinatorial logic circuits, the underlying ASN changes during its computations. Non-temporal computation is robust in that devices require no intrinsic memory to perform the computation. Temporal computation, on the other hand, relies on time separation of the inputs and device memory. Non-temporal inputs were examined to highlight that real-

world ASNs exhibit non-linear, time-independent properties that have not been previously demonstrated.

## 3.2 Fabrication

A silicon wafer with a 500 nm thermal oxide functioned as the substrate for the microchip. A layer of NLOF 2020 was deposited onto the wafer and UV photo-lithographically (PL) patterned to deposit a 5 nm Cr wetting layer and a 150 nm Platinum layer. These layers were lifted off to expose 4x4 patterned platinum electrodes designed to connect ASN devices with experimental hardware (fig. 3.1). Pt electrodes of reported device are 30 µm in diameter and spaced 500 µm apart. A 400 nm insulating SU-8 layer was deposited to expose only point contacts of Pt electrodes, as seen in fig. 3.1. Again, NLOF 2020 was UV PL patterned onto which a 300 nm layer of copper was deposited and lifted off to provide a grid of 5x5 µm copper posts with 5 µm pitch. Thus, the end device consists of $Si/SiO_2$/Cr/Pt-electrodes/SU-8/Cu-posts.

Growth of silver networks utilizes a bottom-up approach employing copper posts as the seed sites for electroless deposition, or galvanic displacement. Microchips are then placed in an aqueous solution of silver nitrate (50 mM) for 60 min, rinsed in nanopure water and dried at 95°C for 2 minutes. This self assembly process of the silver structures is inexpensive, facile and follows the chemical equation below. Spontaneous reduction of $Ag^+$ metal cations occurs simultaneously with the oxidation of $Cu^0$ atoms, consistent with the cell potential (E°).

$$Cu^0(s) + 2\,Ag^+(aq) \longrightarrow {}_2Ag^0(s) + Cu^{2+}(aq)\; E^\circ = 1.26\,V$$

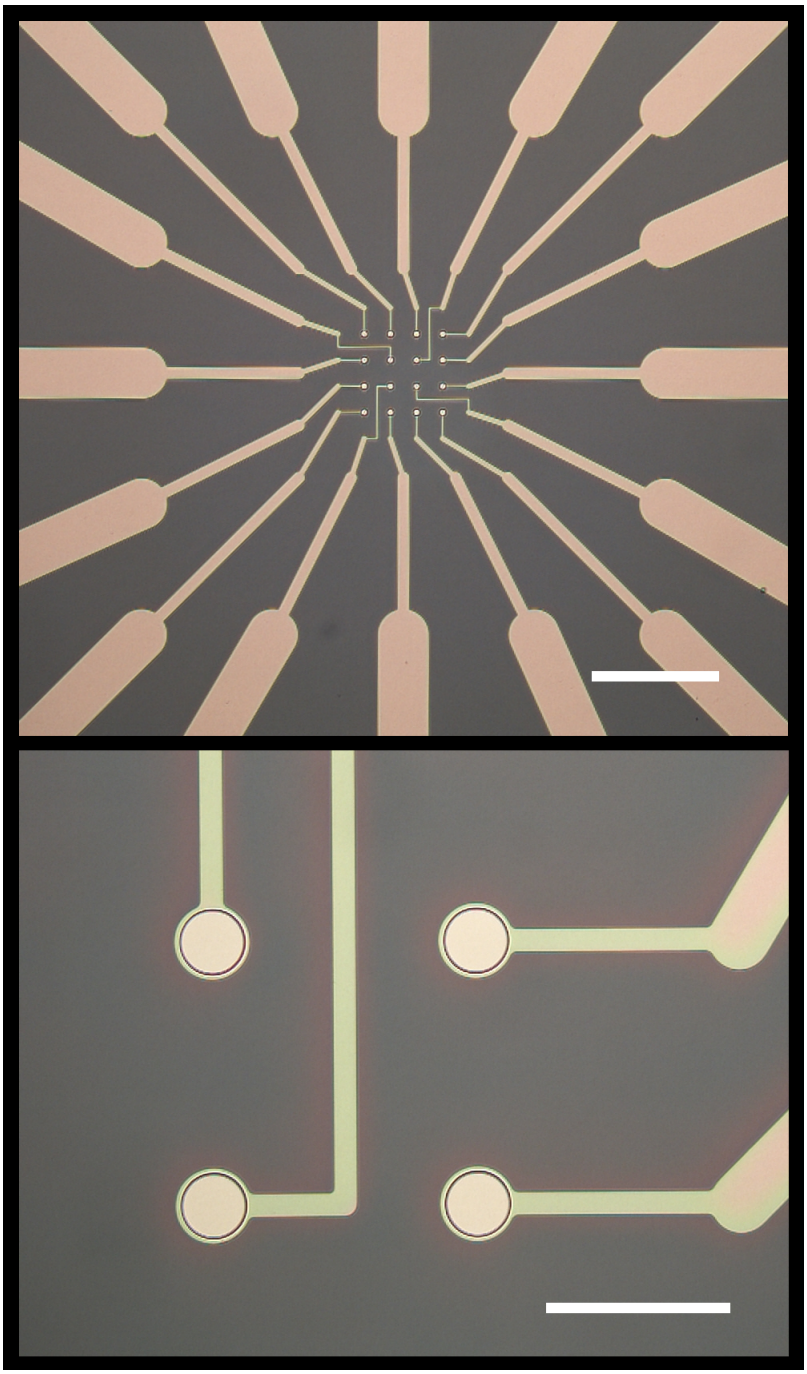

Figure 3.1: Optical images of the wafer with Pt electrodes and SU-8 layers present (scale bars = 1.5 mm and 500 $\mu$m, respectively). Pt electrode pattern (top) is covered in SU-8 except at inner point contacts of the platinum (bottom).

As previously reported, copper seed size, pitch, and solution concentration determine silver crystal morphology. Seed sizes below 3.5 µm produce nanowire networks through a process controlled by local crystal growth anisotropy, resulting in augmentation along Ag(111) planes [4]. On the other hand, seeds above 10 µm result in dendritic deposits due to depletion of the reactive solute species in the growth front [4]. This depletion of $Ag^+$ occurs at a rate capable of causing Mullins-Sekerka instabilities, or regions where the metal cation is consumed faster than it is replenished. Nearby, high density areas of metal cations build up causing branching structures to form, followed by more depletion regions. The device presented here builds off 5 µm seed sites and consists of a combination of dendritic and nanowire morphologies as seen in fig. 3.2.

Sulfurization of devices leads to system-wide functionalization of metallic intersections into metal-insulator-metal (MIM) junctions. A two chamber set up filled with inert gas is used to heat solid sulfur (99.5% purity, Sigma-Aldrich) in one chamber to 120°C concurrently with heating of the chip chamber to 95°C. After half an hour a valve is opened allowing an influx of sulfur gas to the device chamber. This functionalization allows for the complex system-wide dynamical switching activity distributed throughout space and time.

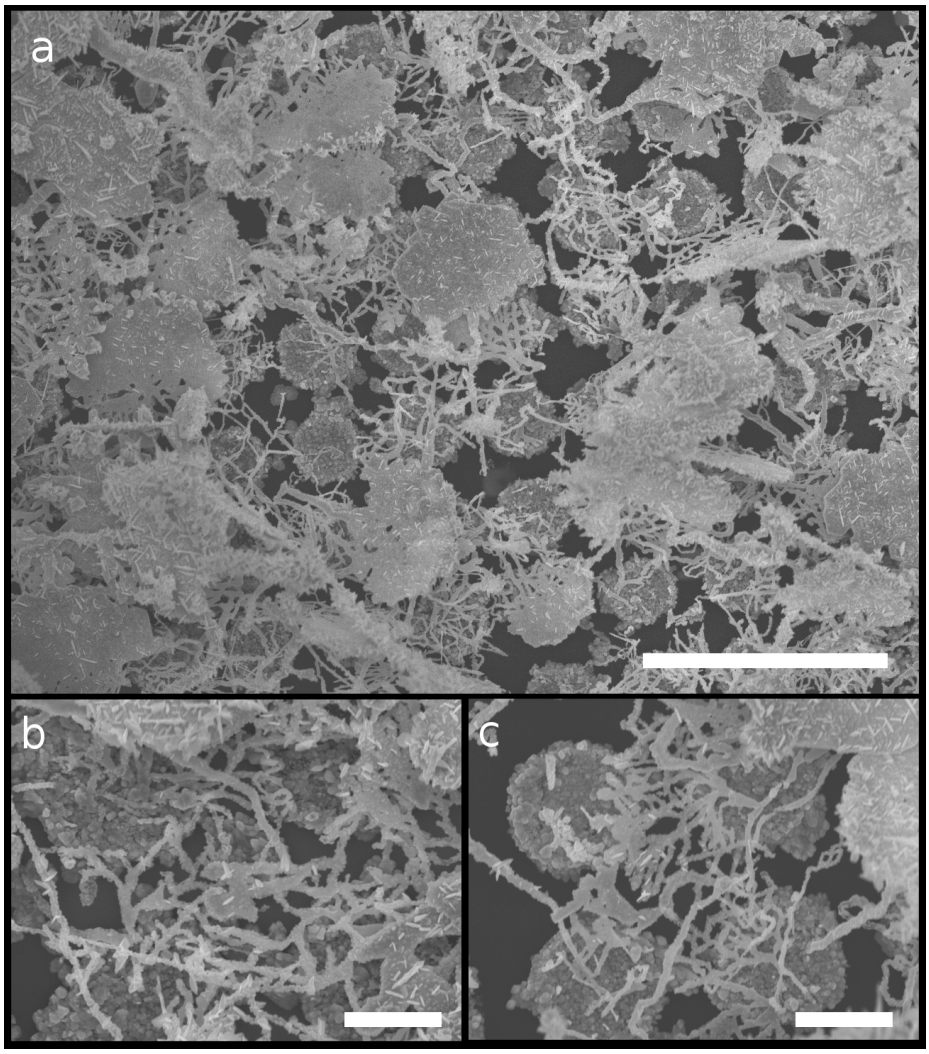


Figure 3.2: SEM images of the ASN device (scale bars = 20$\mu$m, 4 $\mu$m and 4 $\mu$m, respectively). Seed sites can be seen in (a), zooming in illustrates silver nanowires cladded in $Ag_2S$ crossing in the lower left of (b) and a dendritic structure originating towards the top right of (c).

## 3.3 Methods

To test the device's capabilities, we investigated its ability to reconstruct logic functions based on voltage input signals passed into the device.

All trials were preceded by ±3 V triangle waves. The purpose of this was to prime the device, and to give greater consistency to results. We investigated the capacity of the ASN to implement 2-input logic functions across a variety of randomly selected electrode combinations. In addition to the two input electrodes, a third electrode was grounded. Reads were done at different sampling rates, including 5 kHz, 50 kHz, 100 kHz, and 1 MHz. ASN dynamics in the framework of this study were found to be optimally captured at a 50 kHz sampling rate; thus, results presented used this read rate. Trials were run with inputs set to ±0.01 V, ±0.1 V, ±1 V, and ±3 V. An example of device data sampled at 50 kHz with two input signals of ±1 V is shown in fig. 3.3. Devices feature 16 electrodes: 2 inputs, 1 ground, and 13 output channels for data collection. Logic functions were learned based on readings from the 13 output channels.

To test the network's ability to combine and process inputs presented non-temporally, two bit streams were produced by duplicating all 2-bit permutations of 0 and 1 several hundred times and shuffling the resulting permutations. These bit streams were then applied to the electrode pairs as $+V$ volts when a 1 was present in the stream, and as $-V$ volts when a 0 was present. Each input stream was advanced at a given frequency $f_{in}$, and the ASN was sampled at a frequency $f_s$. Our system had noticeable 60 Hz noise on electrode samples, which was filtered using a Butterworth filter with 20 dB loss in the 55 Hz to 62 Hz range. The data points from each of the 13 output electrodes were then averaged throughout the duration of each input bit, omitting the first and last 2 data points per input. Least

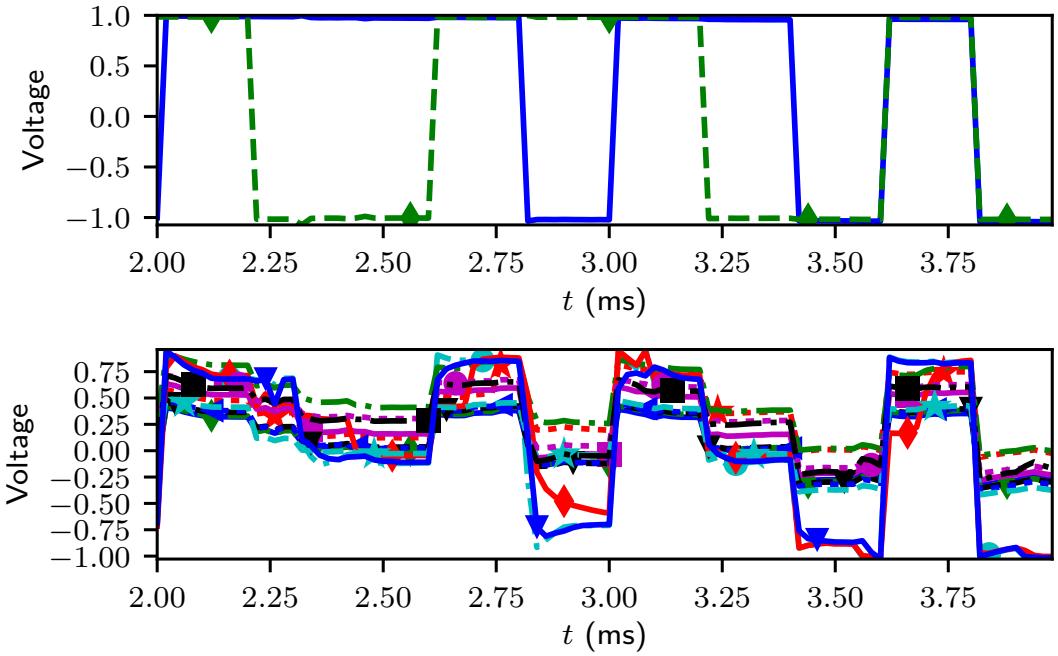


Figure 3.3: Voltage readings from $\pm 1\,\mathrm{V}$ input electrodes (top) and output electrodes (bottom). Data were sampled at $50\,\mathrm{kHz}$ with input bit frequencies of $5\,\mathrm{kHz}$. An ideal network would have a large range of values in the output electrodes.

squares regression was used to generate coefficients mapping these averages and a bias term (1) to the desired logic output. The regression was trained across varying lengths of training inputs, and then the resulting coefficients were tested across a subsequent number of testing inputs.

There was no overlap between the data used to fit the least squares regression and the data evaluated for accuracy. This was done to preserve the accuracy of the reported figures (no "double dipping" [45]). This setup also mimics the in-situ technique that is needed for these types of devices: since the ASN is volatile, the readout coefficients periodically need to be re-calibrated [94]. The time period for which coefficients are valid in the Ag—$Ag_2S$—Ag devices is discussed further in section 3.4.

Inputs were presented at 5 kHz, and electrodes were sampled at 50 kHz. Thus, pulse widths for each bit (0 or 1) were 10 ms long. Five different electrode pair and ground combinations were randomly selected and received two inputs. Four target logic functions were used: AND, OR, NAND, and XOR. The first three functions are linearly separable, meaning if the input signals can be reconstructed from the readouts, then perfect accuracy can be achieved. The last function, XOR, is not linearly separable, and any results better than a naive guess would require predictable, non-linear behavior from the ASN. For XOR, a naive guess results in 50 % accuracy, as each output option has equal weight. For AND, OR, and NAND, a naive guess results in 75 % accuracy. Due to this discrepancy, all accuracy results have been normalized such that 1 indicates perfect accuracy, and 0 indicates that the regression resulted in a naive guess. Standard deviations of output electrodes indicate the reliability of successfully learning a logic function with a single electrode combination at different points in time (fig. 3.4a and c).

In addition to presenting the accuracy statistics for a sample of individual electrode combinations, normalized accuracies were generated for all combinations of electrodes (fig. 3.4b and d). These numbers were constructed to be indicative of yield; accuracies presented for all combinations represent the accuracy at which we are 95 % confident a random electrode combination will outperform at any point in time. These were generated for each electrode combination at a given input amplitude by calculating the mean $\mu$ and the standard deviation $\sigma$ from each individual electrode combination's accuracy, taking $\mu - 1.65\sigma$ for each electrode combination, and then taking the mean and standard deviation of this quantity across all electrode combinations. Error bars are most simply described as the standard deviations of yield for different electrode combinations.

This methodology supplied information on the internal connectivity of the ASN, and the types of internal processing that was taking place. For example, applying an input to an isolated electrode would result in a failure to learn any logic functions. A lack of non-linear combinations of the inputs would result in no ability to represent XOR.

## 3.4 Results and Discussion

As the time-varying ASN inputs were utilized for non-temporal computations, we theorized that lower voltages would be the most effective. Non-temporal computations rely on a predictable internal state, which transforms the input in some way that is conducive to a fixed readout layer. Since the internal state of the ASN generally changes more with higher voltages, the readout layer would be less stable. This hypothesis was shown to be mostly true; comparing the results of 3 V and 0.01 V from fig. 3.4b and d, which was rendered from coefficients trained on 1000 input samples, the lower voltage produced more stable coefficients for AND, OR, and NAND. 0.1 V and 1 V were also tested, and produced results between these two situations, with more stability than 3 V and less than 0.01 V.

Results for AND, OR, and NAND tasks showed very high accuracy (fig. 3.4d). This indicates that the device possessed connectivity amongst all electrodes. Since AND, OR, and NAND are all linearly separable, the linear readout layer that we used would get 100 % on all of these if it had access to the original inputs. Since it did not, the readout layer relied on both inputs' data being present in the other electrodes. Physically this can be explained through the presence of complex connections in the device, ranging from long to short distances. Near-100 % performance on many different combinations of electrodes, with more than 95 % confidence in all cases, demonstrates that the inputs were properly disseminated throughout the network. Low voltages minimized network switching and could therefore be considered a read-only operation. Lower amplitude input streams performed better on the linear tasks and illustrates the ASN's suitability for non-reservoir applications. With the potential to implement more complex behaviors, ASNs might be used for cheap, high-yield neuromorphic hardware.

The network also demonstrated reliable, non-temporal non-linearities. This can be seen in fig. 3.4b, where the XOR function was learned better than the naive guess. XOR is not linearly separable, and thus if the ASN behaved only as a resistive network, the linear readout would never beat the naive guess. These effects were only prominent at high voltages; using 0.01 V was unable to learn anything about XOR (fig. 3.4d). The non-linearities are partially visible in the electrode reading diagram from fig. 3.3. These non-linearities demonstrate that ASNs might be used to realize more complex non-temporal computing functions than purely resistive networks. These non-linearities also add value in the context of reservoir computing, which highly values materials demonstrating rich internal functions.

As an additional point of interest and to show the stability of the linear readout, we include the accuracy heat map of linear and non-linear functions (AND & XOR) with respect to different numbers of both training and testing samples. At 0.01 V the accuracy of the linear functions increase with increasing training samples up to some point at which point the system could no longer increase in performance (fig. 3.5). In the presence of more switching, linear function accuracy is hindered; AND results are shown in fig. 3.6, but are representative of OR and NAND tasks as well. These results indicate that implementation of non-reservoir computing in ASNs would operate in a low switching regime. The XOR heat map at 3 V demonstrates that non-linearities in the device were subtle but reliable, requiring a large number of training samples, but also remaining valid for a large number of testing samples (fig. 3.7). Again, for these non-temporal logic tests, the target function relies only on the inputs at the current point in time! Though ASNs have been shown to have temporal properties that enable temporal computations, no investigation of device non-linearities when given a constant signal have been

previously presented. This result, and specifically the reliability of it, implies that ASNs might be used to realize a more diverse set of functions than previously imagined.

## 3.5 Conclusion

Evaluation of Boolean logic performance of an Ag—$Ag_2S$—Ag Atomic Switch Network device using randomized, non-temporal inputs were executed at multiple input voltages. Amplitudes of encoded inputs assessed were $\pm 0.01\,\mathrm{V}, \pm 0.1\,\mathrm{V}, \pm 1\,\mathrm{V}$, and $\pm 3\,\mathrm{V}$. Out of 16 electrodes, input and ground electrodes were randomly assigned, leaving 13 electrodes for readouts, which were linearly regressed to predict logic functions. The stability of the readout was investigated. Logic functions explored included AND, OR, NAND and XOR; linearly separable tasks (AND, OR, and NAND) exhibited nearly 100% accuracy for $\pm 0.01\,\mathrm{V}$ data at a 95% confidence level. This behavior indicated not only network connectivity, but also that ASNs have promise for reliable non-temporal, neuromorphic-style computations. The XOR function, which requires non-linearity to solve, was found to be partially solvable with more than 95 % confidence thanks to stable, non-temporal, non-linear behaviors in the device at $\pm 3\,\mathrm{V}$. These results highlight the need for further research on the computational capabilities of ASNs, especially for functions that would be difficult to realize in CMOS alone. We hope that this work, and the peculiar non-linear behavior of ASNs, can be used to inspire clever solutions in the future for a wide range of neuromorphic and reservoir computing applications.

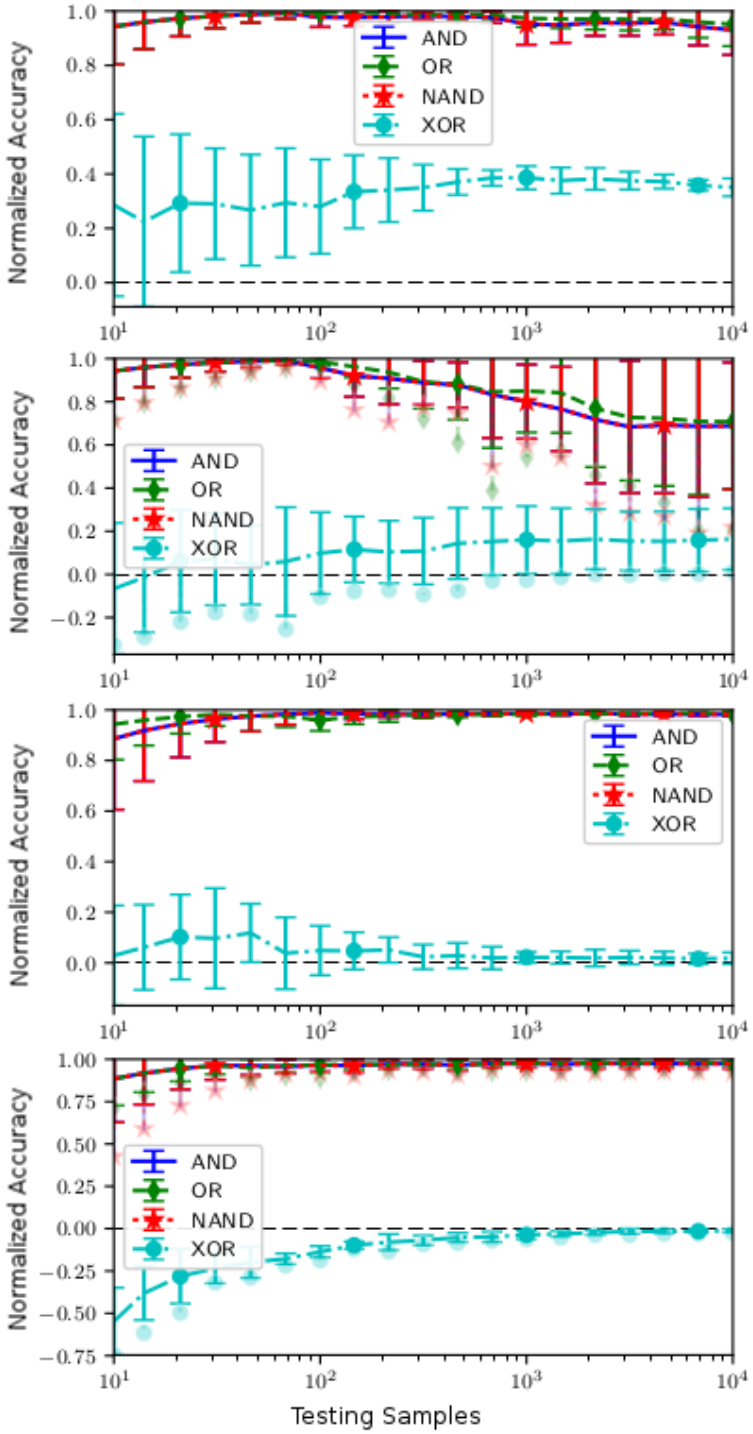


Figure 3.4: Accuracy on all logic functions learned using 1000 training samples. fig. 3.4a and fig. 3.4b used 3 V inputs; fig. 3.4c, (continued on the following page)

(caption cont.) and fig. 3.4d used 0.01 V. The left two plots represent normalized accuracy (described in section 3.3) of a single electrode combination. Error bars represent the standard deviations of the electrode combination's performance at different points in time. The right two plots are the 95 % confidence accuracies across all electrode combinations; that is, we are 95 % sure that a random electrode combination, at any point in time, will produce a regression that will outperform the mean line shown. Faded markers below lines indicate the worst-performing electrode combination's 95 % confidence accuracy.

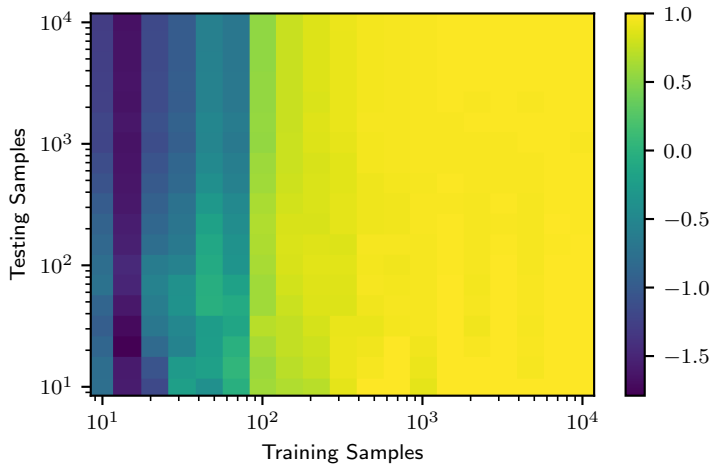


Figure 3.5: Accuracy of learning AND with 0.01 V inputs across different numbers of both training and testing samples.

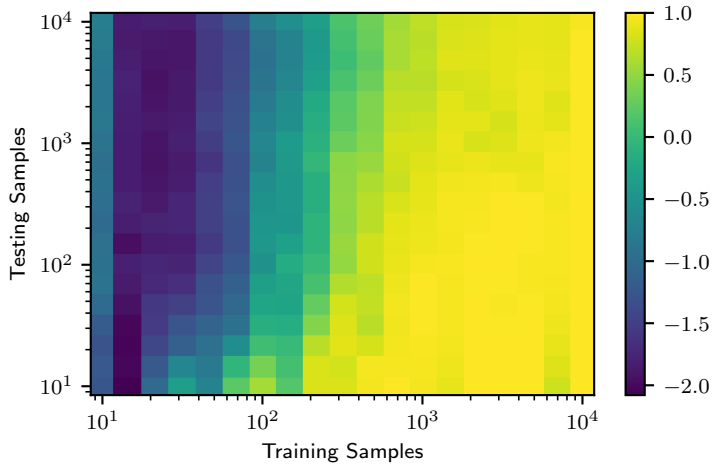


Figure 3.6: Accuracy of learning AND with 3 V inputs across different numbers of both training and testing samples.

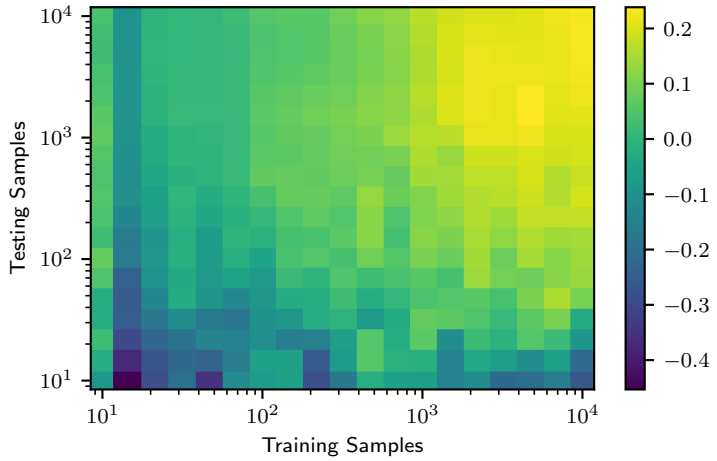


Figure 3.7: Accuracy of learning the non-temporal XOR function with 3 V inputs across different numbers of both training and testing samples. Beating the naive guess for XOR relied on non-temporal non-linearities in the ASN. Those non-linearities were stable, making regressed coefficients valid for a large number of testing samples.

# Chapter 4

# Complex Adaptive Systems

Complexity is an increasingly crucial aspect of societal, environmental and biological phenomena. Using a dense unorganized network of synthetic synapses it is shown that a complex adaptive system can be physically created on a microchip built especially for complex problems. These neuro-inspired atomic switch networks (ASNs) are a dynamic system with inherent and distributed memory, recurrent pathways, and up to a billion interacting elements. We demonstrate key parameters describing self-organized behavior such as non-linearity, power law dynamics, and multistate switching regimes. Device dynamics are then investigated using a feedback loop which provides control over current and voltage power-law behavior. Wide ranging prospective applications include understanding and eventually predicting future events that display complex emergent behavior in the critical regime.

## 4.1 Introduction

Complex Adaptive Systems (CAS) are the driving force behind many interesting phenomena that govern our world; they encompass everything from the behavior

of subatomic particles, to fluctuations in the stock market. As the name suggests, these systems consist of many complex interactions and are able to adapt within an environment. A short list of commonly studied CAS are global trade, markets, economies, neural networks, the internet, immune systems, and ecosystems, just to name a few.[34] Their importance continually increases as society becomes more globalized, and new large-scale interconnected systems arise.

Three main criteria classify CAS protean behavior. A system must first be uniquely interconnected: a network of individual elements must have a complicated and entangled relationship. Secondly, the network structure must be self-organized to minimize energy, maximize entropy, and cannot be determined by any single entity. Thirdly, there must be spontaneous emergent behavior that is solely a property of the network and not that of any single individual within the network.[49] These parameters enable CAS to operate and adapt through complicated interactions between functionally diverse elements encouraging a highly correlated, non-equilibrium critical state.

Self-organization drives the most interesting of the three criteria, emergent behavior.[53] The behaviors of the nodes or agents within the system, while seemingly random, all contribute in a specific way to create a larger behavioral pattern that is distinct from individual elemental behavior. The subsequent pattern within the system is the emergent behavior. In order to have emergent behaviors, the system must be in what is called the "critical state" or on the "edge of chaos".[9, 48] A critical state means that the system has found a metastable position between chaos and order, and small, local perturbations to the system can induce massive changes that ripple across the entire network in a nonlinear cascading fashion. Emerging behavior can learn from previous patterns in a recurrent feedback node,

such as neural avalanches in the brain.[9, 13, 69] A small stimulus may ignite one neuron that can potentially cascade throughout the brain, activating many different pathways throughout the network.[49, 78]

In this paper, we discuss the previously reported atomic switch network (ASN) in the context of CAS.[5, 17, 77] These recurrent complex networks demonstrate intrinsic nonlinearity as well as a capacity for cognitive memory and learning.[17, 18, 74] Spatial Lissajous curves highlight the distinct transformative nature of the network, or dynamic response. Finally, a feedback loop is implemented with I/O software and warrants control over the slope of current and voltage power laws. Results indicate the ASN functions as a CAS. Understanding the underlying rules that govern CAS could lead to a deeper understanding of how these systems behave, a task beyond the limits of current computational capacity.

## 4.2 Experimental Methods

### 4.2.1 Fabrication and Interfacing

Fabrication details of the ASN consist of a combination of top-down standard CMOS photolithography methods with bottom-up self-assembly, a full description of which can be found in Demis 2015.[18] Self-assembly of silver nanowire structures follow Eq. (1) below and are subsequently sulfurized using a carrier gas to form metal-insulator-metal (MIM) junctions.[4, 74] Examples of different stages in the fabrication process can be seen in fig. 4.1. Individual atomic switches exhibit non-linear behavior, quantized conductance, and short or long term fading memory based on the frequency and amplitude of the perturbing bias.[29, 66, 83] Not only do these elements inherently exhibit the properties just mentioned, but they also

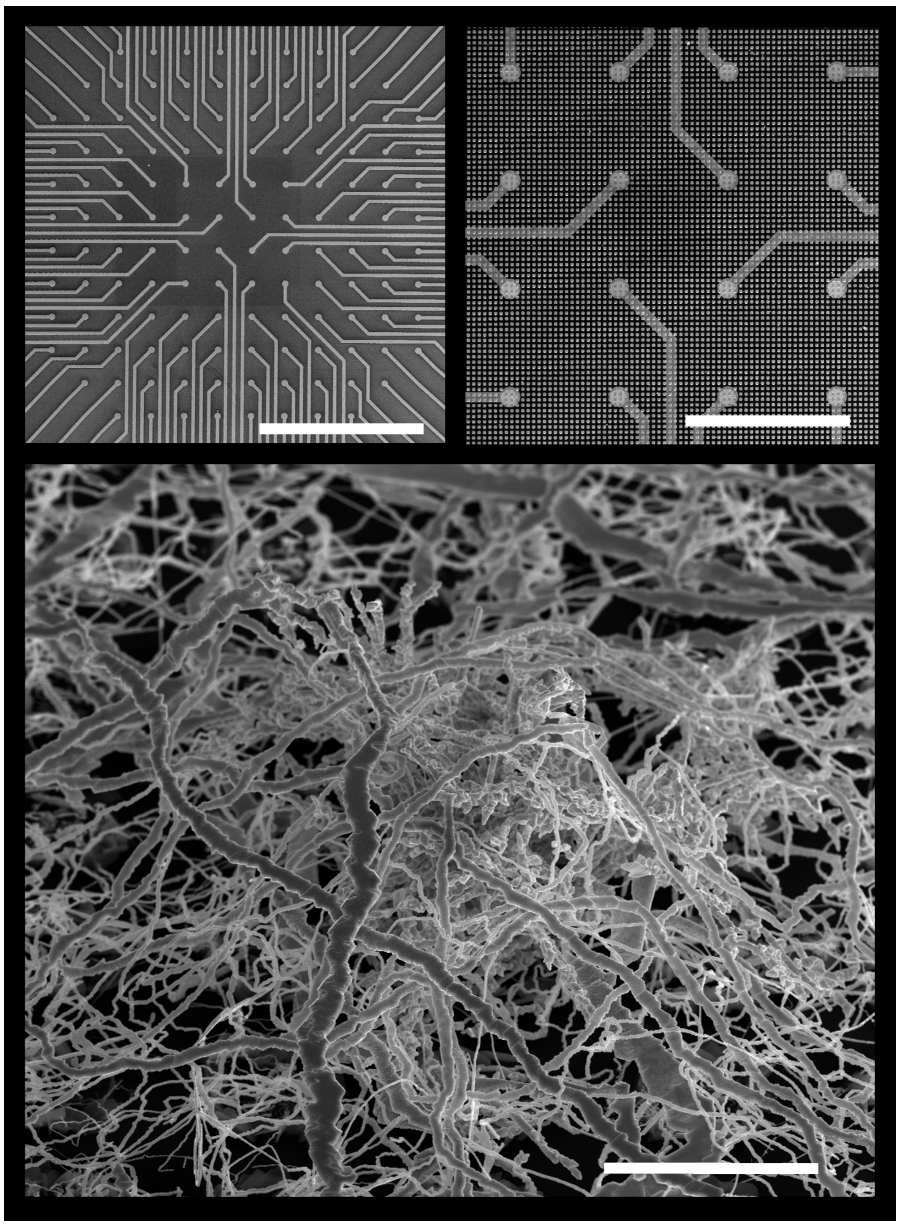

Figure 4.1: An optical image of an $SiO_2$ coated wafer with 120 Pt electrodes (top left, scale bar = 1 mm), a zoom in via SEM after SU-8 deposition to provide point contact electrodes which are covered by 5x5 $\mu$m Cu posts (top right, scale bar = 300 $\mu$m). Finally, an SEM of a self-assembled $Ag^+$ network after submersion in $AgNO_3$ (bottom, scale bar = 10 $\mu$m). See [18], Fig. 1 for design schematics.

have the capacity to be coupled with one another, making them the ideal building blocks for a system designed for complexity.

$$Cu^{0}_{(s)} + 2Ag^{+}_{(aq)} \longrightarrow 2Ag^{0}_{(s)} + Cu^{2+}_{(aq)} = 1.26 \text{ V} \quad (1)$$

Device input output (I/O) interface consists of an interlocking set up to make contact with outer electrodes, an example of a next generation holder with an optical image of a 120 electrode chip is shown in fig. 4.1. These contacts connect to measurement hardware which consists of eight shielded connector blocks, a source measure unit (National Instruments Model 4141), four data acquisition boards (National Instruments Model 6368), and a switching module (National Instruments Model 2532). This hardware paired with control software coded in LabView 2012 (National Instruments) that allows for sourcing of multiple input signals and concurrent recording of spatially distributed voltage traces which have been transformed through the complicated interactions of atomic switches. Post analysis work was conducted in MatLab 2010b and R2016a (MathWorks).

### 4.2.2 Non-linearity

Lissajous curves are powerful tools to understand the input-output behavior of systems excited with periodic signals and are a useful tool in analyzing continuous complex systems. A Lissajous plot allows quick identification of linear and non-linear relations between inputs, e.g. phase delays, frequency shifts, and harmonic generation. The detailed mathematics of Lissajous plots are described elsewhere (see Ref. [1] for a tutorial introduction), but the implementation of this analytical technique is straightforward: the output signal is plotted versus the periodic input

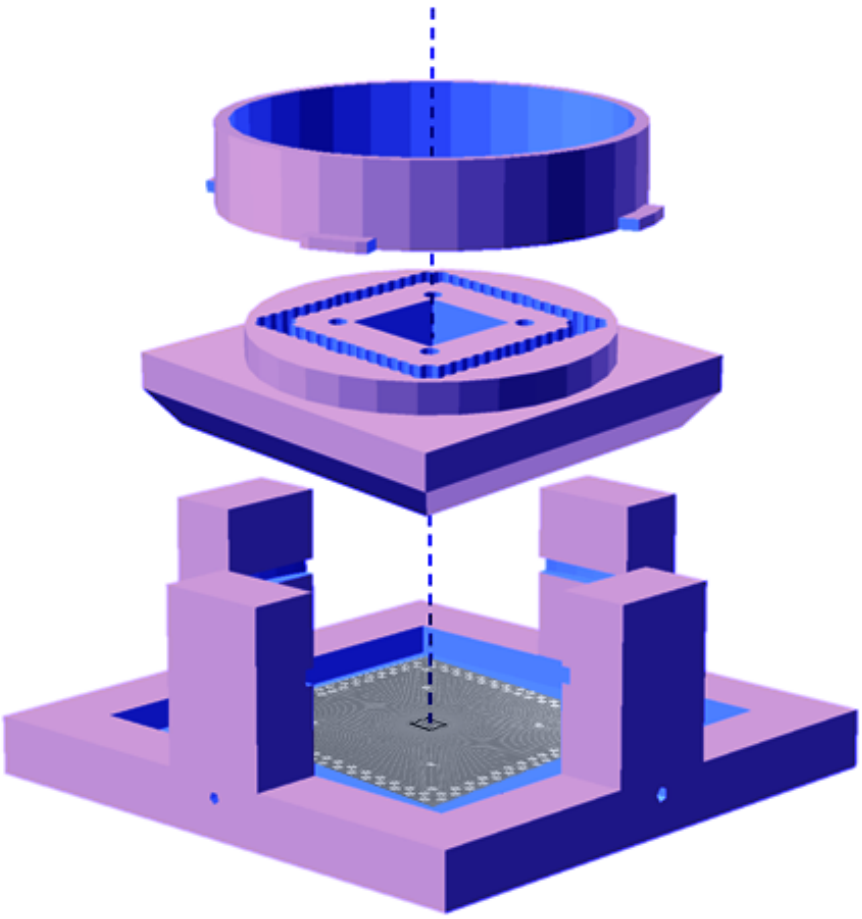

Figure 4.2: (Color online) CAD rendering of the 3D printed interface set up for the latest generation of ASN devices which include 120 electrodes with inner networks over four times as large as previous 16 electrode devices. 120 pins in the middle section make contact with outer device electrodes and connect to measurement I/O hardware when the upper portion is depressed and locked into place within the four posts.

signal.[1] The resulting plots are then interpreted using Eqs. (2) and (3) below:

$$x(t) = Asin(\omega t) \qquad (2)$$
$$y(t) = \sum_{i=0} a_i sin(\omega_i t - \delta_i) \qquad (3)$$

Where A, $\omega$ are the input amplitude and frequency and $a_i$ , $\omega_i$ , $\delta_i$ are the output amplitudes, frequencies, and phase delays, respectively. If the plot shows a diagonal line, the signals are proportional, i.e. $a_0$ A, $\omega_0 = \omega$, $\delta_0 = 0$ and all the other $a_i = 0$ . An elliptical plot indicates a phase delay between the two signals, i.e. $a_0 \neq 0$, $\omega_0 = \omega$, $\delta_0 \neq 0$, and all other $a_i = 0$ . A circle is observed in the particular case of signals in quadrature (a phase delay of 90 degrees). Any plot departing from these reference shapes (straight lines, ellipses and circles) indicate that the output contains frequencies that are not present in the input, and are the signature of a non-linear relation between the two signals. The strength of the departure from the reference shapes indicates the amplitude of the generated frequencies. If output frequencies higher than that of the input have sufficiently large amplitudes, the curves will intersect themselves.[26, 87]

Herein, Lissajous plots were used to describe the complex non-linear response of the ASN to AC inputs. These experiments were conducted on a 120 electrode device with 1 input, 62 outputs, and a grounded electrode to collect current through the network. The input signal was a bipolar 11 Hz sine wave with an amplitude of 1.0 V applied between the upper left corner of the ASN and the grounded electrode. The outputs correspond to the 62 measurements from the electrode array (y-axis). The data presented in later sections spans approximately one minute of recorded voltages.

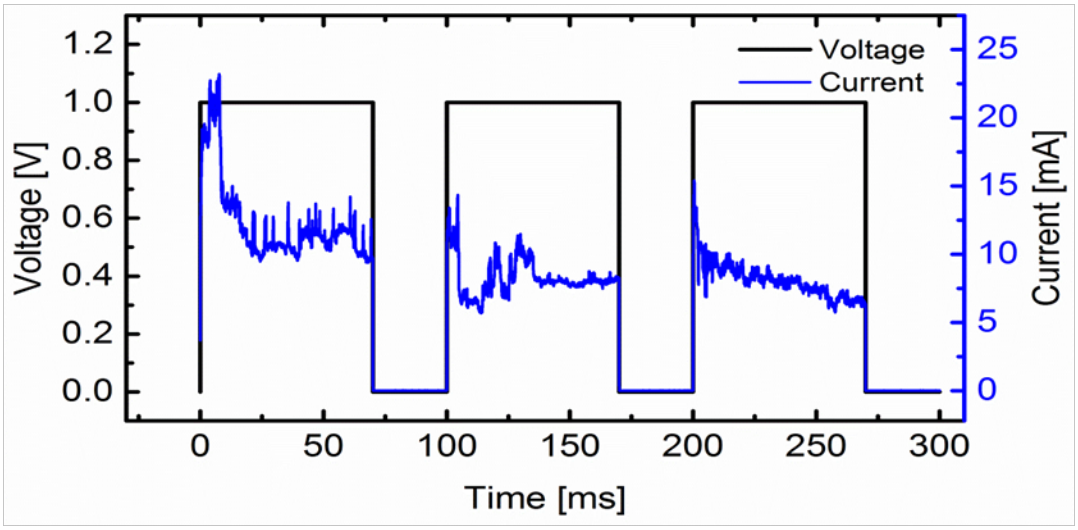


Figure 4.3: Representative example of the current-controlled feedback loop operating in real-time through control of the applied bias voltage (top) with the resulting current trace (bottom). In this example, the current set point modulated between 100$\mu$A and 500$\mu$A at 30s intervals and was monitored at a sampling frequency of 10kHz.

### 4.2.3 Current Control

A proportional-integral-derivative (PID) controller was used in conjunction with measurement hardware described in section 4.2.1 to control current flow through the system. PID loops are commonly used control systems that have feedback mechanisms of three different types. LabView implementation allowed for a current-controlled experiment. The voltage applied to the ASN was varied as seen fit by the PID to meet the current set point based on previous current values from the system (fig. 4.3). Data were sampled at a frequency of 10 kHz while the current set points fluctuated from 100$\mu$A to 500$\mu$A at 30s intervals and are illustrated as the red dashed line in fig. 4.3 The PID loop occasionally approaches the set point too quickly, overshoots, and results in an oscillatory period of adjustments, such as in the first pulse in the current trace below. However, this feedback loop processes

in real-time and adjusts weights of stimulation to coerce a critical system into a chosen state.

## 4.3 Results and Discussion

### 4.3.1 Non-linearity

The individual synthetic synapses, Ag—$Ag_2S$—Ag MIM junctions, function as nonlinear circuit elements and comprise a complex, dynamical system.[64] ASNs have been previously shown to exhibit the universally accepted non-linear activity metric of dynamic IV curves, such as soft switching, transitional, and hard switching (fig. 4.4(a-c), respectively).[77] In addition, evidence of higher harmonic generation in the device has been observed.[5] However, the ASN has never been characterized using V in vs. V out Lissajous curves to describe the complex harmonic motion between perturbations to the system and the mercurial array of outputs. Through these curves, which monitor the relationship between two oscillating signals, we can further verify the diversity of responses and network states throughout the ASN to see proportional, non-linear, and asymmetric behavior.

Varying degrees of non-linear output responses are perceived via Lissajous figures, which plot the input versus the output voltage signal to give a graphical representation of the relative harmonic motion of the two. Distinct transformational changes of the ASN are presented in fig. 4.4(d-f), showing multi-state switching regimes resembling those seen in traditional IV curves. An ellipsoidal response is the simplest case, demonstrating that these networks are capable of producing complicated pathways and resistance states which delay the phase of the input signal (fig. 4.4d). Non-elliptical plots mean that there are inherent non-linear

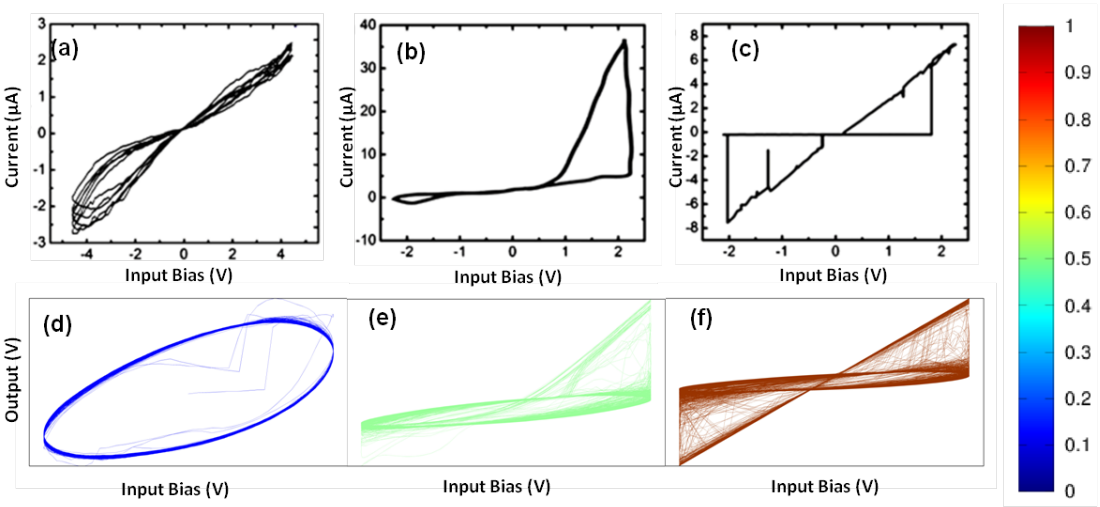


Figure 4.4: (a-c) shows IV curves of the ASN network when stimulated with a triangle wave input bias of ± 2.0 V at 10 Hz, exhibiting soft switching in (a), persisting until a conduction transition begins in (b), leading to hard switching in (c). Specific classes of V in V out Lissajous curves are featured in panels (d-f), and were stimulated by a ± 1.0 V sinusoidal 11 Hz input signal. Amplitude of the output signal corresponds to the value in the bottom right corner. Observed activity includes (d) initial pseudo linearity (containing short periods of non-linear responses), (e) asymmetric switching activity, and (f) bipolar switching activity. Channels intermittently converge and proportionally follow the input signal, resulting in the embedded elliptical shapes seen in (e) and (f).

transformations occurring from the spontaneous emergent switching activity. Interestingly, the device operates between two states: one that has minimal output activity and is nearly flat along the y-axis, and a second that pops up to readout asymmetric or symmetric traces proportional to the input (fig. 4.4e,f). However, there exist numerous complex transformations of the AC input that switch on and off at ever-changing thresholds. Lissajous curves further reinforce the idea that the dynamic response of the ASN produces complex activity and multiple operational regimes exist throughout the network at any given time.

To further evince the system's spatial-temporal activity and wide range of responses, these input-output plots were mapped onto the physical electrode locations on the device (fig. 4.5). A bipolar 11 Hz sine wave was input at the electrode marked with the red box (fig. 4.5, upper left corner), and the device was grounded at the electrode marked with the black box (fig. 4.5, above input, upper left corner). As expected, the input signal channel displays a direct linear relationship (a plot of input vs. input) and the ground electrode displays no significant relationship (noise) with respect to the input. For ease of comparison, fig. 4.4 is shown in fig. 4.5 within a blue box. Several channels in fig. 4.5 show an ellipsoidal shape indicating that their phase is shifted with respect to the input. These curves are not perfect ellipses and deformations are due to the non-linear processing of the ASN. Slight distortions in the elliptical shape are a consequence of steady dynamic changes to the signal's harmonic motion, but the predominant elliptical shape indicates that the system intermittently relaxes into a proportional response, with a mean signal value very close to zero (-1.9 x 10 -5 V).

Other channels similar to fig. 4.4(e) (highlighted with a green box in fig. 4.5) which show lop-sided switching and transformations of the input can be further

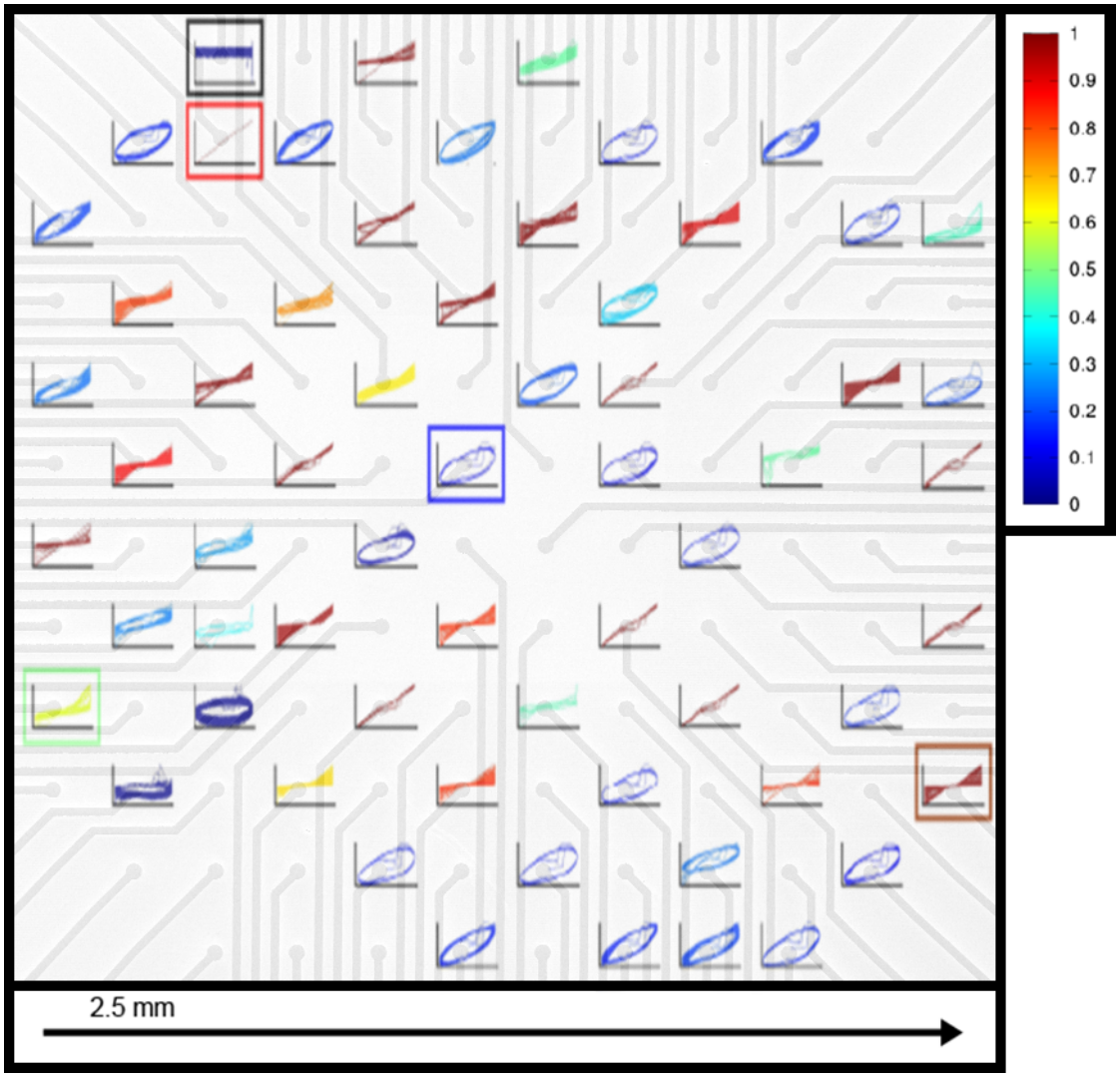


Figure 4.5: Each subplot is a Lissajous figure displaying one minute of the ASN's response to an 11 Hz, 1 V sine wave at 64 spatially distributed measurement points (Normalized output V vs. 1V input). The signal was input at the electrode marked with the red box, and the device was grounded at the electrode marked with the black box in the upper left of panel (a). Additional outlined subplots represent examples shown in Figs. 4(d-f). Color bar represents the amplitude of normalized output voltages through time.

described as having asymmetric pathways, or a polarity-dependent response. Since the bias read at the electrodes passes through an immense number of individual atomic switches, the resulting I/O perturbation follows a highly recurrent self-organized route through the network. The mean of this channel is 0.132 V, further supporting switch rectification somewhere along the complex pathway (fig. 4.4e). Finally, the symmetric traces in fig. 4.4(f) also yielded a near zero mean of 2.2 x 10 -3 V. Resistance changes in channels similar to fig. 4.4(e) and (f) heavily involve the formation and annihilation of atomic switches across the network. Behaviors stochastically move from proportional to non-linear responses via large scale cascading switching events.

The variety of behavior displayed in the Lissajous plots indicates that the ASN has the characteristics of a critical system. Self-organized growth leads to a uniquely interconnected system and fulfills the first two criteria of a CAS.[49] The localized regions of varying activity and behavior are reminiscent of the "edge of chaos" operational regime represented in well-known critical systems like the brain.[13] The "edge" happens at the critical transition between random/disordered and ordered states.[6] It is suggested that operating in this regime leads to maximum information processing and therefore computational capacity.[36, 52]

### 4.3.2 Control Dynamics

Results of the current controlled PID loop experiment yielded 1/f power law scaling for the two current set points explored, indicative of self-organized criticality, natural complexity and scale invariance (fig. 4.6 a-b).[6, 43] Similar trends were observed for voltage and current data. The power spectral density (PSD) of the output signal obeys a power law which may be manipulated by controlling the

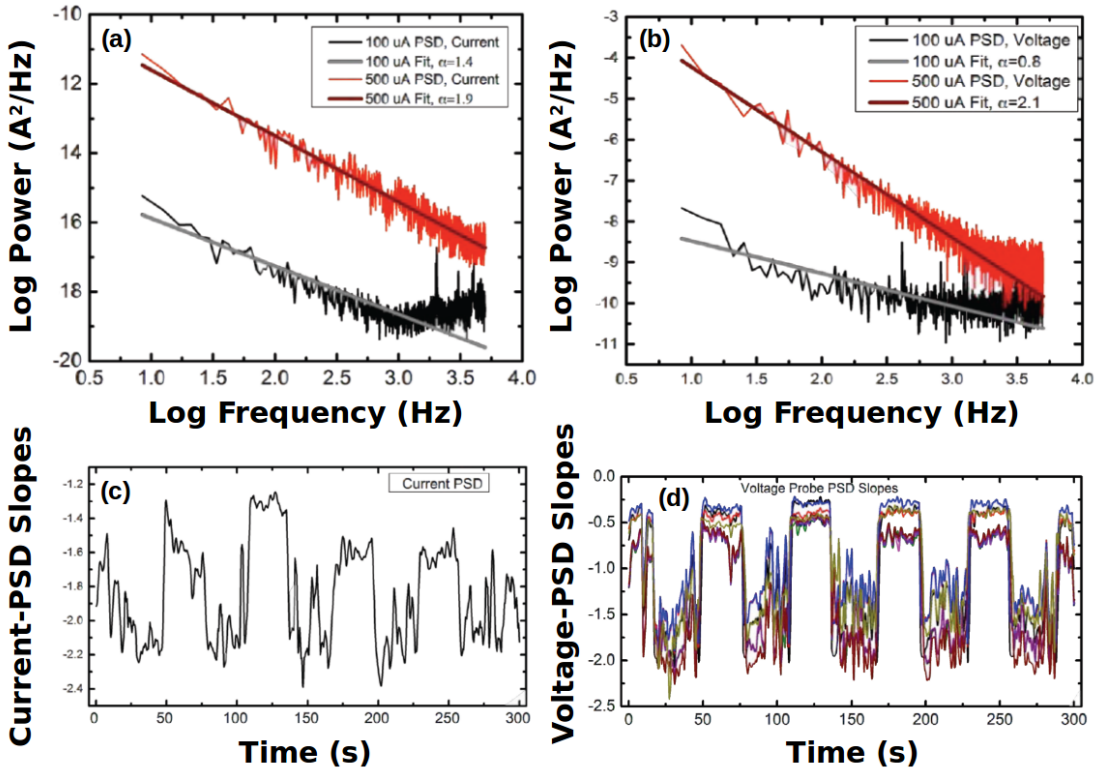


Figure 4.6: Plots (a) and (b) above show dependence of power law scaling (PSD $\alpha$ value) from current set point data presented in Fig. 3. The PSD slope ($\alpha$) of the current output is shown in (a) at currents of 100 $\mu$A and 500 $\mu$A and simultaneously acquired voltage (b). In all cases 1/f $\alpha$ scaling is present. Repeated cycling of PID loop and current set point demonstrated an ability to tune the PSD slope ($\alpha$), and hence spatiotemporal dynamics of the current output (c) and local voltage throughout the ASN device (d).

current output of the device. Repeated cycling of the control loop between these current set points demonstrated an ability to tune the PSD slope ($\alpha$), and hence spatiotemporal dynamics of the current or voltage through the network. While power laws themselves indicate a complex system, they do not substantiate a CAS unless the slope is variable such as in the mammalian brain.[8, 34, 35, 49] Thus, the adaptive response of the ASN indicates a CAS exhibiting spontaneous emergent behavior from a structurally complex system with entangled individual elements.

## 4.4 Conclusions

As the scope of our society becomes more global, we have seen the rise of many new complex adaptive systems (CAS), and understanding the ways in which these patterns emerge could lead to numerous applications in the realm of non-linear dynamical systems that produce complex emergent behavior. Atomic Switch Networks (ASNs) dynamics have been described via their spatially distributed non-linear response shown with V in vs. V out Lissajous plots. The device generates a wide range of outputs in response to an AC signal including phase shifts, and higher harmonic switching which substantiates the case of criticality in the ASN. A current controlled feedback experiment where the slope of the voltage and current PSD's were controllable is reported. Due to the recurrent functional topology of ASNs, the system is able to produce persistent critical dynamics. Exhibiting control over a critical network is noteworthy and furthers device potential in studying a wide array of CAS systems.

# Chapter 5

# Spoken Digit Classification Using AgI Atomic Switch Networks

Increasing computational complexity becomes difficult as the fundamental limits of Complementary Metal Oxide Semiconductor (CMOS) technology are reached. Highly interconnected, densely packed, low-power fabrics of nanodevices provide a potential alternative to CMOS. Here we examine a new material, AgI, for use in an Atomic Switch Network (ASN), which has previously been shown to have densely packed and entangled individual elements. Fundamental studies to verify AgI formation were conducted via XPS, and UV-Vis spectroscopy. The AgI chip was functionally tested via linear regression on basic logic tasks and spoken digit identification. Results showed that the AgI chip added computational complexity to a circuit, and was capable of computing XOR, a non-linear operation. The AgI chip also successfully demonstrated non-linear memory, and was capable of computing XOR across inputs at different points in time. The non-linear memory of the chip was also shown to be useful for identifying spoken digits, allowing fewer

data points to be regressed to achieve the same accuracy. This work motivates further exploration of ASNs as viable computational elements, without relying as heavily on precise CMOS fabrication.

## 5.1 Introduction

To address the ever increasing complexity of our world, alternative hardware is required to overcome information transfer lags between memory and processing, as well as packing density limitations. In order to circumvent the Von Neumann Bottleneck, new materials must demonstrate the ability to reliably solve complex problems that are either unsolvable or less efficient to solve through traditional silicon processes. In addition to this, they must be able to be packed closer than standard CMOS technology allows as the end of Moore's Law is reached [85]. Highly interconnected nodes within mammalian brains serve as inspiration for new computing systems with the goals of processing multi-input, chaotic, and/or temporal problems. Specifically, the densely packed and interconnected nodes of the brain are an ideal inspiration for finding solutions through emerging connective weights that vary based on previous inputs.

Individual atomic switches have been shown to produce non-linear responses, short and long-term memory, and quantized conductance [30, 82, 84]. These properties make them ideal circuit elements for use within a network towards complex problem solving. Continuing advancements in memristive hardware includes patterned cross bar arrays, and density-controlled self-assembled atomic switch networks [17, 82]. Previous work on silver atomic switch networks has utilized sulfur vapors and the subsequent formation of $Ag_2S$ as an insulating medium. The

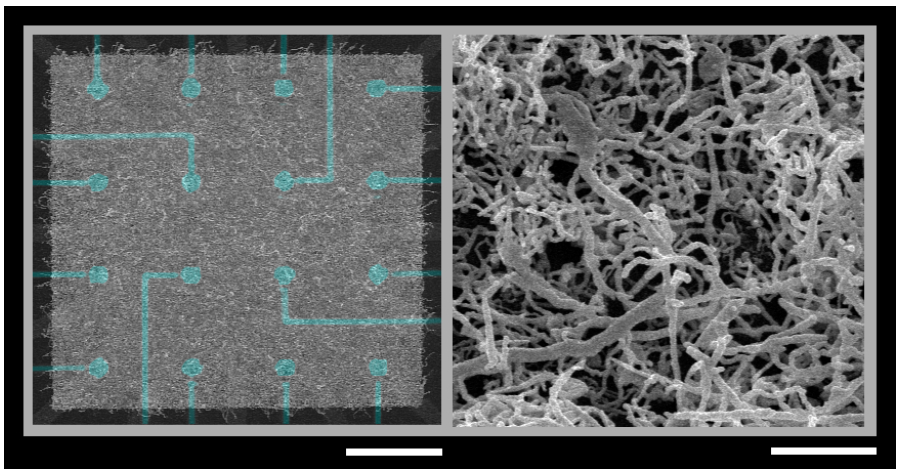

Figure 5.1: SEM image of an AgI ASN (left), transparency was set to 70% and overlaid on an optical image of point contact Pt electrodes shown in blue (left). The overlay allows one to visualize the inner measurement contacts which are 50 $\mu$m in diameter in the context of the entire network (1 mm$^2$). On the right is a zoomed in SEM image of the same network to illustrate the variety of wire lengths and diameters present. Scale bars = 250 $\mu$m and 10 $\mu$m, respectively.

sulfur deposition process is limited via a slow reaction rate and necessitates elevated temperatures, resulting in long deposition times [73]. Other studies have suggested that silver iodide may be utilized in electrochemical metallization memory cells with lower set voltages and a longer filament lifetime, yielding less volatility and potentially increasing the device's reliability [75]. The reaction rates of silver with iodine vapors are well documented and demonstrate that the reaction rate is inversely proportional to temperature allowing for a rapid functionalization process at ambient temperatures [72].

This work presents a new material for use in an AgI *Atomic Switch Network* (ASN). The formation of AgI films was characterized and applied as the insulating layer within a silver nanoarchitecture. The silver structure included long and short connections as well as wide and thin wires, lending to a variety of ON/OFF thresholds. Up to $10^8$/cm$^2$ junctions where two silver structures cross exist in ASNs,

allowing for potential atomic switch formation [77]. A vast number of switching elements with a constantly configuring network and a wide range of ON/OFF properties leads to non-linear transformations of input data, the basis of complex computation. As described in section 5.2, a *Scanning Electron Microscope* (SEM) image of the fabricated ASN is shown in fig. 5.1.

*Reservoir Computing* (RC) was used to evaluate the computational capacity of the AgI ASN. RC is inherently temporal in nature and can be used in many of the same situations as recurrent feed-forward neural networks. RC exhibits properties such as fault-tolerance, non-linearity, and learning [92]. Computational neural models such as the perceptron and support vector machine can also be used as reservoirs; however, long convergence times can be a drawback depending on the task. Material-based reservoirs have the benefit of not needing to be trained while providing similar computational qualities [38].

The AgI ASN material was evaluated by ensuring that the correct material was formed and functionalizing the resulting ASN (section 5.2), and testing the ASN's computational abilities on RC tasks relating to both logic and spoken digit recognition (section 5.2.1). Logic tests with RC were divided into both non-temporal and temporal sections, demonstrating the flexibility of the ASN in solving non-linear problems (sections 5.2.1.1 and 5.2.1.2). The results demonstrated that AgI ASNs are capable of reliably adding computational value to these tasks (section 5.3).

## 5.2 Methods

Silver iodide was formed via two different experimental techniques, one under ambient conditions and the other with added heat. To verify the formation of silver

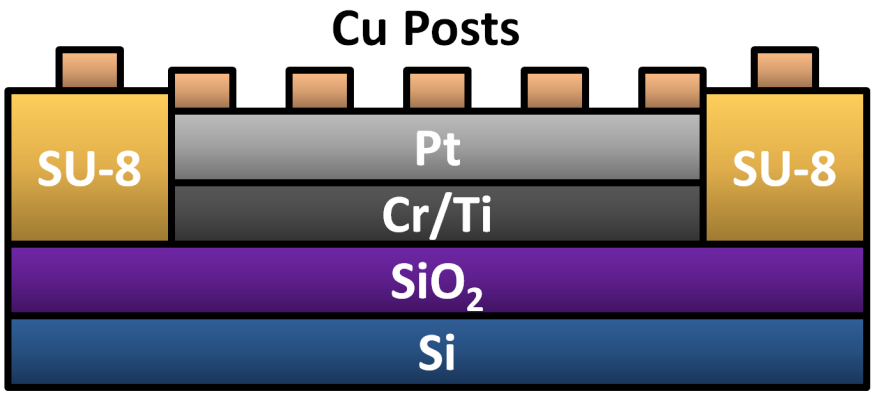


Figure 5.2: Layers of an atomic switch network (ASN) after top-down photolithographic fabrication methods are complete, prior to bottom-up assembly of a silver network. This schematic is not to scale, but can be used as a comprehensive guide to the components of the base multi-electrode array. The copper posts necessary to the network architecture, while the point contact platinum electrodes are imperative to the readouts of the network for later computation.

iodide, XPS and UV-Vis samples were prepared using transparent silver thin films (20 nm). These films were deposited on glass cover slides via a silver target in a Hummer 6.2 sputter system from Anatech Ltd (Hayward, CA, USA). In a negative 80 argon vacuum environment, the sputtering system operated at 15 mA of current. These samples were subsequently used in characterizing the presence of AgI.

ASN devices were fabricated on silicon wafers with a 500 nm layer of oxide deposited on the surface. Using standard photolithography techniques a 16 electrode patterned grid of 150 nm thick platinum is deposited using a negative photoresist (AZ NLOF 2020), and a 5 nm wetting layer of either Cr or Ti. Liftoff occurs over night in N-methyl-2-pyrrolidine (NMP) heated to 60°C. Point contact electrodes were isolated using an insulating layer of SU-8 (400 nm) which was soft baked at 90°C and developed in SU8 developer for 3 minutes and post exposure baked at 180°C for 30min. Again using AZ NLOF 2020 and UV light, a 300 nm layer of copper was deposited via metal evaporation at 3nm/s and lifted off over night

in NMP at 60°C. Once top down fabrication was complete devices consisted of a stack of $Si/SiO_2/Cr/Pt$-electrodes/SU-8/Cu-posts fig. 5.2 and were stored in inert atmosphere until the the fabrication of a silver nanoarchitecture [17, 74].

Each atomic switch network structure is unique and determined though the bottom-up fabrication of metal cations. In this case, silver nanowires form through an electroless deposition reaction involving the reduction of silver and the oxidation of copper. When the silicon device described above was placed in a solution of 50mM of silver nitrate ($AgNO_3$), the ordered copper posts (5x5 $\mu$m) direct a density controlled formation silver nanowires. This self organized growth occurs along the [111] axis of silver. This crystal assembly occurs according to the following reaction:

$$Cu^0_{(s)} + 2Ag^+_{(aq)} \longrightarrow 2Ag^0_{(s)} + Cu^{2+}_{(aq)} = 1.26 \text{ V}$$

#### 5.2.0.1 Characterization

**UV-Vis** The visible absorbance spectra of the thin films were measured on an HP 8453 spectrophotometer to identify the characteristic absorbance peak of AgI after functionalization.

**XPS** Five samples (Ag on glass control; 2 AgI (heated) on glass and 2 AgI (ambient) on glass) were secured to a sample load bar via carbon tape. In order to reduce charging effects, corners of the carbon tape were folded to make contact with the silver layer of each sample. This study used an AXIS Ultra DLD XPS instrument from Kratos Analytical, operated and maintained by the Molecular Instrumentation Center at the Department of Chemistry and Biochemistry at

UCLA. The X-ray source is Al K-alpha at 15kV. Survey and high-resolution scans were taken with pass filters of 160 and 20, averaged out over 4 and 16 sweeps, respectively. In order to reduce charging effects due to instrumentation issues, corners of the carbon tape were folded to make contact with the silver layer of each sample. All XPS spectra were then converted to a file type readable by the CasaXPS analytical software.

#### 5.2.0.2 Device Functionalization

ASNs function via metal-insulator-metal junctions, the skeletal architecture of which is supplied by metal nanowires. In order to functionalize the devices, an insulating material must be added. In the case of AgI ASNs, two insulating methods were explored. The first relied on ambient temperature; the device was placed in a sealed 100 mL container at room temperature with an iodine pellet and stored in a dark room for 24 hours. The second method consisted of a heated (30°C) nitrogen atmosphere, while the device was suspended over a solid iodine pellet for five minutes. Transparent thin films were iodized using the same two methods outlined above for the ASN devices; ambient and heated.

### 5.2.1 Reservoir Computing

*Reservoir Computing* (RC) is a means of computing complex functions without significant pre-training, using some dynamical system as a reservoir [25, 74]. By passing a time-varying input through a dynamic reservoir that implements non-linearities, different points on the reservoir are measured and linearly combined to reproduce an arbitrary output signal. RC leverages material complexity towards computational purposes; atomic switch networks are a natural candidate for this as

$Ag_2S$ networks have demonstrated the requisite complexity in the past [70, 71]. In this work, we used AgI networks as such a reservoir, and evaluated its potential for RC in two contexts: logic operations and spoken digit recognition.

#### 5.2.1.1 Logic Operations, Non-Temporal

Similar to our prior work with $Ag_2S$ devices [70], the device was exposed to several temporal bit streams at once. Both temporal (time and memory dependent) and non-temporal tasks were evaluated on the output. For these digital logic experiments two electrodes carried input signals of $+V_{logic}$ or $-V_{logic}$, representing a logical 1 and 0, respectively. One electrode was set as ground (0 V) and used to collect current. The remaining 13 electrodes were used to read voltage activity from different points on the device; a linear combination of these readings was used to derive all task performance metrics. A purely metal network set up in this manner would only be capable of performing linear computations on the active inputs. Meaning, any non-temporal linear computation would be possible in a metal network, but temporal and non-linear computations would not be possible.

To demonstrate the value added by using the reservoir, results are presented with three different readout modes. These readout modes indicate the pattern of electrodes used for linearly regressing coefficients to predict a target function. Note that all readouts were split into training and testing partitions. Regression was performed on the training partition, and reported accuracy results were from the testing partition. "I" indicates that only the voltages of the reservoir inputs were used to regress readout coefficients. "I" mode is therefore equivalent to no reservoir at all, while accounting for the same electrical noise seen in the other readout modes. "N" indicates that the readout electrodes were used - that is, the

traditional reservoir output. "R" indicates full-reservoir readout mode, where both readout and input electrodes were used for the regression. "R" is important for memristive devices as the network demonstrates predominately resistive behavior, and therefore the output voltage is strongly correlated to the input voltage [79]. Providing the input readouts therefore allows the regression to more accurately excise this correlation.

Following prior results on an $Ag_2S$ network [70], it was decided that the linear readout coefficients in this work would be calculated only one time per scenario. A sufficient number of training examples was found to stabilize the reservoir's behavior, and evaluating testing data on only a single array of readout coefficients was found to be valid [70].

#### 5.2.1.2 Logic Operations, Temporal

Temporal tests were carried out by regressing the reservoir readouts at a time $t = \tau$ based on one input from $t = \tau$ and another at $t = 0$. That is, both inputs to each logic function were part of the same temporal stream, and were $\tau$ inputs apart. Readout modes "I" and "R" were used, though "I" only served as confirmation that using only the inputs would result in a naive guess, as the current input would never have correlation with a past input.

#### 5.2.1.3 Spoken Digit Recognition

A more-complicated task with strong temporal needs, we evaluated ASN performance on spoken digit recognition using digits from the *Free Spoken Digit Dataset* (FSDD) (https://github.com/Jakobovski/free-spoken-digit-dataset). Similar to prior reservoir efforts at recognizing spoken digits, such as Jalalvand [37], recogni-

tion was not performed on the raw audio data but rather on the *Mel-Frequency Cepstrum Coefficients* (MFCCs) of the data. Each 8 kHz wave-format sound file from the FSDD was zero-padded up to a 1 s recording and then converted into MFCCs using the "python_speech_features" Python package [1]. Default settings were used, resulting in an array of MFCCs where each 25 ms window of signal is parameterized by 13 MFCCs. Windows were offset by 10 ms, resulting in 1287 total coefficients. To reduce device thrashing, and because our system did not allow for 13 simultaneous inputs, we flattened the resulting MFCC array and fed them to the network one at a time, such that the entire temporal sequence of the lowest-frequency coefficent's value is passed first, then the next-lowest-frequency coefficient's values across all windows, and so on. The resulting 1287 Hz signal was sent to one electrode, another electrode was used as a ground, and the remaining 14 electrodes were measured. Both the input electrode and the 14 reading electrodes were recorded at 1 kHz. For RC, the resulting voltage streams were sampled at the end of sub-windows of computation, and the entire collection of sampled recordings was linearly regressed to indicate which digit was spoken (see fig. 5.3). Due to limited resources, we used 12 unique spoken digit recordings, characterized by two speakers, saying three digits, two unique times. For reference with the FSDD, the speakers were Jackson and Theo, the digits spoken were zero, one, or two, and we used the first two instances of each of those pairings. As a baseline, regressions were performed on only the input electrode's voltage reading ("I" mode) as well as on the full electrode suite of the input electrode and the 14 read electrodes ("R" mode).

[1] https://python-speech-features.readthedocs.io/

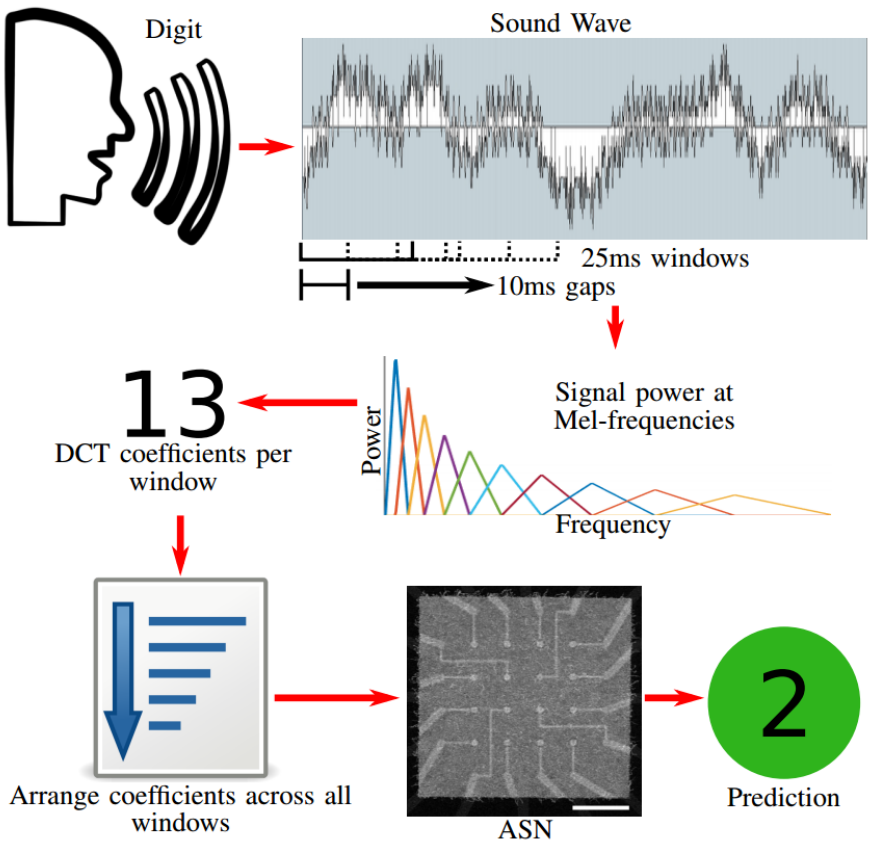


Figure 5.3: ASN input process used for spoken digits. Raw audio was broken into overlapping windows, each of which was converted to 13 MFCCs. These were arranged to minimize input thrashing for the ASN, and then passed as input to a single electrode. The final prediction was based on a linear combination of the remaining electrodes; see text for details.

## 5.3 Results and Discussion

### 5.3.1 ASN Characterization

fig. 5.4 shows the visible absorption spectra of transparent Ag and AgI thin films prepared by both methods. The transparent Ag thin films prepared by desktop sputtering exhibited surface plasmon resonance (SPR), suggesting the presence of silver islands within the thin films [10]. The results are in line with previous reports which have demonstrated that silver exposed to iodine decreases SPR intensity coupled with a buildup of excitons [10]. An absorbance peak around 420 nm has been previously reported relating to the dipole-forbidden $4d_{10} - 4d_9 5s$ transition in Ag which is enabled by the $Ag^+$ ion's tetrahedral symmetry within the AgI wurtzite structure yielding p-d hybridization. Method B's longer exposure to iodine yielded a red-shifted maximum, it has been postulated this may arise due to the formation of larger AgI particles [72].

Kinetic studies of AgI formation have demonstrated that the reaction exhibits a rate constant inversely proportional to temperature.It is postulated that this effect arises due to higher reaction temperatures favoring the growth of $\beta$-AgI basal planes parallel to the surface, creating a protective layer that hinders the diffusion of iodine through the thin film. Reactions occurring below 146° favor the formation of mixtures containing $\gamma$- and $\beta$-AgI; above this temperature, the more conductive $\alpha$-AgI crystals with mobile silver atoms are formed.

### 5.3.2 Logic Operations, Non-Temporal

For non-temporal logic operations, four functions were tested: IN0, IN1, AND, and XOR. These were tested to recall each individual input, to compute a linear

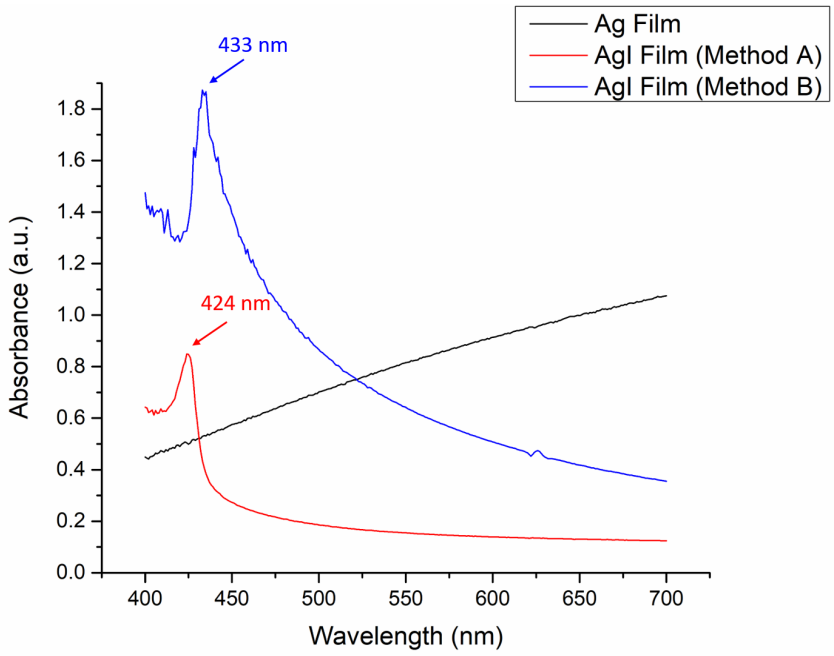


Figure 5.4: UV-Vis of silver thin films before and after iodization using ambient and heated methods.

combination of those inputs, and to compute a non-linear combination of those inputs. Four different electrode configurations were tested, with differing electrodes chosen for ground and input electrodes.

Mean and standard deviation of accuracy for linear functions (IN0, IN1, AND) across different frequency and voltage settings is shown in fig. 5.6. Statistics were computed across different electrode combinations and logic functions - 12 trials each. In general, recall was perfect - for "I" and "R" modes, this was unsurprising as the original inputs were available with only minor electrical noise added. For "N", the 10 Hz experiment exhibited a minor loss in accuracy, likely due to noise. If there were a connectivity issue in the network, it would have shown in the 5000 Hz trial in addition to the 10 Hz trial.

The non-linear function XOR was tested similarly, and its aggregate mean and

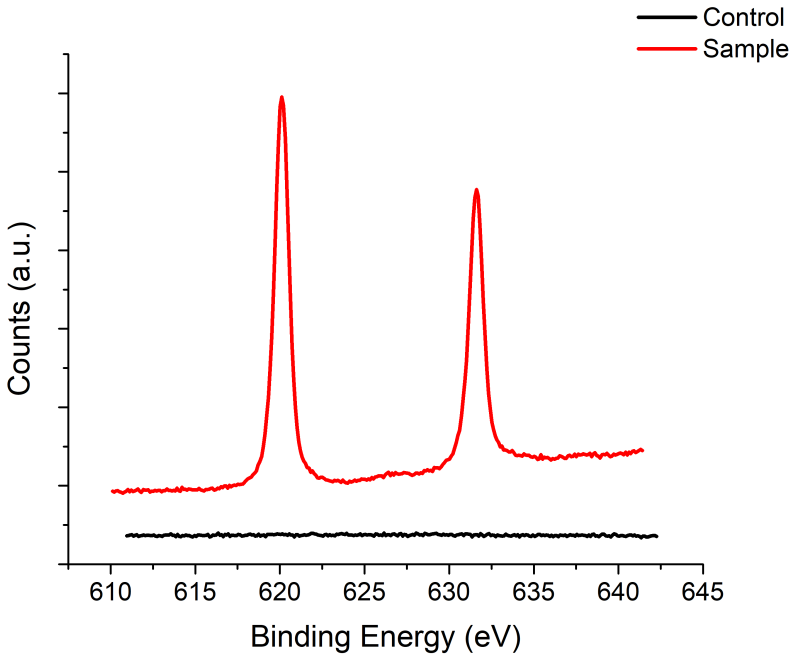


Figure 5.5: XPS spectra of silver-based devices exposed to (sample, red) or withheld from (control, black) iodization procedure. Characteristic peak for iodide 3d5/2 at a binding energy of 620 electron volts (eV) are absent in those devices withheld from iodization. In contrast, this peak is present in those devices exposed to iodization procedure and is consistent with previously reported spectra for metal iodides.

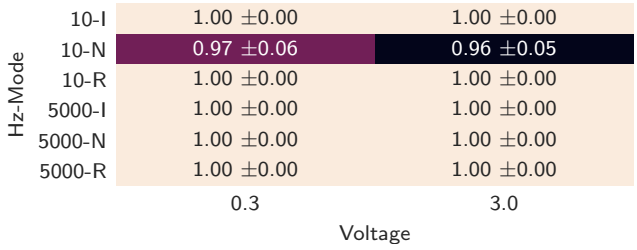


Figure 5.6: Mean ± standard deviation of accuracy for different input frequencies, input voltages, and regression modes, computed across different electrode combinations and the linear logic functions IN0, IN1, and AND. I - inputs only. N - read electrodes only. R - full reservoir readout.

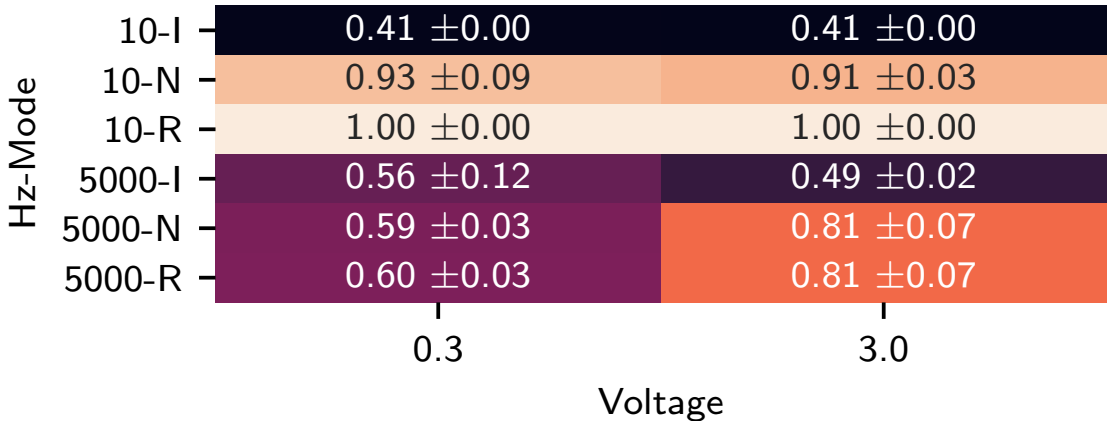


Figure 5.7: Identical layout as fig. 5.6, but showing statistics only for XOR to demonstrate non-linear results. Statistics are therefore computed across electrode combos, demonstrating the variability of choosing different input electrodes.

standard deviation is shown in fig. 5.7. Statistics are shown with respect to electrode combos - 4 trials each. This function is indicative of the ASN's abilities for reservoir computations, as it demonstrates functionality beyond that of the linear regression used for readouts. This may be seen by looking at the "I" mode of fig. 5.7: the linear readout was incapable of accurately regressing the non-linear function. However, both the "N" and "R" modes at 10 Hz were capable of outperforming a naive guess. The "R" mode demonstrated superior results as expected (section 5.2.1.1). We note that the 5000 Hz readouts are not quite as effective, likely because the switching time of this network was too large compared to the input exposure time. This is corroborated by 3 V performing better than 0.3 V: memristive switching times are known to decrease as voltage increases [94]. The 10 Hz results did not exhibit this problem, and netted 100 % accuracy on all logic functions across all electrode combinations.

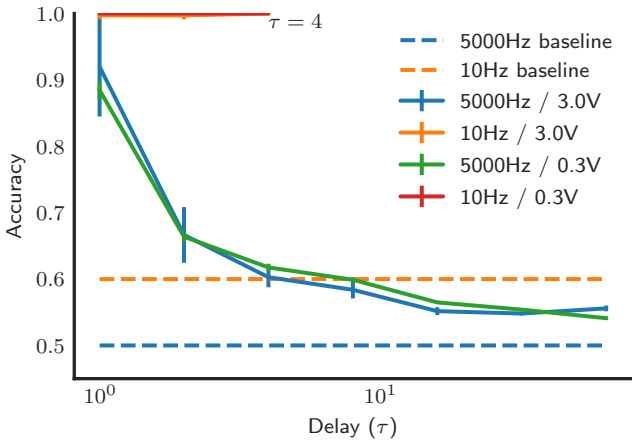


Figure 5.8: Recall of the input from $\tau$ bits in the past. While 10 Hz only had enough data to test up to $\tau = 4$ prior bits, it demonstrated perfect recall. 5000 Hz on the other hand demonstrated linearly-decaying recall, consistent with capacitive or inductive effects.

### 5.3.3 Logic Operations, Temporal

The temporal capacity of the reservoir was tested by applying the four different logic functions to bits in the input bitstream that were $\tau$ inputs apart. As non-temporal and linear functionality has already been demonstrated in section 5.3.2, we focus here on the ability of the ASN to recall an input from $\tau$ bits back, and the ability of the ASN to XOR the current input with that previous input.

"I" mode (inputs only) was tested with all temporal functions. As expected, performance was at the naive-guess baseline for all points. Thus these graphs were omitted.

Recall is shown in fig. 5.8. Due to a limited memory buffer, the 10 Hz experiments used an input sequence with a pattern length of only 5, making it impossible to measure $\tau > 4$. Nonetheless, the temporal fidelity of this ASN was very high. Prior inputs could be recalled with perfect accuracy, far above the naive guess baseline of 60 %. The 5000 Hz experiments were conducted with a much larger

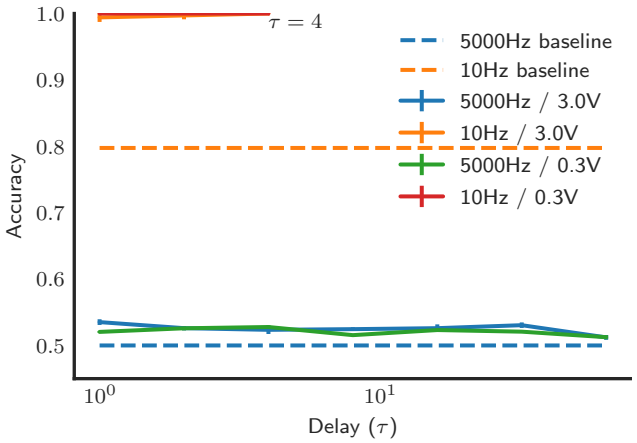


Figure 5.9: XOR between the current input and the input $\tau$ bits in the past. Like fig. 5.8, 10 Hz demonstrated perfect accuracy. Unlike recall, this illustrates that the prior results were stored in a non-linear manner, allowing for richer computations. 5000 Hz did not outperform the naive baseline, indicating slower input was required.

buffer, and so we show recall for $\tau \in 2^{\{0,\ldots,6\}}$. The roughly exponential fall-off observed indicates linear memory retention. Interestingly, the write voltage did not make a significant difference. It is possible that what is being observed is an inductive or capacitive effect rather than a less-volatile, long-term change in the device. Comparing with the non-temporal XOR results from fig. 5.7, where voltage made a significant difference, this may be further explained by pointing out that recalling a prior result is a linear operation. As such, we suggest that 5000 Hz is too quick for interesting temporal behavior to emerge. This is corroborated in fig. 5.9, described next.

The temporal computation of XOR is shown in fig. 5.9. The perfect accuracy of the 10 Hz experiments indicates that the temporal input sequence is preserved in a non-linear manner when exposed at 10 Hz. We note that while the naive baseline was 80 %, indicating that 4/5 of the input bit stream's XOR operations had the same result, the bit stream was exposed many times. That is, there were more than

5 experiments conducted, giving significance to the perfect accuracy. In contrast, the 5000 Hz experiments did not meaningfully surpass the naive guess baseline. Had the 5000 Hz exposed each input for a sufficient amount of time to produce non-volatile, non-linear behaviors, this would not have been the case.

### 5.3.4 Spoken Digit Recognition

As discussed in section 5.2.1.3, the FSDD digits were encoded as MFCCs and passed to the network as a temporal sequence at 1287 Hz. Results are shown in fig. 5.10. The "Input only" lines are consistent with readout mode "I", and the "Reservoir" lines are consistent with readout mode "R". The target function was regressed by dividing the measured electrode data into $N$ segments and using the last data point from each segment. For "Input only", this means that $N = 80$ used 80 values in the regression. For "Reservoir", this means that $N = 80$ used $80 \times 15 = 1200$ values in the regression. For the accuracy at each $N$, 12-fold cross-validation was used with 11 of the audio files as training data the 12th audio file as testing data. Each file was exposed to the device multiple times on a loop, aggregating far more than twelve tests to compute the accuracy. Nonetheless, there were only 12 unique data streams used. As a result, this problem suffered from significant overfitting, indicated by the "I" results decreasing in accuracy as more points were used for the regression. This overfitting manifested as significant noise in the accuracy; $N = 100$ might give an accuracy as high as 100 %, while $N = 101$ would give an accuracy of 54 %. To account for this, the space of points $N$ tested was divided into windows of size 25, and the average and standard deviation of accuracy within this window is shown in fig. 5.10. For instance, the mean and standard deviation shown at $N = 100$ indicate the statistics for $N \in \{88, ..., 112\}$.

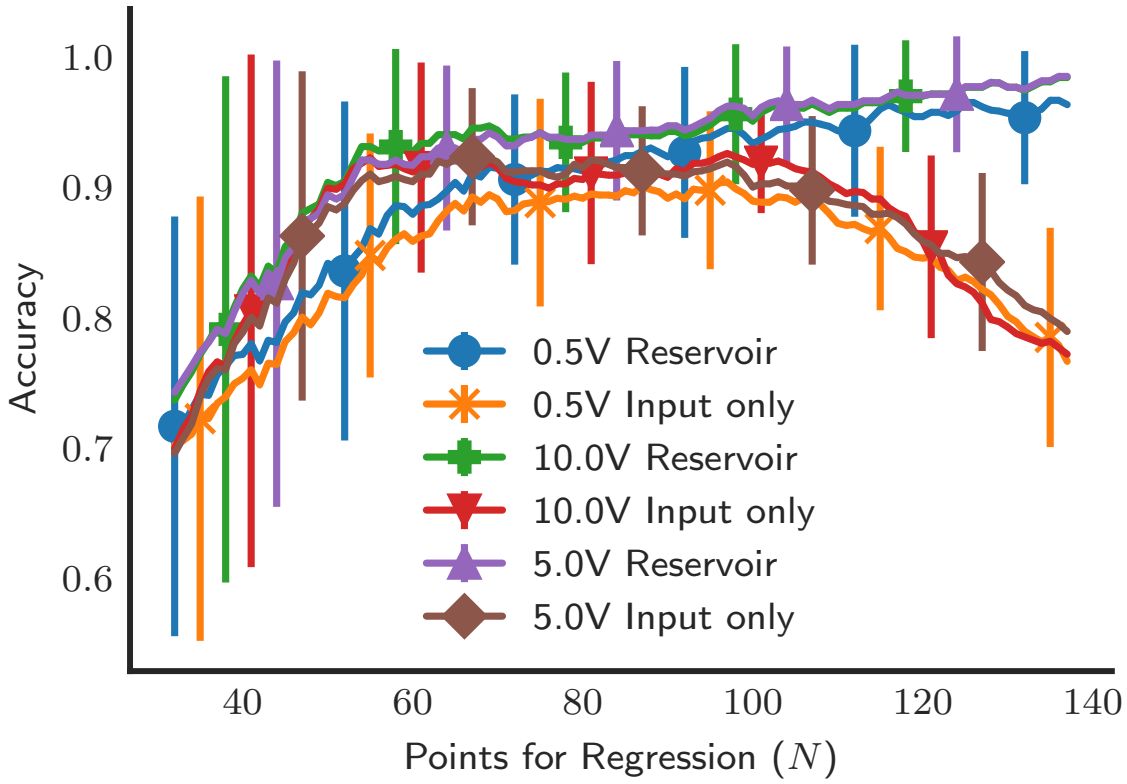


Figure 5.10: Mean and standard deviation for tapping the temporal sequence of spoken digit MFCCs at $N$ different points, and regressing to identify the digit spoken. This plot shows that the "R" readout method avoided overfitting and provided some benefit over using the inputs directly ("I" mode). See section 5.3.4 for precise formulation of this plot.

The main take-away of this experiment is that the reservoir lent stability to the regression, seen by a lack of downturn in the "R" lines, and provided a moderate benefit in accuracy, even before the input-only lines began overfitting. The lack of overfitting on the "R" lines could be interpreted as a side-effect of the temporal, non-linear properties of the reservoir. This is corroborated by the fact that the "R" lines achieved higher accuracy than the "I" lines, a phenomenon that could not be achieved without non-linear or temporal behavior. However, compared with section 5.3.3, it is unclear if the 1287 Hz input signal used for digit identification was slow enough to effect significant changes in the ASN. Another interpretation could be that the stability was added as a means of noise reduction via combining. Rather than relying on a stream of individual values, each of which has some noise associated, the "R" readout mode could rely on 15 such streams. Assuming the noise on each electrode is somewhat independent, averaging these channels could significantly reduce noise.

## 5.4 Conclusion

A new material for ASNs was verified via XPS and UV-Vis as AgI. Using lithographic techniques, an ordered multi-electrode array and patterned seed sites were fabricated. These served as the foundation for bottom up growth of silver nanowires which were successfully iodized to create a large number of MIM junctions in a densely packed and interconnected network. To evaluate the potential for computation, the network was given a series of voltage inputs to represent logic tasks. In addition to this, a series of spoken digits were converted from audio to varying voltage traces of different magnitudes and sent into the new AgI ASN. It

was demonstrated that the ASN has perfect, non-linear temporal recall of a 10 Hz binary signal. A 5 kHz signal was shown to change too rapidly to effect lasting change in the ASN. For spoken digits, it was shown that processing the audio signal with a AgI ASN improved accuracy and prevented overfitting. These experiments, coupled with the relative ease and inexpense of the AgI fabrication process, showed AgI to be a promising ASN material. As advancements in traditional computer architectures slow, we believe that in-memory computing fabrics, such as the ASNs demonstrated in this work, may provide inexpensive, efficient, and accurate computational elements that replace some traditional computing hardware.

# Chapter 6

# Two dimensional electrophysiological characterization of human pluripotent stem cell-derived cardiomyocyte system

Stem cell-derived cardiomyocytes provide a promising tool for human developmental biology, regenerative therapies, disease modeling, and drug discovery. As human pluripotent stem cell-derived cardiomyocytes remain functionally fetal-type, close monitoring of electrophysiological maturation is critical for their further application to biology and translation. However, to date, electrophysiological analyses of stem cell-derived cardiomyocytes has largely been limited by biologically undefined factors including 3D nature of embryoid body, sera from animals, and the feeder

cells isolated from mouse. Large variability in the aforementioned systems leads to uncontrollable and irreproducible results, making conclusive studies difficult. In this report, a chemically-defined differentiation regimen and a monolayer cell culture technique was combined with multielectrode arrays for accurate, real-time, and flexible measurement of electrophysiological parameters in translation-ready human cardiomyocytes. Consistent with their natural counterpart, amplitude and dV/dt max of field potential progressively increased during the course of maturation. Monolayer culture allowed for the identification of pacemaking cells using the multielectrode array platform and thereby the estimation of conduction velocity, which gradually increased during the differentiation of cardiomyocytes. Thus, the electrophysiological maturation of the human pluripotent stem cell-derived cardiomyocytes in our system recapitulates in vivo development. This system provides a versatile biological tool to analyze human heart development, disease mechanisms, and the efficacy/toxicity of chemicals.

## 6.1 Introduction

The potential of human pluripotent stem cells (hPSC) to self-renew indefinitely and differentiate into virtually any cell type makes them a valuable cell source for human developmental biology, cell-based regenerative therapy, disease modeling, and drug discovery/assessment.[15, 32, 33, 80, 81, 86, 98] As the human heart is the least regenerative of tissues, cardiomyocytes derived from human embryonic stem cell/induced pluripotent stem cells (hESC/iPSC-CMs) provide a particularly powerful biological tool.[2, 41, 47, 60, 61, 93] Differentiation protocols have evolved over the years to allow for large-scale induction of human cardiomyocytes, and efforts

have been made to induce further maturation of ESC/iPSC-CMs in vitro, with tissue engineering approaches showing promising results.[54, 65, 89, 99] However, the maturity of in vitro hESC/iPSC-CMs still remains fetal-type with limited electromechanical properties. Unlike postnatal cardiomyocytes, hESC/iPSC-CMs are proliferative [12, 58, 76, 89], but with immature sarcomere structure [12, 58, 76] and $Ca^{2+}$ handling properties.[19, 39, 40, 42, 89] Sarcolemmal-dependency of calcium kinetics, negative force-frequency relation [42] and high maximum diastolic potential demonstrate the functional immaturity of hESC/iPSC-CMs. Indeed, contractile forces generated by hESC/iPSC-CMs are estimated to be less than 0.5–5% of cardiomyocytes isolated from the neonatal heart.[22, 55] Application of external biophysical cues including mechanical force [89], electrical stimulation [65], and matrix stiffness [2, 31] are promising approaches to induce the maturation of hESC/iPSC-CMs. However, these approaches have yet to achieve sufficient functionality to replace the damaged cardiomyocytes in the diseased heart.

Following the induction of the cardiac gene program during early embryogenesis, cardiomyocytes undergo a remarkable maturation process to develop into structurally and functionally competent cardiomyocytes during fetal stages, characterized by the assembly of contractile proteins into myofibrillar structure, expression of ion channels and gap junctions at the right location, organization of mitochondria and SR along the myofibrils, etc. The study of late-stage cardiogenesis is translationally relevant, as most of the events leading to congenital heart anomalies occur at later stages, and cell therapy requires functional cardiomyocytes with strong contractile force. Although great progress has been made in studies of specification and multilineage differentiation of cardiac progenitors, our understanding of the cardiac maturation process remains primitive.[62] While the differentiation level of

early cardiac progenitors is well defined by marker gene expression, the maturity of cardiomyocytes at late developmental stages is relatively less reflected in the gene expression pattern.[14, 50, 56, 96] Given that the biophysical cues are not only the results but also the essential drivers of the cardiac maturation [2, 21, 23, 31, 68], the electrophysiological properties of hESC/iPSC-CMs are critical parameters to monitor.

Microelectrode arrays (MEAs) provide a highly sensitive, non-invasive method to study the electrophysiology of cardiomyocytes with spatiotemporal resolution. However, to date, the application of MEA to human cardiomyocytes has largely been limited by biologically undefined factors including 3D nature of embryoid body, sera from animals, and feeder cells isolated from mouse.[32] In this paper, using two-dimensional monolayer cultures of hESC-CMs with media free of animal products, we present a hybrid method for real-time measurement of electrophysiological dynamics of human cardiogenesis that is compatible with existing MEA technologies. Combination of hESC/iPSC-CM monolayer culture and the MEA system enables accurate, real-time, and flexible measurement of electrophysiological characteristics, thereby providing a versatile biological tool to analyze human heart development, understand disease mechanism, and assess the efficacy and toxicity of drugs.

## 6.2 Results

**Molecular and cellular characterization of hESC-CMs**. H9 and UCLA4 hESCs were grown and differentiated as previously described [60] and plated as a monolayer. To define the differentiation stages, marker gene expression was serially profiled (fig. 6.1a). mRNA quantification suggests that mesodermal markers

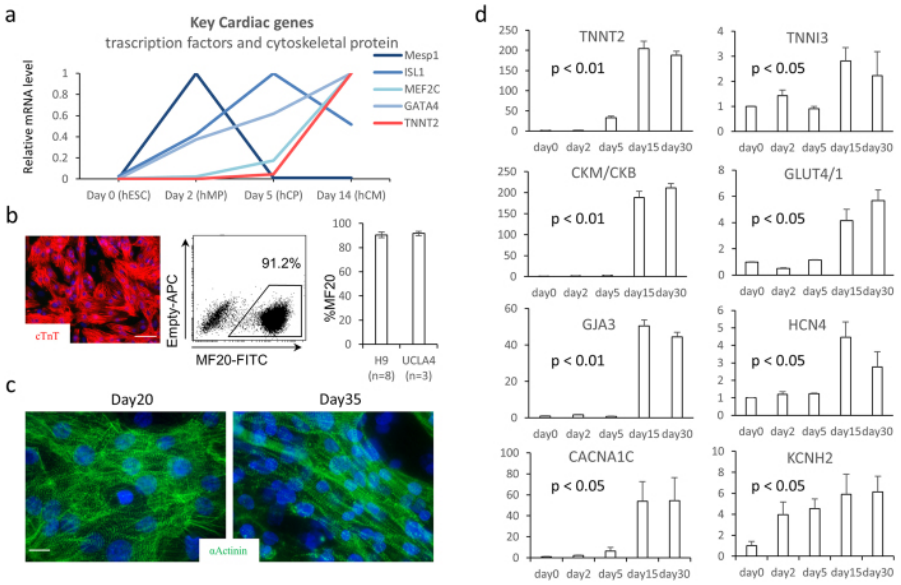


Figure 6.1: (a) mRNA relative expression over the time course of hESC differentiation toward cardiac lineages. The value is standardized to the peak value of the time points for each gene. (b) Immunofluorescent staining for $\alpha$-actinin in red showing over 90% are positive for $\alpha$-actinin (scale bar = 100 um) (c) Morphological changes in hESC-CMs over the time course. Representative optical images of hESC-CMs on MEA on Day 20 and Day 35 (fluorescent staining: $\alpha$-Actinin in green, nucleus in blue, scale bar = 10 um). (d) mRNA relative expression by qPCR standardized to the expression of day0 over the time course of cardiac differentiation/maturation.

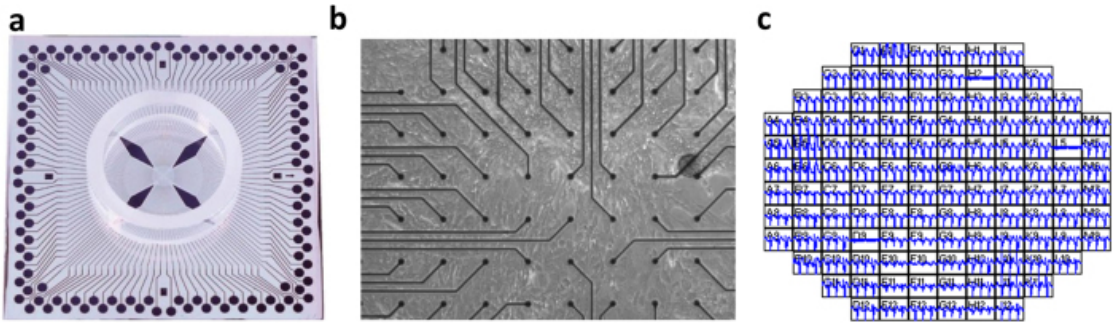


Figure 6.2: (a) Microelectrode arrays (MEA) with 120 integrated TiN electrodes (30 $\mu$m diameter, 200 $\mu$m interelectrode spacing) were used to culture the 2D hESC-CMs. (b) Representative optical image of hESC-CMs on top of MEA. (c) Field potential signals were detected in electrodes which are in touch with the hESC-CMs.

(Mesp1, Bry) were highest at day 2 (mesodermal precursor stage; MP stage). Cardiac progenitor marker, ISL1, reached its peak at day 5 (cardiac progenitor stage; CP stage). Spontaneous contraction starts at around day 7. By day 14, major cardiac structural proteins, ion channels, and gap junctions became strongly expressed (immature cardiomyocyte stage; CM stage). At this stage, 90% of the cells were MF20 + cardiomyocytes with typical sarcomeric structures (fig. 6.1b). hESC-CMs underwent further maturation after day 14 and became elongated and oriented perpendicular to the lateral registration of sarcomeres by day 30 (fig. 6.1c). $\alpha$-actinin staining suggests that the Z-band becomes more aligned at later stages (fig. 6.1c).

To examine the maturation level of late-stage hESC-CMs, the expression of marker genes at day 14 and day 28 were examined. Cardiac maturation indices, such as the subtype ratio of enzymes (CK-M/B) and metabolic indicators (GLUT4/1), progressively increased (fig. 6.1d). However, the expression level of most contractile proteins (TNNT2, TNNI3), gap junction genes (GJA 3), or ion channel genes (HCN4) were not significantly upregulated in mRNA at day 28 compared to day 14 (fig. 6.1d). Therefore, the mRNA expression profile was highly distinctive at early differentiation stages (days 2–14) but became less definitive at late maturation stages (days 14–28).

**Validation of MEA culture**. Taking advantage of the monolayer differentiation regimen, hESC-CMs were cultured on an MEA platform that enables real-time (up to 40,000 samples/sec), simultaneous acquisition of 120-channels of spatially distributed electrical data from individual microelectrodes embedded in a cell culture device (fig. 6.2a-c). Inadequate contact between cultured cells and the measurement electrodes resulted in signal amplitudes less than a pre-defined signal-to-noise ratio

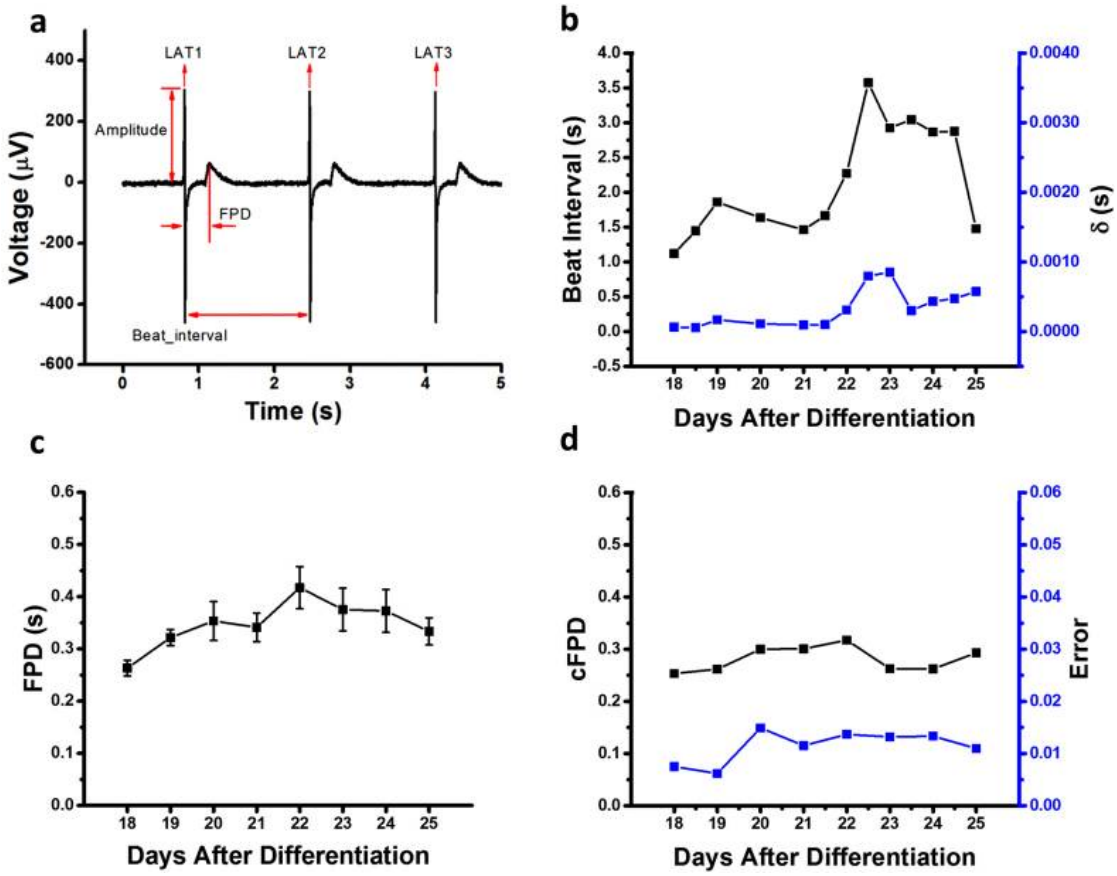


Figure 6.3: (a) Field potential features such as beat interval, field potential duration, amplitude, and local activation time (LAT) were extracted out of the signal sequences. On average, 100 out of 120 channels were selected to calculate the beat interval after the peak detection and experiments were performed in triplicate. (b) The beat interval was stable up to day 28–30 with a beat interval around 2 s. Starting from day 28, the beat interval of hESC-CMs became unstable and irregular. The standard deviation ($\delta$) of beat interval agreed with the beat interval trend. (c) The field potential duration (FPD) ranged from 0.2 s to 0.5 s and was relatively stable throughout the differentiation process. (d) The corrected FPD ( = FPD/[beat interval/1000] 1/3 ; Fridericia's formula) was also relatively stable ranging from 0.2 to 0.3.

(4), making them indistinguishable from the background noise of the measurement system. Electrode channels in firm contact with the underlying cell monolayer acquired clearly distinguishable local field potential signals (fig. 6.3a) that enabled examination of hESC-CMs maturation at the electrophysiological level by monitoring their steady and consistent beat signatures over 10 days when cultured on an MEA plate. Regular beat intervals ranging from 2–4 s with standard deviations below 0.0014 s (fig. 6.3b) and field potential durations (FPDs) of approximately 0.3–0.4 s were observed throughout the differentiation (fig. 6.3c). Corrected FPD was also relatively stable (fig. 6.3d).

Monitoring the field potential of hESC/iPSC-CMs following chemical compound administration has been reported and expected as a novel drug screening tool for cardiotoxicity. To validate the assay system, response to pharmacological interventions were examined by administration of canonical ion channel blockers E4031, TTX (tetrodotoxin), and Nifedipine (fig. 6.4). Consistent with previous reports [33], E4031, a $K\hat{+}$ channel blocker, reduced the field potential amplitude and the beat interval in a concentration-dependent manner but had no impact on FPD (fig. 6.4a,d,g). TTX, a selective Na + channel blocker, induced an increase in the beat interval even at a remarkably low concentration with a concurrent trend of reduction in the amplitude and FPD (fig. 6.4b,e,h). Nifedipine, a $Ca\hat{2}+$ channel blocker with negative inotropic and chronotropic effects, showed a mild trend of reduction in the peak amplitude of field potential, a significant increase in the beat interval, and decrease in FPD (fig. 6.4c,f,i), consistent with well-known clinical observations. Previous reports using hESCs showed a decrease in beat interval with Nifedipine.[27] These inconsistencies may be attributed to the specific details of differentiation regimens, relative condition of the cells, or inter-cell line

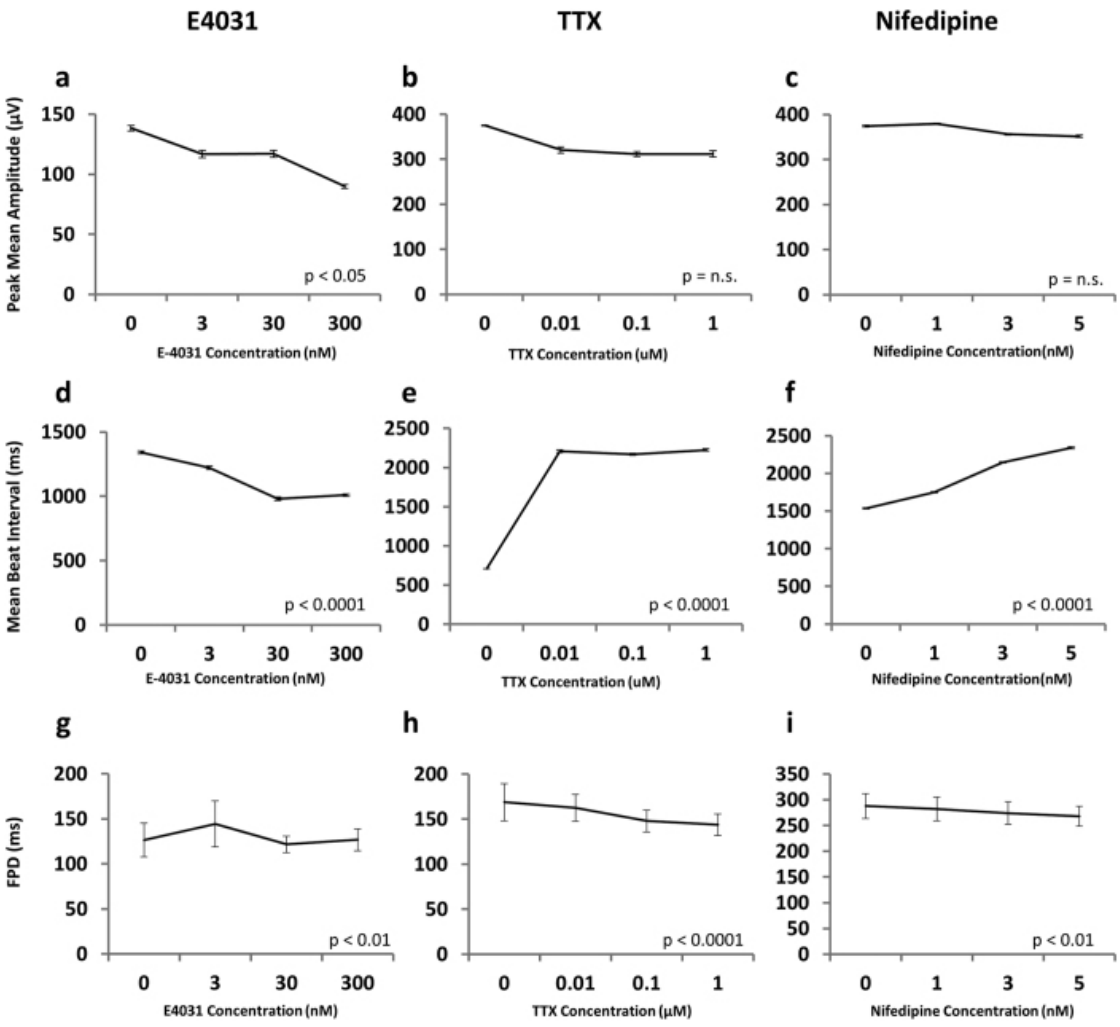


Figure 6.4: Peak mean amplitude (a–c) and mean beat interval (d–f) of field potential of monolayer cardiomyocytes cultured in the presence of (a,d) E4031 ($K^+$ channel blocker), (b,e) TTX (tetrodotoxin, $Na\hat{+}$ channel blocker) and (c,f) Nifedipine ($Ca\hat{2}+$ channel blocker). p-values are calculated by one-way ANOVA. Data are representative of at least 2 biological replicates.

difference. The observed reduction in peak amplitude in response to E4031 was deemed statistically significant based on a p value of less than 0.05 in an analysis of variance (ANOVA). Trends observed for the reduction in peak amplitudes for TTX and Nifedipine were found to be statistically insignificant. Trends, both increases and decreases, in observed beat intervals for all three ion channel blockers were also statistically significant according to their representative p-values. These results suggest that our system facilitates an accurate and real-time measurement of the electrophysiological activity of hESC-CMs.[27, 33]

**Identification of pacemaking cells in the monolayer cardiac sheet**. The combination of a confluent layer of hESC-CM and the large microelectrode array allowed for not only temporal, but also for spatial analysis of the electrical activity. The field potential propagation was characterized using the phase difference of each channel covered by the confluent layer of hESC-CM. fig. 6.5 shows representative field potential propagation waves at varying cell age from day 18 to 25. The propagating wave generates circular wave fronts. Analysis over a 20-minute recording window showed a consistent propagation map, indicating that the pacemaking source was stable (fig. 6.5a–d). However, the propagation map changed over days, indicating that the pacemaking source was not completely fixed over a long period (fig. 6.5e–h,i).

The electrical activity of hESC-CMs was initialized by a small group of pacemaking cells and propagated to the surrounding cardiomyocytes via gap junctions. Assuming that the propagation waves originated from a point source, the contour of the activation map was approximated by a circle. Although the position of pacemaking cells may fall outside of the electrode array in the MEA platform (see fig. 6.2), the location of pacemaking cells can be predicted using the radius of the

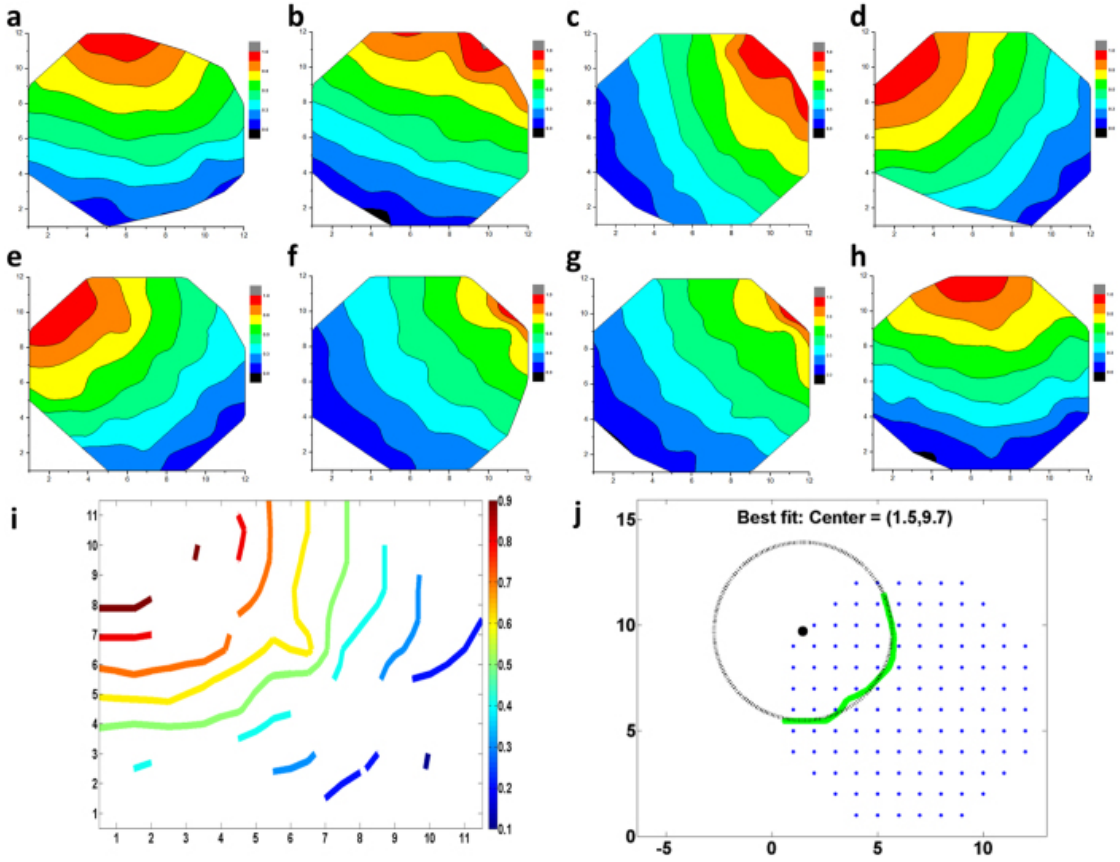


Figure 6.5: Field potential propagation, pacemaking and conduction velocity of the 2D hESC-CMs. (a–h) shows a representative activation map from day 19, 20, 21, 22, 25, 26, 28, 29, respectively. The activation map was consistent over the 20-minute recording window showing a stable pace making source, but the propagation map changed over days. (i) On day 23, a contour graph of the propagation wave was generated from the activation map. (j) The center of the propagation wavelet was identified by fitting the wavelet with a circle. The origin of the circle represented the location of the pacemaking cells. The pacemaking cells were located at the edge of the MEA.

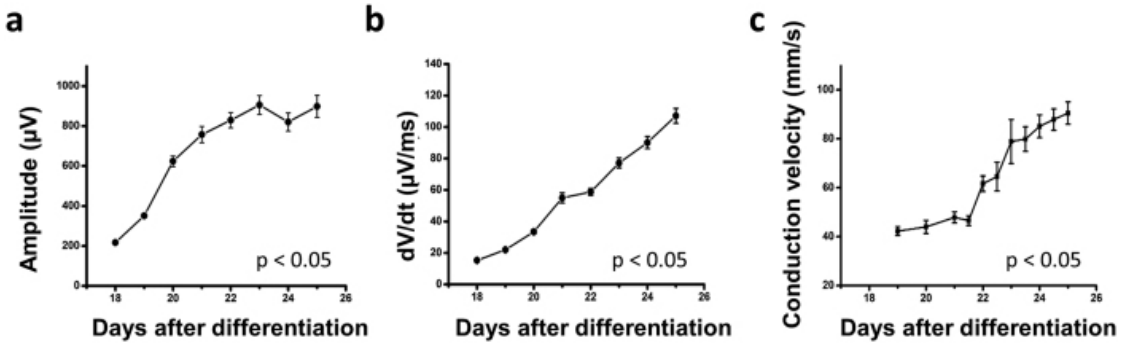


Figure 6.6: (a) The field potential amplitude rapidly increased until day 23 and declined at day 27. The turning point agreed with that of the beat interval. (b) The field potential amplitude upstroke speed increased from 15.3 $\mu$V/ms at day 18 to 122.9 $\mu$V/ms at day 26 and declined at day 27. (c) Conduction velocity was calculated at each day. There was an increment of conduction velocity as the development of hESC-CMs. Results from two samples were consistent.

curvature of the field potential. For example, the coordinates of the pacemaking cells shown in fig. 6.5j were (1.5, 9.7), at the edge of the MEA electrodes.

**Characterization of cardiac maturity and conduction velocity**. The capacity to monitor spatiotemporally resolved local field potentials in real-time provides a readout for maturation of hESC-CMs during differentiation. Consistent with a previous study [56], the mean field potential amplitude increased rapidly (4–5 fold) up to day 26 (fig. 6.6a). Furthermore, the maximal field potential upstroke (dV/dt max), indicative of the sodium channel activity, became progressively larger as the hESC-CMs maturate (fig. 6.6b). During natural embryogenesis, cardiac conduction velocity increases as the heart maturates, with neonatal and adult cardiomyocytes showing  0.3 m/s and  1 m/s, respectively. To examine whether conduction velocity increases during the maturation of hESC-CMs in this system, the conduction speed was calculated by analyzing the signal traveling distance and time lag. Analysis performed in both vertical and diagonal directions with respect to the pseudo pacemaking region (fig. 6.6c) reveal a conduction speed at

day 18 of approximately 35 mm/s. As the hESC-CMs maturated over subsequent days, conduction velocities increased up to a maximum of 120mm/s at day 28, a value indicative of functional immaturity relative to neonatal cardiomyocytes. Field potential amplitude, upstroke and conduction velocity were determined to be statistically significant based on p-values ¡ 0.05 determined via ANOVA. In contrast to commonly utilized molecular signatures, electrophysiological parameters showed a clear progression of cardiac maturity during the differentiation stages between days 14 to 26. Thus, the combination of the monolayer culture platform and MEA facilitates comprehensive monitoring of the electrophysiological maturation process of hESC-CMs.

## 6.3 Discussion

The integration of a chemically-defined differentiation regimen with a monolayer culture of human pluripotent stem cell-derived cardiomyocytes and electrophysiological measurement on an MEA platform provides a direct method to examine the spatiotemporal dynamics of the electromechanical maturation in human cardiomyocytes. Stem cell derived cardiomyocytes provide a powerful tool for human developmental biology, regenerative therapies, disease modeling, and drug discovery. However, the utility of MEA for the hESC/iPSC-CMs has been largely limited to disease modeling and drug assessment.[3, 11, 15, 20, 28, 46, 63, 67, 90] The monolayer culture method described here overcomes technical problems associated with the utilization of conventional 3D embryoid bodies, namely large inter-experiment variability due to inconsistency in their size, quality, and attachment to MEA surface. In addition, the use of animal sera and feeder cells often introduce additional

variables to differentiation efficiency and functionality. Our chemically-defined regimen serves to further minimize experiment-to-experiment variability.[60] In combination, our system enables the monitoring of electric signals over weeks from cells in direct contact with electrodes, identification of pacemaking cells, and performance of computational analyses of localized voltage-type signal and position-dependent properties of electrical activity.

Utilization of this system has enabled a direct characterization of electrophysiological maturation in hESC-CMs. During the natural embryonic cardiogenesis, action potential amplitude, action potential upstroke, conduction velocity, and heart rate gradually increase as the fetal cardiomyocytes maturate. In vitro differentiation of pluripotent stem cells recapitulates the natural developmental process. Our data suggest that hESC-CM differentiation shows the same trend of electrophysiological properties including field potential amplitude, dV/dt max, and conduction velocity. Even though our differentiation protocol is 'directed' toward the cardiac lineage, the differentiation of hESC-CMs follows the same developmental process at genetic and electrophysiological levels. Of note, the electrophysiological parameters show a progressive increase in the field potential amplitude, dV/dt, and conduction velocity (fig. 6.6), while typical cardiac markers including TNNT2 and TNN13 do not show significant differences after day 14 (fig. 6.1). Therefore, electrophysiological parameters appear to be more sensitive indicators for the assessment of cardiomyocyte maturity than genetic parameters. Although our monolayer hESC-CMs display robust beating, the electrophysiological parameters indicate that monolayer hESC-CMs are less differentiated than cardiomyocytes generated via 3D embryoid bodies. For example, previous reports show dV/dt max of 2 V/second or higher.[44, 57] The relative immaturity of hESC-CMs may be in part because the monolayer condition

is less physiological than the 3D environment. Possibly due to the immaturity or to the spatial resolution of electrode array, the wave fronts were not reorganized from circular to oval pattern as hESC-CMs differentiate. These limitations should be considered when applying the monolayer hESC-CM MEA system to analyses of human developmental biology, patient-specific disease mechanisms and drug discovery/assessment.

Looking ahead, the availability of high-throughput measurement platforms has proven to be highly advantageous in basic and translational research. High-throughput optical readouts using voltage dyes, calcium dyes, or their combinations have demonstrated the utility of hESC/iPSC-CMs as a model system for such methods.[7, 33] While our current system configuration cannot be directly utilized in high-throughput analysis, there is no fundamental barrier that precludes the development of such capabilities. In fact, monolayer culture facilitates the basic molecular and cell biology techniques including lipofection, viral infection, and microscopic observation in combination with the electrophysiological analyses described here. Further, when considering the reproducibility and the versatility of the MEA platform coupled with 90% cardiac efficiency in our monolayer culture, the development of high-throughput electrophysiological readouts represents a promising research direction. The accurate, real-time, and flexible method demonstrated in this study sets a new standard for electrophysiological analyses of hESC/iPSC-CMs with broad applicability in stem cell biology.

## 6.4 Methods

**Microelectrode array measurements**. hESC-CMs were maintained and differentiated as previously described.[60] At 16 days of age hESC-CMs were plated on uncoated, microelectrode arrays (MEAs) containing 120 integrated TiN electrodes (30 $\mu$m diameter, 200 $\mu$m interelectrode spacing). The MEAs were placed in an incubator with a temperature of 37°C and 5% $CO_2$. Two days were given to ensure the cardiomyocytes were well attached to the MEA. Recording commenced at a cell age of 18 days. Local field potentials at each electrode were collected over a period of 20 minutes, twice a day, and 3 weeks in total with a sampling rate of 1 kHz using the MEA2100-HS120 system (Multichannel systems, Reutlingen, Germany). The chemical compounds used herein were purchased from Tocris (E4031), Fisher Scientific (TTX) and Sigma-Aldrich (Nifedipine).

**Peak detection**. Determining the amplitude, frequency, and conduction velocity of cardiomyocyte activity required reliable assignment of peaks in the local field potential signal for all 120 channels. The Matlab function 'findpeaks' was used with tunable parameters 'minpeakheight' and 'minpeakdistance' to reliably determine signal peaks. Setting the 'minpeakheight' as 16 $\mu$V defined a minimum signal-to-noise ratio of 4 considering the noise level in the MEA system was $\pm$ 8 $\mu$V. The 'minpeakdistance' was set as 1000 ms, which was based on the experimental observation that cardiomyocytes were beating at a frequency smaller than 1 Hz.

**Beat interval**. The beat interval was measured as the peak-to-peak time difference from the beat amplitude assignments for each channel. After implementing peak detection as described above, the beat interval and standard deviation were collected for all channels. Unsynchronized and/or significantly noisy electrodes excluded from analysis were those with standard deviations that fell outside of 10%

of the median standard deviation from all channels. The mean of the beat interval ± STD was calculated from all channels within this threshold. Analyses of the field potential propagation. Time differences in the rhythmic local field potential collected from 120 electrodes were quantified by dividing the complete data set for each day into a sequence of segments (typically 30 s, each). Peak detection was used to identify active channels. Cross correlation of the acquired signals from each active channel with respect to a pre-chosen reference electrode provided the time lag of each electrode with respect to the reference electrode. The time lags were then normalized between 1 and 0, representing the pace leader and last follower, respectively.

**Identification of pacemaking cells**. The pacemaking cells sometimes fall outside the region of the MEA electrode area. Assuming the whole cardiomyocyte culture had only one cluster of pacemaking cells and the pace-generating signal propagated like a wave, the position of the pacemaking cells can be extrapolated based on the partial propagation waveform that was detected in the MEA electrode area. Compared to the localized pacemaking cells, a contour plot of propagation time at each channel within the MEA electrode area was shown. Each archer-shape line had the same propagation time. A circle was fitted to the archer-shape line and the origin of the circle represented the location of the pacemaking cells. A Matlab circle fit module developed by Izhak Bucher was adopted in the above process.

**Conduction speed analysis**. Conduction speed was defined as the velocity of the field potential propagation across the MEA surface. The time for each electrical beat was found through the peak detection analysis described previously. The time lag and distance of each channel with respect to the pacemaking cells (earliest beat identified from the 120 channels) was calculated. The conduction speed at

each channel was therefore calculated. Conduction speed in both the vertical and diagonal direction was shown in fig. 6.6c. To calculate the average conduction speed for each recording period, the conduction speed was averaged in both 120 channels and the 20-minute recording period. Results from a cell age of 18 days to 25 days were shown in fig. 6.6.

# Chapter 7

# Conclusions

Neuromorphic atomic switch networks have been fabricated in 16 and 128 electrode configurations. These devices consist of highly ordered top-down methods combined with density directed bottom-up methods, the combination of which falls into the realm of nanoarchitectonic design. Resulting silver networks consist of long and short-range nanowire to microwire connections with up to $10^8/\text{cm}^2$ junctions that once insulated hold the potential for atomic switch formation. Insulating materials used were either sulfur or iodine, differences of which are touched up in 5. These chips present an alternative hardware solution that circumvents not only the packing density limitations of Moore's Law, but also the information transfer lag-time known as the Von Neumann Bottleneck.

As such, atomic switch networks have been evaluated within the context of computing. Specifically, they have been described with respect to unconventional, alternative, or natural computing. These areas of computing emphasize computing inspired by nature, simulation of nature by computing, and computing with natural materials. Brain inspired neural networks fall into these categories, as does the

physical implementation of a microchip structured similarly to the mammalian brain. The ASNs described herein have been most suited for use as a reservoir in a recurrent neural network, for reservoir computing. Reservoir computing is inherently temporal in nature and has many benefits such as fault-tolerance, non-linearity, and learning all without the need for pre-training within the network.[92] Classically reservoir computing was implemented in a basin of water, and has since gained popularity in photonics. Research towards ASN RC efforts included evaluation of network dynamics, non-linear transformations, power spectral densities, and benchmark tasks. One benchmark was to evaluate the network in linear and non-linear logic tasks. As expected, low voltages that perturb the reservoir network less are better at linear logic (AND, OR) while higher voltages excited the network much more and performed better at non-linear XOR task. It should be noted that the future of reservoir computing lies within solving complex problems, not recreating standard computers which excel at linear logic.

With the growing complexity of our world comes an increase in complex adaptive systems (CAS). Being able to model the evolution of patterns and cascading effects of non-linear dynamical systems holds potential anywhere complex behavior emerges. Examples of which include the internet, economics, ecosystems, and genetics, just to name a few. A case for Atomic Switch Networks (ASNs) as a complex adaptive system was made, calling attention to power law slopes and evidence for edge of criticality operations. Spatially distributed non-linear responses were shown in $V_in$ vs. $Vout$ plots to illustrate the dynamics of ASNs 4. These properties include a large repertoire of outputs signals which can be described by phase shifts, and non-linear transformations of the input signal. The ASN was pushed to produce persistent critical dynamics between two states via a current controlled feedback

loop, in not only current, but also in voltage. Control over a critical network holds potential for the modeling of a wide array of CAS systems.

Atomic switch networks function as complex systems which transform data into higher dimensional space. Differences in switching speeds and memory retention for materials provide the potential for further studies. Once a larger data base for temporal and spatial behavior exists, the commercialization of such systems as chips for nonlinear, stochastic prediction, or pattern classification problem solving is inevitable. At this point, the slower switching speeds of AgI lend a higher accuracy for the use of linear regression algorithms consisting of a training and testing period. The classically studied $Ag_2S$ not only takes longer to insulate and thus functionalize, but also has less reliable switching behavior. That is not to say that there will be no feasible application of such a speedy, stochastically switching system. Again, I must stress the importance of archiving the properties of different materials for these purposes, of which the work herein explored only two. Additionally, multiple networks in varying configurations ought to be studied as modeling and theory suggests these would excel at complex problem solving. The brain is a 3D network which has compartmentalized areas that are still highly interconnected allowing for quick information transfer and temporal processing. In order to reach the next level of complexity a well thought out combination of neuromorphic chips, CMOS, and software holds incredible potential for the future of computing.

# Bibliography

[1] H. A. H. Al-Khazali and M. R. Askari. Geometrical and graphical representations analysis of Lissajous figures in rotor dynamic system. *IOSR Journal of Engineering*, 2(5):971–978, 2012.

[2] A. Arshi, Y. Nakashima, H. Nakano, S. Eaimkhong, D. Evseenko, J. Reed, A. Z. Stieg, J. K. Gimzewski, and A. Nakano. Rigid microenvironments promote cardiac differentiation of mouse and human embryonic stem cells. *Sci Technol Adv Mater*, 14(2):025003, Apr 2013.

[3] Y. Asai, M. Tada, T. G. O. Nakatsuji, and Norio. Combination of functional cardiomyocytes derived from human stem cells and a highly-efficient microelectrode array system: An ideal hybrid model assay for drug development. *Current Stem Cell Research & Therapy*, 5(3):227–232, 2010.

[4] A. V. Avizienis, C. Martin-Olmos, H. O. Sillin, M. Aono, J. K. Gimzewski, and A. Z. Stieg. Morphological Transitions from Dendrites to Nanowires in the Electroless Deposition of Silver. *Crystal Growth & Design*, 13(2):465–469, feb 2013.

[5] A. V. Avizienis, H. O. Sillin, C. Martin-Olmos, H. H. Shieh, M. Aono, A. Z.

Stieg, and J. K. Gimzewski. Neuromorphic atomic switch networks. *PloS one*, 7(8):1–8, jan 2012.

[6] P. Bak, C. Tang, and K. Wiesenfeld. Self-organized criticality: An explanation of the 1/ f noise. *Physical Review Letters*, 59(4):381–384, jul 1987.

[7] S. Bedut, C. Seminatore-Nole, V. Lamamy, S. Caignard, J. A. Boutin, O. Nosjean, J.-P. Stephan, and F. Coge. High-throughput drug profiling with voltage- and calcium-sensitive fluorescent probes in human ipsc-derived cardiomyocytes. *American Journal of Physiology-Heart and Circulatory Physiology*, 311(1):H44–H53, May 2016.

[8] J. M. Beggs and D. Plenz. Neuronal avalanches in neocortical circuits. *The Journal of neuroscience : the official journal of the Society for Neuroscience*, 23(35):11167–77, dec 2003.

[9] J. M. Beggs and N. Timme. Being critical of criticality in the brain. *Frontiers in physiology*, 3(June):163, jan 2012.

[10] Z. Bing, L. Dong-sheng, X. Lue-lue, Y. Wei, W. Xin-zhan, Z. Xin, and L. Hongjian. Related content tunable surface-plasmon-resonance wavelength of silver island films tunable surface-plasmon-resonance wavelength of silver island films. *Chinese Physical Society*, 19(11):117310–1, 2010.

[11] O. Caspi, I. Itzhaki, I. Kehat, A. Gepstein, G. Arbel, I. Huber, J. Satin, and L. Gepstein. In vitro electrophysiological drug testing using human embryonic stem cell derived cardiomyocytes. *Stem Cells and Development*, 18(1):161–172, May 2008.

[12] O. Caspi, A. Lesman, Y. Basevitch, A. Gepstein, G. Arbel, I. Huber, M. Habib, L. Gepstein, and S. Levenberg. Tissue engineering of vascularized cardiac muscle from human embryonic stem cells. *Circulation Research*, 100(2):263–272, 2007.

[13] D. R. Chialvo. Emergent complex neural dynamics. *Nature Physics*, 6(10):744–750, oct 2010.

[14] R. Claire, T. D. D., and G. S. C. Concise review: Maturation phases of human pluripotent stem cell-derived cardiomyocytes. *STEM CELLS*, 31(5):829–837, Jan 2013.

[15] M. Clements and N. Thomas. High-throughput multi-parameter profiling of electrophysiological drug effects in human embryonic stem cell derived cardiomyocytes using multi-electrode arrays. *Toxicological Sciences*, 140(2):445–461, 2014.

[16] L. N. de Castro. Fundamentals of natural computing: an overview. *Physics of Life Reviews*, 4(1):1–36, 2007.

[17] E. C. Demis, R. Aguilera, K. Scharnhorst, M. Aono, A. Z. Stieg, and J. K. Gimzewski. Nanoarchitectonic atomic switch networks for unconventional computing. *Japanese Journal of Applied Physics*, 55(11):1102B2, 2016.

[18] E. C. Demis, R. Aguilera, H. O. Sillin, K. Scharnhorst, E. J. Sandouk, M. Aono, A. Z. Stieg, and J. K. Gimzewski. Atomic switch networks—nanoarchitectonic design of a complex system for natural computing. *Nanotechnology*, 26:1–11, 2015.

[19] M. X. Doss, J. M. Di Diego, R. J. Goodrow, Y. Wu, J. M. Cordeiro, V. V. Nesterenko, H. Barajas-Martínez, D. Hu, J. Urrutia, M. Desai, J. A. Treat, A. Sachinidis, and C. Antzelevitch. Maximum diastolic potential of human induced pluripotent stem cell-derived cardiomyocytes depends critically on ikr. *PLOS ONE*, 7(7):1–17, 07 2012.

[20] T. Egashira, S. Yuasa, T. Suzuki, Y. Aizawa, H. Yamakawa, T. Matsuhashi, Y. Ohno, S. Tohyama, S. Okata, T. Seki, Y. Kuroda, K. Yae, H. Hashimoto, T. Tanaka, F. Hattori, T. Sato, S. Miyoshi, S. Takatsuki, M. Murata, J. Kurokawa, T. Furukawa, N. Makita, T. Aiba, W. Shimizu, M. Horie, K. Kamiya, I. Kodama, S. Ogawa, and K. Fukuda. Disease characterization using lqts-specific induced pluripotent stem cells. *Cardiovascular Research*, 95(4):419–429, Sep 2012.

[21] A. J. Engler, C. Carag-Krieger, C. P. Johnson, M. Raab, H.-Y. Tang, D. W. Speicher, J. W. Sanger, J. M. Sanger, and D. E. Discher. Embryonic cardiomyocytes beat best on a matrix with heart-like elasticity: scar-like rigidity inhibits beating. *Journal of Cell Science*, 121(22):3794, Nov 2008.

[22] A. W. Feinberg, C. M. Ripplinger, P. van der Meer, S. P. Sheehy, I. Domian, K. R. Chien, and K. K. Parker. Functional differences in engineered myocardium from embryonic stem cell-derived versus neonatal cardiomyocytes. *Stem Cell Reports*, 1(5):387–396, Nov 2013.

[23] G. Forte, S. Pagliari, M. Ebara, K. Uto, J. K. V. Tam, S. Romanazzo, C. Escobedo-Lucea, E. Romano, P. Di Nardo, E. Traversa, and T. Aoyagi. Substrate stiffness modulates gene expression and phenotype in neonatal

cardiomyocytes in vitro. *Tissue Engineering Part A*, 18(17-18):1837–1848, Apr 2012.

[24] N. Friedman, S. Ito, B. a. W. Brinkman, M. Shimono, R. E. L. DeVille, K. a. Dahmen, J. M. Beggs, and T. C. Butler. Universal Critical Dynamics in High Resolution Neuronal Avalanche Data. *Physical Review Letters*, 108(20):208102, may 2012.

[25] A. Goudarzi, M. R. Lakin, D. Stefanovic, and C. Teuscher. A Model for Variation- and Fault-Tolerant Digital Logic using Self-Assembled Nanowire Architectures. pages 116–121, jun 2014.

[26] T. B. Greenslade. All about Lissajous figures. *The Physics Teacher*, 31(6):364, 1993.

[27] L. Guo, R. M. C. Abrams, J. E. Babiarz, J. D. Cohen, S. Kameoka, M. J. Sanders, E. Chiao, and K. L. Kolaja. Estimating the risk of drug-induced proarrhythmia using human induced pluripotent stem cell-derived cardiomyocytes. *Toxicological Sciences*, 123(1):281–289, Sep 2011.

[28] S. E. Harding, N. N. Ali, M. Brito-Martins, and J. Gorelik. The human embryonic stem cell-derived cardiomyocyte as a pharmacological model. *Pharmacology & Therapeutics*, 113(2):341–353, 2007.

[29] T. Hasegawa, T. Ohno, K. Terabe, T. Tsuruoka, T. Nakayama, J. K. Gimzewski, and M. Aono. Learning abilities achieved by a single solid-state atomic switch. *Advanced materials*, 22(16):1831–4, apr 2010.

[30] T. Hasegawa, T. Ohno, K. Terabe, T. Tsuruoka, T. Nakayama, J. K. Gimzewski,

and M. Aono. Learning abilities achieved by a single solid-state atomic switch. *Advanced materials (Deerfield Beach, Fla.)*, 22(16):1831–4, apr 2010.

[31] L. B. Hazeltine, C. S. Simmons, M. R. Salick, X. Lian, M. G. Badur, W. Han, S. M. Delgado, T. Wakatsuki, W. C. Crone, B. L. Pruitt, and S. P. Palecek. Effects of Substrate Mechanics on Contractility of Cardiomyocytes Generated from Human Pluripotent Stem Cells. *International Journal of Cell Biology*, 2012:13, 2012.

[32] J. Hescheler, M. Halbach, U. Egert, Z. J. Lu, H. Bohlen, B. K. Fleischmann, and M. Reppel. Determination of electrical properties of es cell-derived cardiomyocytes using meas. *Journal of Electrocardiology*, 37:110–116, 2004.

[33] H. M. Himmel. Drug-induced functional cardiotoxicity screening in stem cell-derived human and mouse cardiomyocytes: Effects of reference compounds. *Journal of Pharmacological and Toxicological Methods*, 68(1):97 – 111, 2013. 10th Annual Focused Issue on Methods in Safety Pharmacology.

[34] J. H. Holland. Studying complex adaptive systems. *Journal of Systems Science and Complexity*, 19(1):1–8, Mar 2006.

[35] D. Hsu, W. Chen, M. Hsu, and J. M. Beggs. An open hypothesis: is epilepsy learned, and can it be unlearned? *Epilepsy Behavior*, 13(3):511–522, 2009.

[36] G. Indiveri, B. Linares-Barranco, R. Legenstein, G. Deligeorgis, and T. Prodromakis. Integration of nanoscale memristor synapses in neuromorphic computing architectures. *Nanotechnology*, 24(38):384010, 2013.

[37] A. Jalalvand, F. Triefenbach, K. Demuynck, and J.-P. Martens. Robust

continuous digit recognition using reservoir computing. *Computer Speech & Language*, 30(1):135–158, 2015.

[38] D. S. Jens Bürger, Alireza Goudarzi and C. Teuscher. Computational capacity and energy consumption of complex resistive switch networks. *CoRR*, abs/1507.03716, 2015.

[39] L. Jing, F. J. Dong, S. C. Wah, and L. R. A. Functional sarcoplasmic reticulum for calcium handling of human embryonic stem cell-derived cardiomyocytes: Insights for driven maturation. *STEM CELLS*, 25(12):3038–3044, Jan 2009.

[40] S. Jonathan, I. Ilanit, R. Sophia, S. E. A., I. Leighton, A. Gil, B. Rafael, B. C. William, S. Jackie, and G. Lior. Calcium handling in human embryonic stem cell-derived cardiomyocytes. *STEM CELLS*, 26(8):1961–1972, Jan 2009.

[41] S. J. Kattman, A. D. Witty, M. Gagliardi, N. C. Dubois, M. Niapour, A. Hotta, J. Ellis, and G. Keller. Stage-specific optimization of activin/nodal and bmp signaling promotes cardiac differentiation of mouse and human pluripotent stem cell lines. *Cell Stem Cell*, 8(2):228–240, Feb 2011.

[42] D. Katya, S. Mark, Z.-L. Naama, G.-N. Sharon, A. Michal, D. Asaf, I.-E. Joseph, and B. Ofer. Functional properties of human embryonic stem cell–derived cardiomyocytes: Intracellular ca2+ handling and the role of sarcoplasmic reticulum in the contraction. *STEM CELLS*, 24(2):236–245, 2005.

[43] C. T. Kello, J. Rodny, A. S. Warlaumont, and D. C. Noelle. Plasticity, learning, and complexity in spiking networks. *Critical reviews in biomedical engineering*, 40(6):501–18, 2012.

[44] C. Kim, M. Majdi, P. Xia, K. A. Wei, M. Talantova, S. Spiering, B. Nelson, M. Mercola, and H.-s. V. Chen. Non-cardiomyocytes influence the electrophysiological maturation of human embryonic stem cell-derived cardiomyocytes during differentiation. *Stem Cells Dev*, 19(6):783–795, Jun 2010.

[45] N. Kriegeskorte, W. K. Simmons, P. S. F. Bellgowan, and C. I. Baker. Circular analysis in systems neuroscience: the dangers of double dipping. *Nature Neuroscience*, 12(5):535–540, may 2009.

[46] V. J. Kujala, Z. C. Jimenez, J. Väisänen, J. M. A. Tanskanen, E. Kerkelä, J. Hyttinen, and K. Aalto-Setälä. Averaging in vitro cardiac field potential recordings obtained with microelectrode arrays. *Computer Methods and Programs in Biomedicine*, 104(2):199–205, 2011.

[47] M. A. Laflamme, K. Y. Chen, A. V. Naumova, V. Muskheli, J. A. Fugate, S. K. Dupras, H. Reinecke, C. Xu, M. Hassanipour, S. Police, C. O'Sullivan, L. Collins, Y. Chen, E. Minami, E. A. Gill, S. Ueno, C. Yuan, J. Gold, and C. E. Murry. Cardiomyocytes derived from human embryonic stem cells in pro-survival factors enhance function of infarcted rat hearts. *Nature Biotechnology*, 25:1015 EP –, Aug 2007.

[48] C. G. Langton. Computation at the Edge of Chaos: Phase Transitions and Emergent Computation. *Physica D: Nonlinear Phenomena*, 42:12–37, 1990.

[49] J. S. Lansing. Complex Adaptive Systems. *Annual Review of Anthropology*, 32(1):183–204, 2003.

[50] S. Laura, B. Esther, S. Francesca, M. Alessandro, C. Elisabetta, and J. M. E. Developmental changes in cardiomyocytes differentiated from human embryonic

stem cells: A molecular and electrophysiological approach. *STEM CELLS*, 25(5):1136–1144, Jan 2007.

[51] J. W. Lawson and D. H. Wolpert. Adaptive Programming of Unconventional Nano-Architectures. *Journal of Computational and Theoretical Nanoscience*, 3(2):272–279, sep 2006.

[52] R. Legenstein and W. Maass. What makes a dynamical system computationally powerful? In *New Directions in Statistical Signal Processing: From Systems to Brains*, chapter What makes, pages 1–31. TBS, 2005.

[53] S. A. Levin. COMPLEX ADAPTIVE SYSTEMS : AND THE UNKNOWABLE. *Bulletin (New Series) of the American Mathematical Society*, 40(1):3–19, 2002.

[54] D. K. Lieu, J.-D. Fu, N. Chiamvimonvat, K. W. Chan Tung, G. P. McNerney, T. Huser, G. Keller, C.-W. Kong, and R. A. Li. Mechanism-based facilitated maturation of human pluripotent stem cell-derived cardiomyocytes. *Circ Arrhythm Electrophysiol*, 6(1):191–201, Feb 2013.

[55] T.-Y. Lu, B. Lin, J. Kim, M. Sullivan, K. Tobita, G. Salama, and L. Yang. Repopulation of decellularized mouse heart with human induced pluripotent stem cell-derived cardiovascular progenitor cells. *Nature Communications*, 4:2307 EP –, Aug 2013. Article.

[56] S. D. Lundy, W.-Z. Zhu, M. Regnier, and M. A. Laflamme. Structural and functional maturation of cardiomyocytes derived from human pluripotent stem cells. *Stem Cells and Development*, 22(14):1991–2002, Mar 2013.

[57] J. Ma, L. Guo, S. J. Fiene, B. D. Anson, J. A. Thomson, T. J. Kamp, K. L. Kolaja, B. J. Swanson, and C. T. January. High purity human-induced

pluripotent stem cell-derived cardiomyocytes: electrophysiological properties of action potentials and ionic currents. *Am J Physiol Heart Circ Physiol*, 301(5):H2006–H2017, Nov 2011.

[58] T. C. McDevitt, M. A. Laflamme, and C. E. Murry. Proliferation of cardiomyocytes derived from human embryonic stem cells is mediated via the igf/pi 3-kinase/akt signaling pathway. *J Mol Cell Cardiol*, 39(6):865–873, Dec 2005.

[59] C. Mead. Neuromorphic electronic systems. *Proceedings of the IEEE*, 78(10):1629–1636, Oct 1990.

[60] I. Minami, K. Yamada, T. Otsuji, T. Yamamoto, Y. Shen, S. Otsuka, S. Kadota, N. Morone, M. Barve, Y. Asai, T. Tenkova-Heuser, J. Heuser, M. Uesugi, K. Aiba, and N. Nakatsuji. A small molecule that promotes cardiac differentiation of human pluripotent stem cells under defined, cytokine- and xeno-free conditions. *Cell Reports*, 2(5):1448–1460, Nov 2012.

[61] C. Mummery, D. Ward, C. E. van den Brink, S. D. Bird, P. A. Doevendans, T. Opthof, A. B. de la Riviere, L. Tertoolen, M. van der Heyden, and M. Pera. Cardiomyocyte differentiation of mouse and human embryonic stem cells. *J Anat*, 200(3):233–242, Mar 2002.

[62] Y. Nakashima, D. A. Yanez, M. Touma, H. Nakano, A. Jaroszewicz, M. C. Jordan, M. Pellegrini, K. P. Roos, and A. Nakano. Nkx2-5 suppresses the proliferation of atrial myocytes and conduction system. *Circulation Research*, 114(7):1103–1113, 2014.

[63] E. G. Navarrete, P. Liang, F. Lan, V. Sanchez-Freire, C. Simmons, T. Gong, A. Sharma, P. W. Burridge, B. Patlolla, A. S. Lee, H. Wu, R. E. Beygui,

S. M. Wu, R. C. Robbins, D. M. Bers, and J. C. Wu. Screening adverse drug-induced arrhythmia events using human induced pluripotent stem cell-derived cardiomyocytes and low-impedance microelectrode arrays. *Circulation*, 128(11 0 1):10.1161/CIRCULATIONAHA.112.000570, Sep 2013.

[64] A. Nayak, T. Ohno, T. Tsuruoka, K. Terabe, T. Hasegawa, J. K. Gimzewski, and M. Aono. Controlling the Synaptic Plasticity of a Cu2S Gap-Type Atomic Switch. *Advanced Functional Materials*, 22(17):3606–3613, sep 2012.

[65] S. S. Nunes, J. W. Miklas, J. Liu, R. Aschar-Sobbi, Y. Xiao, B. Zhang, J. Jiang, S. Masse, M. Gagliardi, A. Hsieh, N. Thavandiran, M. A. Laflamme, K. Nanthakumar, G. Gross, P. H. Backx, G. Keller, and M. Radisic. Biowire: a new platform for maturation of human pluripotent stem cell derived cardiomyocytes. *Nat Methods*, 10(8):781–787, Aug 2013.

[66] T. Ohno, T. Hasegawa, A. Nayak, T. Tsuruoka, J. K. Gimzewski, and M. Aono. Sensory and short-term memory formations observed in a Ag2S gap-type atomic switch. *Applied Physics Letters*, 99(20):203108–1, 2011.

[67] T. G. Otsuji, I. Minami, Y. Kurose, K. Yamauchi, M. Tada, and N. Nakatsuji. Progressive maturation in contracting cardiomyocytes derived from human embryonic stem cells: Qualitative effects on electrophysiological responses to drugs. *Stem Cell Research*, 4(3):201–213, 2010.

[68] B. Piyush, T. Xin, S. T. A., and B. Rashid. Stiffness of the substrate influences the phenotype of embryonic chicken cardiac myocytes. *Journal of Biomedical Materials Research Part A*, 95A(4):1261–1269, Oct 2010.

[69] S.-S. Poil, R. Hardstone, H. D. Mansvelder, and K. Linkenkaer-Hansen. Critical-state dynamics of avalanches and oscillations jointly emerge from balanced excitation/inhibition in neuronal networks. *The Journal of neuroscience : the official journal of the Society for Neuroscience*, 32(29):9817–23, jul 2012.

[70] K. Scharnhorst, W. Woods, C. Teuscher, A. Stieg, and J. Gimzewski. Non-temporal logic performance of an atomic switch network. In *2017 IEEE/ACM International Symposium on Nanoscale Architectures (NANOARCH)*, pages 133–138. IEEE, 2017.

[71] K. S. Scharnhorst, J. P. Carbajal, R. C. Aguilera, E. J. Sandouk, M. Aono, A. Z. Stieg, and J. K. Gimzewski. Atomic switch networks as complex adaptive systems. *Japanese Journal of Applied Physics*, 57(3S2):03ED02, 2018.

[72] M. Shiojiri, Y. Hasegawa, and K. Konishi. Reaction of iodine vapor with silver films in the -agi phase region. *Journal of Applied Physics*, 44(7):2996–3000, 1973.

[73] H. Sillin, E. Sandouk, A. Avizienis, M. Aono, A. Z. Stieg, and J. K. Gimzewski. Benchtop Fabrication of Memristive Atomic Switch Networks. *Journal of Nanoscience and Nanotechnology*, 14(4):2792, 2013.

[74] H. O. Sillin, R. Aguilera, H.-H. Shieh, A. V. Avizienis, M. Aono, A. Z. Stieg, and J. K. Gimzewski. A theoretical and experimental study of neuromorphic atomic switch networks for reservoir computing. *Nanotechnology*, 24(38):384004, 2013.

[75] D. M. Smyth and M. Cutler.

[76] M. Snir, I. Kehat, A. Gepstein, R. Coleman, J. Itskovitz-Eldor, E. Livne, and L. Gepstein. Assessment of the ultrastructural and proliferative properties of human embryonic stem cell-derived cardiomyocytes. *American Journal of Physiology-Heart and Circulatory Physiology*, 285(6):H2355–H2363, 2003.

[77] A. Stieg and A. Avizienis. Self-organized atomic switch networks. *Japanese Journal of . . .*, 02:1–6, 2014.

[78] S. H. Strogatz. Exploring complex networks. *Nature*, 410(6825):268–276, 2001.

[79] D. B. Strukov, G. S. Snider, D. R. Stewart, and R. S. Williams. The missing memristor found. *Nature*, 453(7191):80–3, may 2008.

[80] H. Suemori, K. Yasuchika, K. Hasegawa, T. Fujioka, N. Tsuneyoshi, and N. Nakatsuji. Efficient establishment of human embryonic stem cell lines and long-term maintenance with stable karyotype by enzymatic bulk passage. *Biochemical and Biophysical Research Communications*, 345(3):926 – 932, 2006.

[81] K. Takahashi, K. Tanabe, M. Ohnuki, M. Narita, T. Ichisaka, K. Tomoda, and S. Yamanaka. Induction of pluripotent stem cells from adult human fibroblasts by defined factors. *Journal of Electrocardiology*, 131(5):861–872, 2007.

[82] S. Tappertzhofen, I. Valov, and R. Waser. Quantum conductance and switching kinetics of agi-based microcrossbar cells. *Nanotechnology*, 23(14):145703, 2012.

[83] K. Terabe, T. Hasegawa, T. Nakayama, and M. Aono. Quantized conductance atomic switch. *Nature*, 433(7021):47–50, 1 2005.

[84] K. Terabe, T. Hasegawa, T. Nakayama, and M. Aono. Quantized conductance atomic switch. *Nature*, 433(January):47–50, 2005.

[85] T. N. Theis and H. S. Philip Wong. The End of Moore's Law: A New Beginning for Information Technology. *Computing in Science and Engineering*, 19(2):41–50, 2017.

[86] J. A. Thomson, J. Itskovitz-Eldor, S. S. Shapiro, M. A. Waknitz, J. J. Swiergiel, V. S. Marshall, and J. M. Jones. Embryonic stem cell lines derived from human blastocysts. *Science*, 282(5391):1145–1147, 1998.

[87] E. Y. C. Tong. Lissajous figures. *The Physics Teacher*, 35(8):491, 1997.

[88] J. Tour, W. Van Zandt, C. Husband, S. Husband, L. Wilson, P. Franzon, and D. Nackashi. Nanocell logic gates for molecular computing. *IEEE Transactions On Nanotechnology*, 1(2):100–109, jun 2002.

[89] N. L. Tulloch, V. Muskheli, M. V. Razumova, F. S. Korte, M. Regnier, K. D. Hauch, L. Pabon, H. Reinecke, and C. E. Murry. Growth of engineered human myocardium with mechanical loading and vascular co-culture. *Circ Res*, 109(1):47–59, Jun 2011.

[90] N. H. L. van den Heuvel, T. A. B. van Veen, B. Lim, and M. K. B. Jonsson. Lessons from the heart: Mirroring electrophysiological characteristics during cardiac development to in vitro differentiation of stem cell derived cardiomyocytes. *Journal of Molecular and Cellular Cardiology*, 67:12–25, Feb 2014.

[91] A. Vanarse, A. Osseiran, and A. Rassau. A review of current neuromorphic ap-

proaches for vision, auditory, and olfactory sensors. *Frontiers in Neuroscience*, 10:115, 2016.

[92] D. Verstraeten, B. Schrauwen, M. D'Haene, and D. Stroobandt. An experimental unification of reservoir computing methods. *Neural Networks*, 20(3):391–403, 2007.

[93] E. Willems, S. Spiering, H. Davidovics, M. Lanier, Z. Xia, M. Dawson, J. Cashman, and M. Mercola. Small molecule inhibitors of the wnt pathway potently promote cardiomyocytes from human embryonic stem cell derived mesoderm. *Circ Res*, 109(4):360–364, Aug 2011.

[94] W. Woods, M. M. A. Taha, S. J. Dat Tran, J. Burger, and C. Teuscher. Memristor panic - A survey of different device models in crossbar architectures. *Proceedings of the 2015 IEEE/ACM International Symposium on Nanoscale Architectures, NANOARCH 2015*, pages 106–111, 2015.

[95] W. Woods and C. Teuscher. Fast and Accurate Sparse Coding of Visual Stimuli with a Simple , Ultra-Low-Energy Spiking Architecture. (1).

[96] X. Yang, L. Pabon, and C. E. Murry. Engineering adolescence: Maturation of human pluripotent stem cell-derived cardiomyocytes. *Circ Res*, 114(3):511–523, Jan 2014.

[97] D. D. Young, D. D. Young, M. Sharma, and M. Sharma. Letters To Nature. *Nature*, 433(January):47–50, 2005.

[98] J. Yu, M. A. Vodyanik, K. Smuga-Otto, J. Antosiewicz-Bourget, J. L. Frane, S. Tian, J. Nie, G. A. Jonsdottir, V. Ruotti, R. Stewart, I. I. Slukvin, and J. A.

Thomson. Induced pluripotent stem cell lines derived from human somatic cells. *Science*, 318(5858):1917–1920, 2007.

[99] D. Zhang, I. Shadrin, J. Lam, H.-Q. Xian, R. Snodgrass, and N. Bursac. Tissue-engineered cardiac patch for advanced functional maturation of human esc-derived cardiomyocytes. *Biomaterials*, 34(23):5813–5820, Jul 2013.